

IMPROVED RESIDUAL STRESS PREDICTION IN METAL CUTTING

IMPROVED RESIDUAL STRESS PREDICTION IN METAL CUTTING

By YOUSSEF ZIADA, M.A.SC., B.ENG.

A Thesis

Submitted to the School of Graduate Studies
in Partial Fulfillment of the Requirements
for the Degree of Doctor of Philosophy
in Mechanical Engineering

McMaster University

© Copyright by Youssef Ziada, October 2013

Doctor of Philosophy (2013) McMaster University
(Mechanical Engineering) Hamilton, Ontario

TITLE: Improved Residual Stress Prediction in Metal Cutting

AUTHOR: Youssef Ziada, M.A.Sc., B.Eng. (McMaster University)

SUPERVISOR: Dr. Eu-Gen Ng

NUMBER OF PAGES: xii, 109

Abstract

Any machining operation induces significant deformation and associated stress states within the component being machined. Once the component has been finished and is removed from the machining tool, a portion of these stresses remain within the finished component, and are termed residual stresses. These stresses have a significant effect upon the performance of the final component. However, despite their importance there is no accurate and cost effective method for measuring residual stresses. For this reason predicting these stresses without the need for measurement is highly desirable. The focus of this thesis is on advancing the development and implementation of finite element models aimed at predicting residual stresses induced by metal cutting operations.

There are three main focus areas within this research, the first of which is concerned with predicting residual stresses when small feed rates are used. It is shown that in the existing cutting models residual stress prediction accuracy suffers when feed rates are small. A sequential cut module is developed, which greatly increases the accuracy of the predicted residual stress depth profiles.

A second area of focus concerns the influence of friction models on predicted residual stresses. A detailed set of simulations is used to elucidate the effect of friction not only for sharp tools, but also for tools which have accrued wear. It is shown that whilst friction is not of critical importance for new tools, as tools continue to wear the choice of friction model becomes significantly more important.

The third area of focus is on phase transformations, induced by the cutting process. A decoupled phase transformation module is developed in order to predict the depth, if any, of a phase transformed layer beneath the newly machined surface. Furthermore, the effect of this layer on the residual stress depth profile was also studied.

All three focus areas present new and novel contributions to the field of metal cutting simulations, and serve to significantly increase the capabilities of predictive models for machining.

Acknowledgements

First and foremost, I would like to express my deepest gratitude to my supervisor, Dr. Eu-Gen Ng, for his continuing guidance, support and advice throughout the course of this research, as well as for introducing me to field of finite element simulations. His advice has been invaluable in directing my research as well as in helping me find solutions to the problems I encountered. I would also like to thank Dr. Peidong Wu and Dr. Mukesh Jain for serving on my committee and providing further guidance.

I have been fortunate to work with many wonderful fellow graduate students who have provided much assistance as well as sometimes much needed distractions during this work. A special thanks must be conveyed to Keyvan Hosseinkhani for his help building models, as well as Nima Zarif Yussefian for his assistance in measuring tool wear and Terry Wagg for his assistance in the machining lab. Further, none of this work would have been possible without the financial assistance of the NSERC Canadian Network for Research and Innovation in Machining Technology (CANRIMT).

I would also like to express my gratitude to my parents, without their support and guidance, as well as occasional prodding in the right direction this would not have been possible, and that is before speaking of their ongoing financial support of my academic aspirations. Last, but certainly not least, I would like to thank Lisa Whillans not only for her loving support, but also for her saintly patience in putting up with the perpetual student.

Contents

Chapter 1: Introduction.....	1
1.1 Motivation	1
1.2 Scope	3
1.3 Thesis Outline	4
Chapter 2: Literature Survey	6
2.1 Residual Stresses	6
2.1.1 Geometric Tolerance.....	7
2.1.2 Part Strength.....	7
2.2 Machining Induced Residual Stresses	8
2.2.1 Cutting Edge	9
2.2.2 Tool Wear	10
2.2.3 Uncut Chip Thickness.....	11
2.2.4 Cutting Speed.....	12
2.2.5 Rake Angle.....	13
2.2.6 Tool Coating	13
2.3 Measuring Residual Stresses	14
2.3.1 Diffraction-Based Methods.....	14
2.3.2 Micro Magnetic Methods.....	15
2.3.3 Raman Spectrograph.....	16
2.3.4 Acoustic Methods	16
2.3.5 Deflection Method	17
2.3.6 Hole Drilling	17
2.3.7 X-ray Measurement Operating Principle	18
2.4 Previous Work in FEA Modelling of Metal Cutting.....	21
2.4.1 Sequential Cut.....	24
2.4.2 White Layer Formation.....	25
2.5 Summary	28
Chapter 3: General FEA Modelling of Metal Cutting	29
3.1 Introduction	29
3.2 Time Integration.....	30

3.3	Lagrangian Formulation.....	32
3.4	Eulerian Formulation.....	35
3.5	ALE Formulation	36
3.6	Material Models	38
3.7	Interfacial Friction.....	41
3.8	Heat Generation.....	43
3.9	Constraints.....	44
3.10	Thermal Relaxation Module.....	46
Chapter 4: Experimental Procedure.....		48
4.1	Cutting Tests	48
4.2	Workpiece and Tool Materials.....	50
4.3	Tool Wear Measurement.....	51
4.4	Residual Stress Measurement.....	52
4.5	Experimental Test Matrix.....	53
Chapter 5: Residual Stress Prediction when using Small Uncut Chip Thicknesses.....		54
5.1	Model Details	54
5.1.1	Metal Cutting Simulation Module	54
5.1.2	Sequential Cut Module	56
5.2	Results and Discussion.....	59
Chapter 6: Effect of Friction Models on Residual Stress Prediction.....		71
6.1	Model Details	71
6.1.1	Friction at the Tool-Chip Interface	71
6.1.2	Modelling Parameters	77
6.1.3	Worn Tool Geometry	78
6.2	Predicted Forces and Residual Stresses	79
6.3	Summary	92
Chapter 7: Phase Transformations in Residual Stress Prediction.....		95
7.1	Model Details	95
7.1.1	Modelling Parameters	95
7.1.2	Worn Tool Geometry	96
7.2	Friction at the Tool-Chip Interface.....	97
7.3	Phase Transformation Module	97

7.4	Predicting White Layer Depth.....	102
7.5	Modelling of Residual Stresses	105
Chapter 8:	Conclusions.....	111
8.1	Summary of Results	111
8.1.1	Small Uncut Chip Thickness (Sequential Cut)	111
8.1.2	Frictional Effects.....	112
8.1.3	Phase Change	113
8.2	Future Work	114
References	116
Appendix 1	Annealed Residual Stress Depth Profile	128

List of Figures

Figure 2-1: 2-D Representation of the Cutting Process	9
Figure 2-2: Approximate Current Capabilities of Selected Techniques (The Destructive Techniques are Shaded Gray) (Adapted from [28, 38]).....	18
Figure 2-3: Diffraction of X-rays by a Crystal Lattice (adapted from [40]).....	19
Figure 3-1: A Lagrangian Mesh in Pure Shear	33
Figure 3-2: UL Segments.....	33
Figure 3-3: UL Simulation with Massive Element Size	34
Figure 3-4: Fully Eulerian Mesh in Pure Shear	36
Figure 3-5: Partitioning Scheme for ALE.....	37
Figure 3-6: Normal Pressure and Shear Stress along Rake Face (Adapted from [100]) ...	42
Figure 3-7: Boundary Conditions and ALE Constraints.....	46
Figure 4-1: Schematic of Rib Turning	48
Figure 4-2: Orthogonal Cutting Setup	49
Figure 5-1: Schematic of the Sequential Cut Module.....	56
Figure 5-2: Flowchart of Sequential Cut Procedure	58
Figure 5-3: Experimentally Measured Residual Stress Depth Profile at Fixed Undeformed Chip Thickness of 0.07 mm at 100 m/min and 200 m/min Cutting Speed.....	61
Figure 5-4: Effect of Cutting Speed on Temperature Distribution Beneath the Newly Machined Surface	61
Figure 5-5: Comparison Between Measured and Predicted Residual Stress Profile at 100 m/min Cutting Speed and 0.07 mm Undeformed Chip Thickness	62
Figure 5-6: Temperature Profile Beneath the Newly Machined Surface after Passing through the Cutting Edge at 100 m/min Cutting Speed and 0.07 mm Undeformed Chip Thickness.	63

Figure 5-7: Thermal and Mechanical Induced Stress Distributions Beneath the Newly Machined Surface for 100 m/min Cutting Speed and 0.07 mm Undeformed Chip Thickness.	64
Figure 5-8: Schematic of Stress and Energy Released in Pre-Hardened Layer.....	66
Figure 5-9: Temperature Distribution through the Chip at 100 m/min Cutting Speed and 0.70 mm Undeformed Chip Thickness	66
Figure 5-10: Effect of Process Parameters on Experimental and Predicted Cutting Forces.	67
Figure 5-11: Comparison Between Measured and Predicted Residual Stress Profile at 200 m/min Cutting Speed and 0.07 mm Undeformed Chip Thickness	68
Figure 5-12: Comparison Between Measured and Predicted Residual Stress Profile at 100 m/min Cutting Speed and 0.14 mm Undeformed Chip Thickness	68
Figure 5-13: Comparison Between Measured and Predicted Residual Stress Profile at 200 m/min Cutting Speed and 0.14 mm Undeformed Chip Thickness	69
Figure 6-1: Worn Cutting Edge Geometry	79
Figure 6-2: Comparison of Cutting Forces	80
Figure 6-3: Comparison of Thrust Force	81
Figure 6-4: Effect of Coefficient of Friction on Residual Stress Profiles.....	82
Figure 6-5: Thermal Contributions towards Total Residual Stress Profile.....	83
Figure 6-6: Effect of Shear Limit on Residual Stress Profiles.....	83
Figure 6-7: Shear Stress along the Tool-Chip Interface	84
Figure 6-8: Cutting Forces and Thrust Forces for High Tool Wear ($V_b= 175.5 \mu\text{m}$, $V_c=180 \mu\text{m}$).....	87
Figure 6-9: Residual Stress Profiles for Increasing Friction without a Shear Limit.....	89
Figure 6-10: Mechanical and Thermal Contributions towards Total Residual Stress Profile ($\mu=0.22$)	90
Figure 6-11: Effect of Shear Limit with Significant Tool Wear.....	91
Figure 7-1: Cutting Edge Geometry	97

Figure 7-2: Flow Chart of Phase Transformation Prediction Module	101
Figure 7-3: Cutting and Thrust Forces	102
Figure 7-4: Volume Fraction Martensite Predicted as a Function of Tool Wear.	103
Figure 7-5: Micrographs Cut with 267 μm Flank Wear on Left and at 332 μm Flank Wear on the Right.	104
Figure 7-6: Volume Fraction Martensite Predicted as a Function of Tool Wear, Average Whitelayer Thickness for $v_b = 332$ is Indicated as the Shaded Region.	105
Figure 7-7: Experimentally Measured Residual Stress Profiles	106
Figure 7-8: Experimental and Simulated Residual Stress Profiles for $v_b = 88 \mu\text{m}$, 267 μm and 332 μm Respectively from Left to Right.....	107
Figure 7-9: Effect of Phase Transformation Module	108
Figure 7-10: Component Contribution towards Total Residual Stress Profile, for $v_b = 88 \mu\text{m}$, 267 μm and 332 μm respectively from left to right.	109
Figure 7-11: Nature of White Layer Formed at Various Speeds and Workpiece Metallurgical States. (Adapted from [52])......	110
Figure A-1: Annealed AISI 1045 Sample Residual Stress Depth Profile	128

List of Tables

Table 3-I: Comparison of Strain and Strain Rates for Some Machining Processes ([84])	30
Table 3-II: Variables and Parameters of the <i>Johnson-Cook</i> Model.....	39
Table 4-I: Workpiece and Tool Materials.....	51
Table 5-I: AISI 1045 Johnson Cook Material Constants [101].	55
Table 5-II: Tool Substrate and Coating Materials Mechanical and Physical Properties. ...	55
Table 5-III: Simulation Test Matrix.....	59
Table 6-I: Test Matrix for Various Friction Conditions	77
Table 6-II: Effect of Friction Model Test Matrix (AISI 1045 Cut Using an Uncoated WC Tool).....	77
Table 6-III: Remaining Thermo-Mechanical Properties [105]	78
Table 7-I: Plastic Properties and the Workpiece [115]	96
Table 7-II: Remaining Thermo-Mechanical Properties	96
Table 7-III: Effect of Phase Transformations Test Matrix (AISI 4140 Cut Using an Uncoated WC Tool).....	102

Chapter 1: Introduction

This chapter provides an introduction to the research performed, including the motivation, scope of the work performed and the outline of the thesis.

1.1 Motivation

In any manufacturing process where a material is heavily deformed, residual stresses are induced within the manufactured part. In machining, this usually results in a thin layer near the surface of the manufactured component subject to both tensile and compressive stresses. The development of these stresses is defined by complex interactions among a large number of different parameters such as material properties, machining kinematics, thermal interactions between the tool and the workpiece and pre-existing stresses in the workpiece.

The retained stress state near the surface has a significant effect on final part performance. Changes in this residual stress profile have been reported to affect fatigue life of a component by as much as an order of magnitude. As such, detailed knowledge of the residual stresses induced during the manufacture of a component is highly desirable. However, current measurement techniques for the experimental measurement of these profiles are not only sensitive to measurement uncertainties, but the most accurate techniques also tend to be expensive, with each measured profile costing in the order of thousands of dollars, even at academic rates.

Considering the prohibitive cost of experimental measurements, parametric studies into the effects of machining parameters on the formation of residual stresses lag significantly behind studies for any other aspect of the machining process. Consequently, predicting the formation of residual stresses during metal cutting is of academic interest. However, the inherent complexity of the cutting process itself makes analytical studies of the process very challenging, typically requiring significant simplification of the process. Despite the obvious desirability of accurate predictive models, the challenges associated have kept these models in their infancy for many years.

In order to incorporate as much as possible of the complexity of the actual cutting process, finite element analysis (FEA) is often utilized as the means of numerically simulating the cutting process. Although there are significant advantages of these simulations, there is still much progress to be made in the use of FEA models for the prediction of residual stresses. Significant gaps still exist within the literature. As it stands, there is a need for improvement in accurately predicting residual stresses when using small uncut chip thickness. The interaction of tool-workpiece friction with the prediction of residual stresses, especially using worn tools, is still not well understood, and the effect of phase transformation on predicted residual stress profiles is still underdeveloped.

These above aspects all represent an important shortcoming of current cutting models, even confined to orthogonal (2-D) cutting. As such the goal of this work can be separated into three distinct parts. Each will advance the ability of finite element

techniques for the simulation of metal cutting towards the eventual goal of practical residual stress prediction for industrially relevant cutting.

1.2 Scope

The work presented in this thesis involves FEA modeling of the metal cutting process. In particular arbitrary *Lagrangian-Eulerian* (ALE) models are used to capture the cutting process with a subsequent relaxation module, which predicts the final residual stress profile of the finished surface. At present, the work remains confined to 2-D orthogonal cutting.

Within this framework, the scope of this work is three fold, the first being concerned with sequential cut modelling, the second on the influence of friction and tool wear and the third being the incorporation of phase transformations into the relaxation module. Each of these three contributions is described briefly below.

For cases where the uncut chip thickness is small, it is shown that the accuracy of the residual stress prediction using traditional methods is poor. A sequential cut module is developed to circumvent this problem, and to allow for accurate predictions at small uncut chip thickness values.

Since the literature is divided on the sensitivity of the final predicted stress profile to changes in friction model, the influence of friction on residual stress prediction is investigated.. In order to expand on this analysis, the effect of tool wear is integrated into the ALE cutting model, a capability previously missing in the literature.

Finally, the relaxation module is expanded to predict thermally induced phase changes in steels. The volumetric changes induced are coupled to the stress field in order to allow for the prediction of residual stress profiles with severely worn tool under high cutting speeds.

The modeling results from all three contributions are validated against residual stress profiles, measured using x-ray diffraction after orthogonal cutting experiments. The advances in residual stress prediction described above represent a notable contribution to the state-of-the-art, as well as a significant improvement in the capabilities of the ALE cutting model.

1.3 Thesis Outline

The work in this thesis is presented in eight chapters. The first of these, the current one, concerns the general motivation of the work as well as the general structure and scope of the thesis. The following chapter presents a summary of the current state-of-the-art in residual stress prediction. To this effect, the chapter begins with a general description of residual stresses and their relevance to metal cutting. Experimental techniques for the measurement of residual stresses are discussed next, followed by a discussion of previous work in the modelling of machining induced residual stresses.

In the third chapter, a general ALE cutting model, used throughout the present work, is described in great detail. Then, chapter four focusses on the description of the experimental work used in the validation of the modelling work presented in the subsequent chapters. Details of workpiece, tools as well as experimental procedures are

then discussed. The next three chapters (five, six and seven) present the results of the current work. Each chapter starts by discussing the variation from the general ALE cutting model, followed by a presentation and discussion of the results.

Chapter five comprises the changes to the relaxation module to implement sequential cuts, and the results of this module are then presented and discussed.

Chapter six begins with a detailed discussion of different friction models, and then presents the results of a study of the effect of these models on the predicted residual stress profiles for both lightly and heavily worn tools.

Chapter seven introduces a further modification to the relaxation module that allows for the prediction of phase transformations. The results are subsequently discussed in terms of predicted phase transformed layer first, and then in terms of modification to the predicted residual stress profile.

The final chapter summarizes the main conclusions drawn from this work as well as making recommendations for the future direction of this work.

Chapter 2: Literature Survey

This chapter is presented in four parts. First, the causes and effects of residual stresses are addressed. Then, residual stresses arising specifically from machining are discussed, followed by a discussion of their measurement. The last part deals with the prediction of residual stress generated by metal cutting.

2.1 Residual Stresses

Residual Stresses, or internal stresses, are the stresses which remain within an elastic body without having an external load applied to it. They exist in a free elastic body with no forces applied upon its boundaries[1-2]. These stresses are one of the most important parameters that characterise the surface and subsurface properties and subsequent performance of any mechanical component. They affect fatigue life, resistance to crack growth, static strength, corrosion resistance and magnetic properties, and depending on the particular stress distribution in any component, these properties can enhance or impair the part performance [1].

Residual stresses are induced by one of two main processes: nonuniform plastic deformation and phase transformations. Further nonuniform deformations can be induced either mechanically or through thermal processes. Thus any residual stress profile can be decomposed into the effects of three separate components, those arising from mechanical, those from thermal and volumetric changes due to phase transformation. In metal cutting all these processes are interrelated and lead to complex residual stress profiles.

Residual stresses have an effect on many aspects of part performance, some of the main effects are given below.

2.1.1 Geometric Tolerance

If the magnitude of residual stresses within a component is very large, as compared to part size, the net shape of a component can change. This results in geometric deformations which violate part tolerances. These changes can be seen in micro scale components such as micro-fins [3] or large components such as landing gears, and can be induced by a wide variety of processes. More particular to machining, however, is the comparatively shallow depth of the induced residual stress profiles that makes this a more likely problem for small components, or components with extremely tight tolerances. In general machining, tensile stresses induced by the cutting process cause a concave or ‘dish shaped’ curve to the machined surface, of the same order of magnitude as the depth of the removed cross-section of material [1].

2.1.2 Part Strength

Residual stresses in a component act as a pre-existing stress, which, depending on the type of subsequent loading, can be either advantageous or detrimental to the load carrying capacity of the component. If the component is loaded in tension, tensile residual stresses will result in the weakening of the component whereas compressive residual stresses will increase the load carrying capacity. This, however, is only significant if the residual stresses are of the same order of magnitude as the applied stresses.

Even if the residual stresses are not of the same magnitude as the applied loads they can have a significant effect on component's fatigue strength. Near surface residual stresses have a particularly significant effect under cyclic loading. This is because fatigue fractures usually start at the surface of a component [4]. Residual stresses thus serve to control the fatigue life of a component, where compressive residual stresses near the surface tend to negate crack initiation. On the other hand tensile residual stresses accelerate both the initiation and growth of fatigue cracks [5].

Both cutting and grinding processes induce surface residual stresses, which determine the fatigue life of components. This can be accounted for by an adjustment to the threshold stress intensity factor for crack initiation [6, 7]. Poor machining conditions can induce significant surface tensile stresses, and result in an up to 80% decrease in endurance limit for titanium components [8].

Since compressive residual stresses can be beneficial to part performance, some operations are used to induce such stresses as well as close any pre-existing surface micro cracks from previous processing; for example, processes such as shot peening and ball burnishing [5].

2.2 Machining Induced Residual Stresses

Most machining operations, milling, turning, shaping and broaching can be treated in a similar manner. In other words, if a cross section of the workpiece and cutting tool is considered for any of these operations, the same chip formation process is found as shown in Figure 2-1.

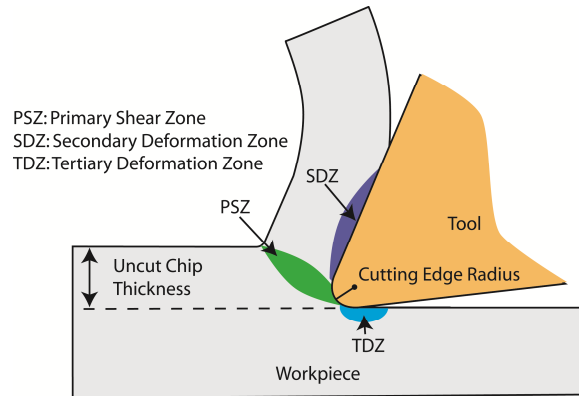


Figure 2-1: 2-D Representation of the Cutting Process

The effect of most of the labeled features in Figure 2-1 upon the formation of residual stresses in the cutting process have been studied. A summary of some of the known behaviours is outlined in the following subsections.

2.2.1 Cutting Edge

The cutting edge radius, or edge treatment has possibly the strongest influence of all the cutting parameters upon the magnitude and type of the residual stresses induced during cutting [9]. It has been found that when sharp tools are used at high speeds, solid state phase transformations are common in steels, leading to a thin martensitic layer along the newly formed surface. However at lower speeds no phase transformations were evident. This means that at high speeds changes in the lattice structure of steel contribute to the residual stresses present in the workpiece, but at low speeds only mechanical deformations are responsible for these stresses, and this is because at lower speeds temperatures can be hundreds of degrees lower than at high speeds. This behaviour often

interacts with the effect of tool coatings as these two factors are often studied together [10], the effect of these coatings is discussed in greater detail in Section 2.2.6.

In the case of honed tools, phase transformations were found to occur even at lower cutting speeds [11], as the increased plastic deformation leads to increased cutting temperatures. This makes the prediction of residual stresses for honed cutting tool geometries more complex than sharp tools, particularly at low speeds such as used in broaching.

Also, in general, the magnitude of the residual stress profiles present after cutting were found to increase as cutting edge radii were increased. This was found to be the case for a variety of uncut chip thicknesses and cutting speeds [11]. Furthermore, increases in edge radii are associated with higher compressive surface residual stresses because mechanical loading is increased as the effective rake angle becomes smaller. This can be beneficial for fatigue life of components, and is associated with the increased frictional interaction between the tool and workpiece [12]. Ee et al. improved the *Johnson-Cook* material in order to account for the severe hydrostatic pressure associated with large edge radii in cutting [13].

2.2.2 Tool Wear

There are many types of tool wear. The two most commonly known gradual wear types are crater wear and flank wear. Crater wear, which manifests in the secondary shear deformation zone, primarily affects the chip and thus has less influence on the development of residual stresses than with chip formation. Flank wear, which causes the

blunting of the tool flank, has strong influences upon the residual stresses in both magnitude and type. The ironing effect of the flank wear induces some compressive stresses on the process. However, by far the more significant effect is felt due to the increase in temperature at the tool tip, brought about by the increased frictional interaction at the rake flank [14, 15]. Increased temperature gradients are associated with increases in surface tensile residual stresses. Thus flank wear can lead to tensile residual stresses on the surface of components or in components which were machined later during a tools life cycle. This was observed for a wide variety of materials such as tool steels, titanium alloys and maraging steel [16-18]. Another effect of this increased tool tip temperature from tool wear is a decrease in material yield strength during machining. Thus compressive residual stresses are projected deeper into the subsurface of workpieces when using worn tooling [19].

In addition to the above, a phase transformation in steel workpieces can arise from the increased temperature associated with worn tools, during machining. Worn tools are commonly associated with the formation of a martensitic white layer in the workpiece surface. The volumetric changes induced by these surface phase changes lead to increased, predominantly tensile, residual stresses. All these thermal effects upon residual stress brought about by tool wear can in fact sometimes be the deciding factor upon the serviceable life of a tool [20].

2.2.3 Uncut Chip Thickness

In general, effect of uncut chip thickness is extremely material-dependant, and can give rise to either compressive or tensile surface and subsurface residual stresses. In

most cases the uncut chip thickness has a limited effect at the surface but increases the depth of penetration of the residual stresses [21]. Mostly these effects are compressive, but under specific cutting conditions, as described below, can become tensile.

In general these effects are explained by the increased heat dissipation brought about through increase in the chip size. As chip size increases, more of the generated heat is dissipated through the chip, reducing the thermal load on the workpiece and consequently reducing tensile residual stresses. Simultaneously, the increased loads associated with the higher chip load give rise to increased compressive loads at the tool tip [16]. However, in some cases large friction between the tool and workpiece can be attenuated by these increased loads. This causes larger temperature gradients in the tertiary shear deformation zone and can contribute to the tensile residual stresses in the workpiece [22]. Thus depending on the tool-workpiece pairing, either compressive or tensile residual stresses can be caused.

2.2.4 Cutting Speed

As in the case of uncut chip thickness, two separate effects compete with each other when increasing cutting speed. It increases the mechanical load, thus inducing compressive residual stress on the workpiece. However, increased speed also leads to higher temperature gradients, and consequently, increased tensile residual stresses. This can give rise to a critical cutting speed above which surface residual stresses change from compressive to tensile [23]. At higher speeds, however, thermal effects dominate; this usually results in increased tensile residual stresses at the surface of workpiece and a shallower penetration depth as the cutting speed is increased. This is because the high

temperatures at the cutting edge and decreased time allowed for thermal diffusion leads to steep thermal gradients at the part surface [22]. Results contradicting this have, however, also been established, particularly when cutting highly strain rate sensitive materials. This is explained as a function of higher heat dissipation through the chip when cutting strain rate sensitive materials at high cutting speeds [2, 9].

Changes in chip type can also occur at higher cutting speeds, which can lead to some inconsistent results with regards to inducing compressive or tensile stresses [17].

2.2.5 Rake Angle

In machining, rake angles in excess of $\pm 25^\circ$ are not common, and the effect of these changes in rake angle are mainly determined by classic cutting mechanics. As rake angle decreases cutting forces and shear plane angle decrease. The increased shear causes a consequent rise in cutting temperature. In general the behaviour reported is that at large positive rake angle, tensile surface residual stresses dominate due to decreased heat dissipation through the chip. Negative rake angles induce dominantly compressive stresses because loads are increased and heat is removed by the chip [21, 23, 24].

2.2.6 Tool Coating

In order to reduce workpiece adhesion on cutting tools, and consequently improve cutting tool performance, tools are often coated with lubricous layers. In general these coatings are used to decrease frictional forces, this is typically thought to result in decreased magnitude of the surface residual stresses, but increased depth of the residual stress profile [22, 25]. However, more recent studies suggest that in fact the measurement

techniques used were not suitable for surface measurement, and when X-ray diffraction is used, an opposite trend is observed. In other words, coated tools tend to result in higher residual stresses, both near the surface as well at a greater penetration depths [10, 26]. It is worth noting that this trend is not thought to be due to decreased friction, but rather due to the thermal barrier introduced by the coatings between the tool and workpiece [10, 25].

2.3 Measuring Residual Stresses

Measuring residual stresses is not a trivial matter, so considerable attention has been given by a large number of researchers to novel or improved measurement technologies [27]. By far the most popular type of measurement is based on diffraction methods.

2.3.1 Diffraction-Based Methods

X-ray diffraction is perhaps the most commonly used method of measurement of residual stresses. As with all diffraction based methods, the elastic strain of specific atomic lattice planes is measured; the principle exploited for this is discussed in Section 2.3.7. In general the penetration depth of X-rays in steels is limited to about 5 μm below the surface [28]. This means that X-ray diffraction technique is suitable for surface residual stresses only, unless sequential surface layers are removed. In practice this means incremental layers of material are etched from the workpiece and residual stress measurements are taken at each depth in order to yield a depth profile. Neutron diffraction, on the other hand, can be used as an alternative in order to achieve deeper penetration depths [29]. In fact experiments performed on reactor sources and spallation

sources can probe depths of up to 50mm in steels [30, 31] . Some modern synchrotron sources can even produce x-rays at sufficiently high energy level to penetrate into steel to nearly the same depths as neutrons [32]. However the difference in scattering angles of the two types of beams leads to a nearly cuboidal sampling region for neutron sources and an elongated diamond shaped prism for X-ray sources. This makes the measurement of stresses difficult using X-rays unless simplifying assumptions, such as plane stress, are made in the data analysis. In practice this means for deep penetrating stresses, neutrons are still more suitable [28]. The obvious advantage to either neutrons or high energy X-rays from a synchrotron is that since the process is non-destructive, fatigue tests or any other tests can be carried out on a sample that has already had its residual stresses appraised, allowing for monitoring of changes in these stresses throughout a component's service life [6].

2.3.2 Micro Magnetic Methods

A further non-destructive measurement technique that is receiving interest is magnetic methods. The operating principle behind these methods is that the electrical conductivity, as well as magnetic properties, of ferromagnetic materials vary with the internal strain state. Consequently changes in these properties can be used to calculate the internal strain state of a component. Traditionally however, the weakness of this method is that the sensitivity of these magnetic and electrical properties is poorly understood in regards to microstructural composition and changes, density and various other properties of the component. Modern systems can, however, determine biaxial stress levels provided there is enough information to calibrate for poor surface quality and geometric influences

[28]. In industrial situations, where substantial calibration is possible for similar components, magnetic methods have the advantage of being extremely cost effective, very fast, as well as being able to penetrate up to several millimeters in a completely non-destructive manner.

2.3.3 Raman Spectrograph

Raman spectrograph can be used to measure a variety of parameters, including stresses, in crystalline and amorphous materials. The operating principle behind using Raman spectrograph to measure residual stresses is that Raman peaks experience splitting and shifts in the presence of stresses that are linearly related to the stresses. Thus, mechanical stresses can be inferred by changes within the Raman peak [33]. In addition to its material limitations, this measurement technique is limited to surface measurement.

2.3.4 Acoustic Methods

There are numerous acoustic techniques used for measuring residual stresses. In scanning acoustic microscopy (SAM) a focused acoustic signal is scanned across a surface that causes propagation of the excited acoustic waves through the mechanical workpiece. The wave propagation depends on a variety of parameters such as elastic, electric and mechanical properties of the workpiece. According to local variations in these properties, information about the extent of the residual stresses can be obtained [34, 35]. A related technique is laser ultrasonic measurement, wherein an ultrasonic wave is generated using a pulsed laser. Based on the *Rayleigh* wave speed measured in the sample, information about the surface texture and residual stress state can be obtained [36]. This technique has been applied to measuring residual stresses in automotive

components [36], as well as for the assessment of material damage in nickel-based super alloys [37].

2.3.5 Deflection Method

All the techniques discussed so far are so called direct methods, in which a parameter that is affected by the residual stresses is measured. Indirect methods on the other hand depend on disturbing the equilibrium in a sample; and by measuring the resulting deformation. The most famous of these techniques, and the oldest, is the deflection method. In this technique layers of material are removed from the sample being measured. Removal of these layers results in a deflection of the part. These deflections are measured as a function of thickness. The amount of stress released by removing the layer is then related to the magnitude of the deformations [1, 38] . The main problem with this technique is a significant increase in complexity if the sample is not a simple plate or cylinder. Also this technique is extremely sensitive to temperature fluctuations necessitating excellent temperature controls [1].

2.3.6 Hole Drilling

Unlike the deflection method, hole drilling provides a relatively simple method for measuring a residual stress depth profile. Further, the geometry of the overall component is largely unimportant. The principle, however, is much the same as when the strains induced by removing a cylinder of material is measured using strain gauges [39]. From these measured strains, residual stresses are calculated using calibration constants derived for the particular strain gauge rosette used, as well as for the type of stresses expected [38]. Advantages of hole drilling include its ability to measure a wide range of materials,

and the sample only needs to be isotropic with known elastic parameters [38]. One of its main disadvantages is, however, a thin dead zone near the surface on the order of $10\mu\text{m}$.

The approximate capabilities of a few of these techniques, compared to each other can be seen summarized in Figure 2-2.

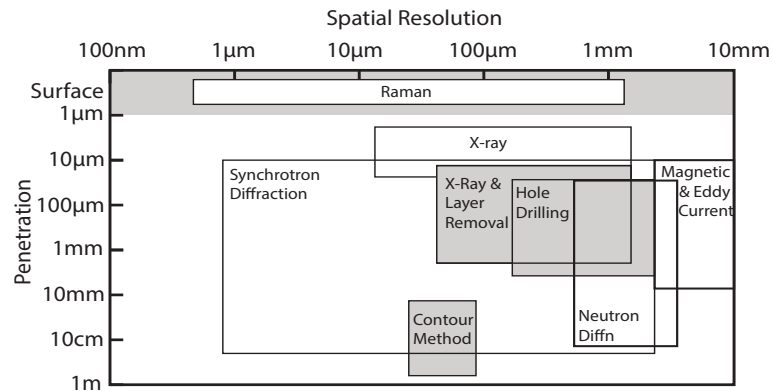


Figure 2-2: Approximate Current Capabilities of Selected Techniques (The Destructive Techniques are Shaded Gray) (Adapted from [28, 38])

2.3.7 X-ray Measurement Operating Principle

All diffraction-based methods operate by measuring the elastic strain of specific atomic lattice planes. The basic operating principle behind this is based on the diffraction pattern obtained from a crystal lattice. In order to explain this, consider a small lattice shown in Figure 2-3, where X-rays leave the source at XX' and reach the sensor at plane YY' .

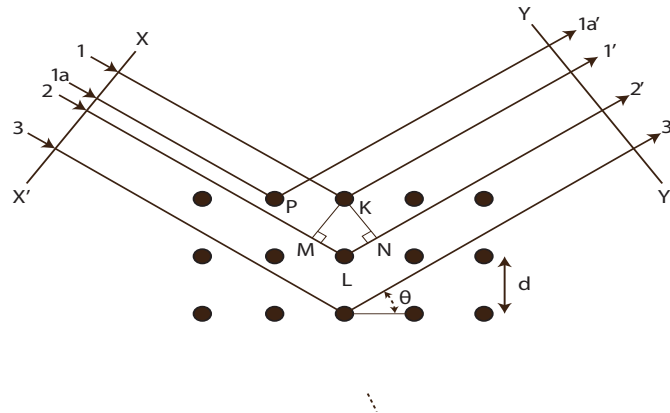


Figure 2-3: Diffraction of X-rays by a Crystal Lattice (adapted from [40])

If we consider the top layer of atoms only, the rays 1 and 1a strike atoms K and P respectively and scatter in all directions. Only in the direction 1' and 1a' do the scattered beams interfere constructively, they are in phase as the distance traveled from XX' to YY' is the same. Now if we consider the next layer of atoms as well, we find that rays 1 and 2 strike atoms K and L respectively. The difference in path lengths between 11' and 22' can be expressed as:

$$ML + LN = d\sin\theta + d\sin\theta \quad (2-1)$$

The maximum constructive interference of this pattern will occur when this increase in path length is equal to increments of the wave length of the X-ray (λ). That is to say:

$$n\lambda = 2d \sin \theta \quad (2-2)$$

This relationship is called *Bragg's law*, and it describes the relationship between a crystal lattice spacing (d) and its diffraction pattern. By altering the interplaner spacing, from straining the material, changes occur within the diffraction pattern. Through careful

measurement of these changes, strain within the material can be deduced and consequently the elastic stress.

From the unstressed and stressed lattice spacing for a material (d_0) the strain can be calculated, for an arbitrary sample angle (Ψ) from Equation (2-3):

$$\varepsilon_{\Psi} = \frac{d - d_0}{d_0} \quad (2-3)$$

These strains can then be related to stress through simple elastic theory. It has been shown [41, 42] that the stress in an arbitrary direction along the surface plane (σ_{ϕ}) is given by Equation (2-4):

$$\sigma_{\phi} = \frac{E}{(1 + \nu) \sin^2 \Psi} \left(\frac{d_{\Psi} - d_n}{d_n} \right) \quad (2-4)$$

Where d_n is the lattice spacing determined with the sample tilted such that $\Psi = 0$.

The most common method for determining the residual stress in the above, is the $\sin^2 \Psi$ method. In this method a number of lattice spacing measurements (d_{Ψ}) are made, these measurements are then plotted against $\sin^2 \Psi$, which, under ideal conditions, results in a straight line. If we assume zero stress at $d = d_n$, where d is the intercept on the y-axis when $\sin^2 \Psi = 0$ and m as the slope of the d vs $\sin^2 \Psi$ line as shown in Equation (2-5):

$$\sigma_{\phi} = \left(\frac{E}{1 + \nu} \right) m \quad (2-5)$$

This forms the basis for residual stress measurement using X-rays.

2.4 Previous Work in FEA Modelling of Metal Cutting

A substantial amount of work has been done in modelling of machining processes both analytically as well as numerically..In recent years with the rapid advances in computing power, sophisticated FEA models are becoming the norm in simulating the cutting process. However, analytical models are still used. Liang and Su [43] present a model for residual stress prediction which calculates the temperature and stress fields during cutting using slip-line theory. These fields are used for calculation of residual stresses induced by cutting. A comprehensive review of the current-state-of-the-art can be found in the recent CIRP keynote address by Arrazola et al. [44]. The main conclusions drawn were that significant progress has been made in simulating metal cutting but that an important gap still exists between the 2D models in the academic laboratory and 3D models for specific industrial operations. A further conclusion was that the lack of consistent and reliable data on material properties presents a significant difficulty that needs to be overcome. Currently, the majority of work is based around applying 2D finite element methods to the cutting problem, with a focus on a wide variety of sub-topics such as predicting cutting forces, temperatures, chip morphology, tool wear and white layer formation.

Metal cutting is a highly non-linear process with very strong strain and thermal gradients, despite this the most commonly implemented numerical solutions are implicit [13, 45-52], these are split between *Lagrangian* simulations [45-47] which necessitate a fracture criterion and continuously re-meshing models [48-52] which are most commonly performed in the commercially available FEA solver Deform-2D. Explicit

solutions for this problem are however also available [53-62]. Explicit *Lagrangian* simulations suffer the same disadvantages as the implicit ones, with slightly improved stability. To overcome these disadvantages, re-meshing schemes for the explicit solutions are of particular interest, this includes arbitrary *Lagrangian-Eularian* (ALE) models which allow for advantages of both the *Lagrangian* and *Eularian* methods [59-62]. The individual advantages of these methods are covered in detail in Chapter 3.

ALE has found significant application within the last couple of decades, thus aspects of cutting models implemented in other techniques have yet to be addressed. Using both *Lagrangian*, as well as updated *Lagrangian* methods, segmented and saw tooth chips have been simulated by predicting adiabatic slip within the chip using *Recht's* criterion These techniques however have yet to be implemented in an ALE model [49, 63].

A further area which has received some attention is the modeling of the effect of material inhomogeneity (for example, different phases within the material of the workpiece) upon chip formation. In *Largangian* work this was achieved through the inclusion of two different material types with individual material definitions for each material phase [57, 58, 64]. This is not feasible for simulations that employ continuous re-meshing unless custom material definitions are created which track the motion of different material phases [52].

Tool wear has also been of interest, with flank wear predictions in uncoated carbide tools [65, 66]. Also crater wear models [67] have been proposed based on FEA simulation

using a dedicated cutting simulation software AdvantEdge. Using updated *Lagrangian* methods, similar models were created in Deform-2D [68] using the wear model by Usui et al. [69].

The influence of friction has also been studied, resulting in conflicting analysis. Early work by Shi and Deng [24] set the tone for validating models using cutting and thrust forces, having looked into the effects of changing the friction condition at the tool chip interface. This work was expanded by Oezel, who concluded that significant influence was exerted by the friction model on the accuracy of predicted forces [70]. This has been contradicted by the conclusions of Filice et al. [71] who, upon analysing a variety of friction conditions, concluded that the influence was inconsequential to the predicted forces. The effect of friction on cutting forces and residual stresses has been analyzed by Anurag and Guo [72]. Their results show that increasing friction does not strongly affect the maximum compressive residual stress: rather its effects are limited to a surface tensile layer. Yang and Liu [53] suggested a new friction model in order to predict residual stresses using a *Lagrangian* cutting model, but did not present any experimental results for validation.

According to the keynote paper by Jawahir et al. [27] residual stresses, surface hardness and microstructural changes are the most commonly evaluated surface integrity parameters, as determined by a comprehensive benchmark evaluation of surface and subsurface integrity [27]. In general, significant attention has been given to predicting residual stresses using cutting models, since simulating residual stresses can obviate many of the limitations of experimental residual stress measurement [53]. ALE models to

predict the residual stresses in some stainless steels, as well as tool steels, have been developed [59, 60, 62, 73, 74]. Similar work shows using updated *Lagrangian* techniques for the machining of titanium [75], Salvatore et al. [54] presented a *Lagrangian* model for predicting residual stresses by calculating an equivalent rake angle to compensate for not including the cutting edge radius. Kortbarria et al. [76] used Deform-3D FEA software to simulate turning of a nickel-based superalloy. Their results matched well with hole drilling experiments. However, significant differences were observed between X-ray diffraction measurements and hole drilling, possibly due to the severe straining of the near surface layer of the alloy. Analytical predictions for machining induced residual stresses were developed by Lazoglu et al. [77] which have the advantage of being extremely fast to compute, however including more complex cutting tool geometries presents significant challenges.

2.4.1 Sequential Cut

In order to investigate the effect of a previous pass on the subsequent pass, a number of researchers have developed so called sequential cut modules. Liu and Guo [47] proposed such a model for the investigation of sequential cuts on residual stresses in AISI 304 steel. Aside from showing that residual stresses decrease after the second pass, they also concluded that the resulting residual stress profile is highly sensitive to the friction condition between the tool and workpiece. Using the same model, Guo and Liu [78] presented a similar study which concluded that by varying the depth of the second cut below a critical value, desirable compressive residual stresses can be induced. Their work suggests that appropriate finishing conditions can be selected based upon this sequential

cut effect, in order to encourage desirable final part quality. It has to be noted however that this work did not include any experimental evidence to validate their models. Similarly Ee et al. [13] presented a sequential cut module when cutting AISI 1045 steel. This model was based on a continuously re-meshing cutting model, but provided no relaxation time between consecutive passes, and as with the work of Liu and Guo [47, 78], no experimental work was used for validation of the model. Outeiro et al. [79], using DEFORM 2D FEA software, presented a cutting model for a AISI 316L steel, that included the effect of sequential cut and presented experimental validation of their simulated residual stress results, However, their results were opposite to those found by both Liu and Guo [47, 78], using AISI 304 stainless steel, and by Ee et al. [13], for 1045 steel. Surprisingly the model results of Outeiro et al [79] agreed less well with experimental results when the sequential cut module was used. This suggests that some of the simplifications within the model were unfounded, such as ignoring tool wear.

It is worth noting that only a few studies predicting residual stresses with an ALE cutting model were found in the literature [59, 60, 62, 73, 74]. The studies have focussed primarily on the effects of general machining parameters such as the effect of cutting edge radius, cutting speed, and the constitutive model on the residual stress profile. None of the studies using ALE included sequential cut, or tool wear effects.

2.4.2 White Layer Formation

In recent years there has been a renewed focus within the research community towards understanding the microstructural changes which occur within the surface layer of steels cut under aggressive conditions. The thin layer which typically appears

featureless when observed under an optical microscope is commonly referred to as white layer. This layer is typically only a few microns thick and is generally thought to be brittle. It is known to be composed primarily of a martensitic structure [52]. There are still opposing trends in regards to the effect that white layer has on fatigue life, Schwach and Guo [80] investigated the effect of white layer and found components without this layer had six times the fatigue life of ones with this layer. On the other hand Ramesh et al. [81] found that the compressive residual stresses induced by this white layer had the effect of significantly increasing fatigue life, which was found to be proportional to both the surface compressive residual stress and the maximum compressive residual stress in the specimen.

A substantial body of work or prior knowledge exists concerning the formation mechanisms of white layer in various material removal processes such as turning, grinding and electrical discharge machining (EDM). In general, white layer formation is explained through three processes, rapid heating and cooling, which leads to phase transformations, severe plastic deformation (SPD) which cause a very fine homogeneous microstructure, and lastly surface chemical reactions with the environment[82-85].

Early work in predicting white layer formation was achieved by assuming an analytical solution for a moving heat source, the problem was then treated as a purely thermally driven process [82]. More recently, however, advances in the FEA modelling of the cutting process has led to new contributions such as that by Ramesh and Melkote [55] who developed a model that treats white layer formation as a quenching problem by developing their own VUMAT subroutine for ABAQUS. There are however some

limitations to this work, for one it was assumed that as soon as an element exceeded the austenitization temperature it would transform. Also, the cutting model was based on *Lagrangian*, formulation meaning that a fracture criterion was needed which led to significant model tuning. Ranganath et al. [56] used a similar *Lagrangian* approach that captures the segmented chips found in hard turning in the prediction of white layer thickness. However the adiabatic slip captured in their model originates at the cutting edge which indicates that the fracture criteria still needs some improvements. Shulze et al. [86] developed what appears to be an interesting model based on a continuously re-meshed updated *Lagrangian* cutting model, but did not present any results only their methodology. Umbrello et al. [52] developed a continuously re-meshed updated *Lagrangian* cutting 2D model to predict white layer due to thermally driven phase changes in hardened AISI 52100 bearing steel. Their simulation results agreed well with experimental white layer depth measurements as well as with hardness profiles. Only Ramesh and Melkote [55] have attempted to reconcile the phase transformation (or white layer) predictions with the residual stress prediction.

In order help in optimizing machining conditions to allow for aggressive material removal, while limiting the negative influence of this phase transformed layer, it is desirable to develop models that allow for the identification of machining parameters that result in white layer not being formed or minimal white layer being formed.

2.5 Summary

After examining the current state-of-the-art, it is clear that significant progress has been made in the field of metal cutting predictions. Also, given that residual stress and microstructural changes are amongst the most commonly measured surface integrity parameters, there is keen interest in developing more accurate predictions of residual stresses in cases where microstructural changes occur.

Despite the significant body of work dedicated to the prediction of residual stresses in metal cutting, gaps exist in the reported literature. Residual stress prediction using ALE cutting models, particularly at small feed rates, has not received significant attention in the literature. Further, it is currently not possible to use the ALE cutting model to predict residual stresses if microstructural changes occur.

The focus of this thesis is therefore to address the prediction of residual stresses in three main areas, predicting residual stresses at small feed rates, a study on the sensitivity of residual stress predictions towards friction models and lastly a methodology for predicting residual stresses in metal cutting when microstructural changes occur.

Chapter 3:

General FEA Modelling of Metal Cutting

In this section the basic cutting model used throughout the thesis will be introduced and explained. The beginning of the chapter will focus on the fundamentals of assembling a finite element model of the cutting process; later parts of the chapter will focus on the details of the ALE model used for this work.

3.1 Introduction

The largest challenge in predicting the residual stresses induced in metal cutting is accurately simulating the cutting process itself. There exists a large body of previous work on this topic which goes back to simple cutting theories in the fifties. These are, however, not able to capture the complexities of the cutting process. Thus finite element methods are commonly utilized to analyze the process. Metal cutting is one of the most complex problems to model using finite element analysis. Not only is the problem of new surface generation usually highly mesh sensitive, but the majority of the complexities of the process occur within a localized region very close to the cutting edge. The strain and strain rates are very high, extreme temperature gradients are experienced, not to mention the problems of crack initiation and growth. All these factors combine to form a challenging highly nonlinear problem. The table below gives a comparison between machining and other manufacturing processes in terms of strain and strain rate.

Table 3-I: Comparison of Strain and Strain Rates for Some Machining Processes ([87])

Process	Typical Strain	Typical Strain Rate ($\frac{1}{s}$)
Extrusion	2 – 5	$10^{-1} - 10^2$
Forging/Rolling	0.1 - 0.5	$10^0 - 10^3$
Sheet Metal Forming	0.1 – 0.5	$10^0 - 10^2$
Machining	1 - 10	$10^3 - 10^6$

There are three main approaches to addressing the difficulties of simulating the metal cutting process, *Lagrangian*, *Arbitrary Lagrangian Eulerian* (ALE) and *Fully Eulerian*. All three methods have advantages and disadvantages which are presented with a simple explanation of each method in this section. However first a brief discussion is necessary on the time integration methods used.

3.2 Time Integration

A dynamic system with no damping can be described as:

$$M\ddot{U} + KU = F_e \quad (3-1)$$

Where M and K are the mass and stiffness matrix, and U and F_e represent the displacement and the externally applied force respectively. When solving this equation two different time integration schemes can be applied these are referred to as implicit or explicit time integration schemes.

For implicit solutions a backward time difference integration rule is used, which means that the displacement vector at the end of the first step ($U^{(1)}$) has to be estimated at the beginning of the step in order to achieve a solution. This approximation is done using

a variety of different methods. The choice thereof has a strong effect on the convergence rate of these simulations. After the initial estimate of the displacement vector a *Newton-Raphson* method is used to advance the solution iteratively. Convergence is determined by the reduction of the residual function (G) below a threshold criterion. The initial time step (Δt_0) is also assumed at the beginning of the solution and then subsequently adjusted throughout the solution based upon the convergence behaviour of the residual function. With rapidly converging solutions larger time steps can be used, whereas smaller time steps are required for the more slowly converging models often associated with larger non-linearity [88].

A further item of significance is that for implicit solutions the full system stiffness matrix needs to be formulated and integrated. This is done once at the beginning of the simulation in linear cases, however non-linear cases necessitate this at every time step in order to capture changes to the system stiffness. Similarly the mass matrix needs to be calculated and inverted at each time step as material non-linearity is simulated. All this means that for non-linear problems significant computation expense is associated with implicit methods, and even then the solutions may not converge for highly non-linear cases [89]. This makes implicit solutions to metal cutting processes slow and unattractive with solution times on the order of several days in some cases, depending on CPU of the computer system. A far more attractive solution from the standpoint of metal cutting is explicit time integration.

For explicit time integration, unlike the implicit case, no initial estimate of the displacement is required, rather the solution is advanced through knowledge of the

velocity and acceleration fields from the previous time step. This means that there is no convergence criterion or iteration during each time step. However there is a limit to how large individual time steps can be in order to yield an accurate solution. For a purely mechanical case this translates into the time step needing to be smaller than the time it takes a dilatation wave to cross the smallest element. This means the maximum time step is determined by material density, element stiffness and mesh size. There is however a risk with explicit formulations, since there is no residual calculated as part of the solution process. There is no inherent measure of the accuracy of the simulation. In other words, an explicit model will always yield a solution, however care has to be taken to ensure that this is a correct solution. With all FEA model results, validation is an important step, however, with explicit solutions this becomes particularly critical.

Since metal cutting is inherently extremely non-linear small time steps are requisite ($<10^{-10}$ s). However, reduced mathematical complexity of explicit formulation results in significant time savings over implicit formulations.

3.3 Lagrangian Formulation

In the *Lagrangian* formulation each node in the mesh grid is tied to a material point. This means that whatever deformation the material point undergoes the node will follow. Thus the node is associated with the same piece of material from the beginning of the simulation to the conclusion of the cutting process. A schematic of such a mesh is given below in Figure 3-1, where a simple mesh is subject to a pure shearing motion.

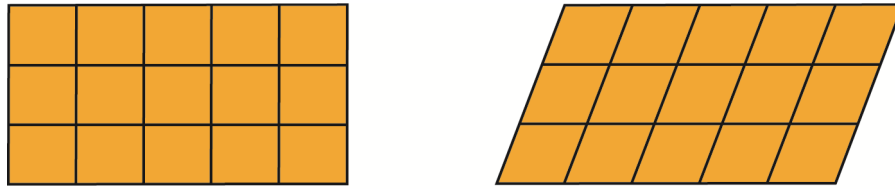


Figure 3-1: A Lagrangian Mesh in Pure Shear

This is the most commonly used formulation to simulate the metal cutting process. In order to construct a model for this, the workpiece is separated into two sections, as shown below in Figure 3-2. The nomenclature for these surfaces defined in this simulation are also indicated. The upper segment is the portion of the workpiece which will form the chip and the bottom segment will form the finished piece. The separation between the chip underside and the machined surface is the predefined crack path.

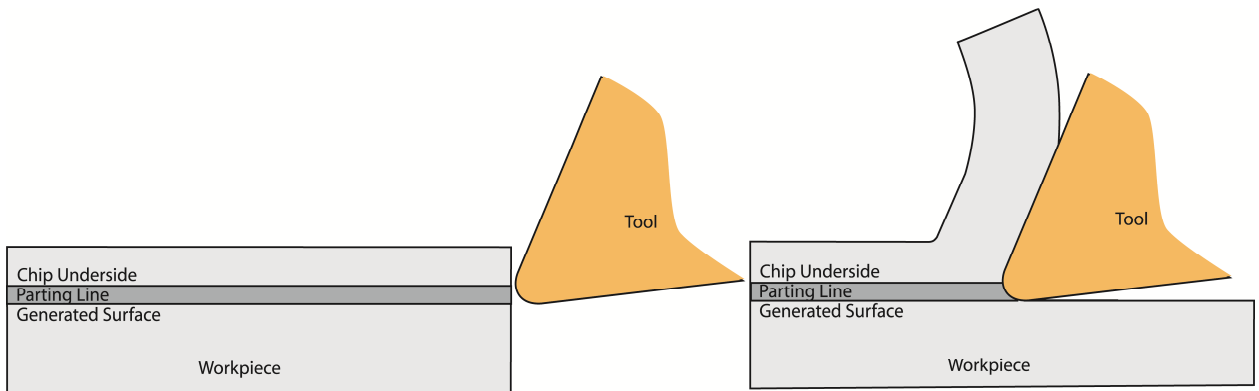


Figure 3-2: UL Segments

The undeformed chip and the machined surface are joined by a conditional link element. This is an element which has the same material properties as the rest of the workpiece but is allowed to fracture based on some fracture criterion. This fracture criterion is of primary importance in such a simulation and will be further addressed later in this section. A *Lagrangian* simulation with an excessively large mesh is shown below

in Figure 3-3 to elucidate the process, the conditional link elements have been highlighted in red.

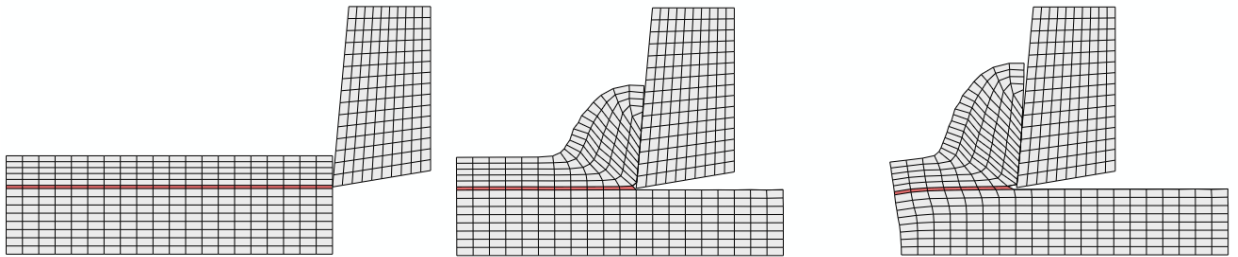


Figure 3-3: UL Simulation with Massive Element Size

If the chip being modeled is continuous the only elements allowed to fracture are the conditional link elements. However discontinuous chips require substantially more complex fracture criteria. One option for this is to use Recht's criterion which predicts catastrophic failure due to adiabatic slip. This happens when the thermal softening in the primary shear deformation zone overwhelms the strain hardening rate. The results is a catastrophic shear along the shear plane, yielding discontinuous chips [63].

Because there is no re-meshing in this formulation and the fracture path is pre-defined it is possible to generate inhomogeneous cutting models in which the very microstructure of the material being cut can be modeled to show its influence on chip formation [57, 58, 64].

There are however several disadvantages to the *Lagrangian* formulation, the most obvious one of these is the difficulty of selecting a suitable fracture criterion for the conditional link elements. Choosing both the type and values for the fracture criteria has great influence on the results obtained from the simulation. A number of different fracture

criteria have been used. They are all based on one of four principles, namely, maximum allowable nodal separation, threshold equivalent plastic strain, max allowable stress and strain energy density based criteria [45, 53, 78, 90-95].

A second disadvantage of this model type is that having predefined the fracture path there is no allowance made for a stagnant region or built up edge ahead of the cutting tool. This is however largely irrelevant as the formulation does not allow for anything but perfectly sharp tools. This is because near the cutting edge of a honed or chamfered tool the deformation of the elements becomes so severe that the solution becomes unstable. This presents the single largest disadvantage to this method in terms of its use for realistic cutting simulation. The lack of a cutting edge radius results in under prediction of the cutting forces, temperatures and of residual stresses. Despite these disadvantages the updated *Lagrangian* method is still frequently used due to its relative simplicity and ability to handle workpiece microstructure. However, the method is unsuitable for the purposes of residual stress prediction.

3.4 Eulerian Formulation

A fully *Eulerian* formulation is most commonly seen in fluid flow simulations, since for this type of simulations the mesh nodes are fixed to a specific coordinate and the material flows through it. This is illustrated below in Figure 3-4, where it can be seen that the material boundaries move, however the nodal positions remain fixed.

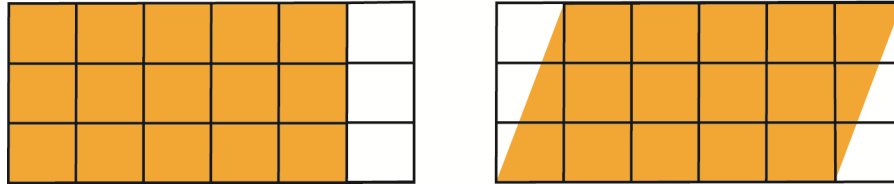


Figure 3-4: Fully Eulerian Mesh in Pure Shear

An *Eulerian* formulation is particularly attractive for metal cutting as very high strains are experienced and thus large mesh distortions are necessary. However, a serious drawback to this formulation is that the chip shape must be known *a priori*. This is because the mesh cannot move and is constrained to the initial geometry. To overcome this problem some iterative procedures have been investigated with limited success [96] [97], wherein an initial chip geometry is assumed and is adjusted based on the resulting boundary stresses. In terms of residual stress prediction there is, however, a very serious flaw to this formulation, which is that the material is modeled as viscoplastic. This ignores the elastic properties of the workpiece, thus residual stress prediction is simply not possible using an *Eulerian* approach [98].

3.5 ALE Formulation

Arbitrary *Lagrangian Eulerian* (ALE) formulation seeks to combine the advantages of both *Eulerian* and *Lagrangian* simulations. In ALE, nodes are neither fixed to the underlying material nor are they fixed in space. Instead the nodes are allowed to move in any arbitrary manner as defined by the user. Thus ALE is similar to adaptive re-meshing in that it seeks to optimize mesh quality throughout the simulation. However it is important to note that unlike adaptive re-meshing no new elements or nodes are created using ALE. It is simply a node motion scheme.

In the past ALE cutting models were designed by allowing unconstrained ALE mesh sweeps over the entire model; however this leads to poor mesh quality near the cutting edge of the tool. Furthermore the increased mesh distortion associated with large cutting edge radii causes robustness problems and computation time suffers [99]. These stability problems can be avoided by using a more structured approach to meshing. To this effect the workpiece is separated into four segments as shown in Figure 3-5. The mesh in three of these segments (shown in light grey) is allowed to flow freely, the mesh nearest the cutting edge (shown in dark gray) is however fully constrained in space as in a *Eularian* simulation.

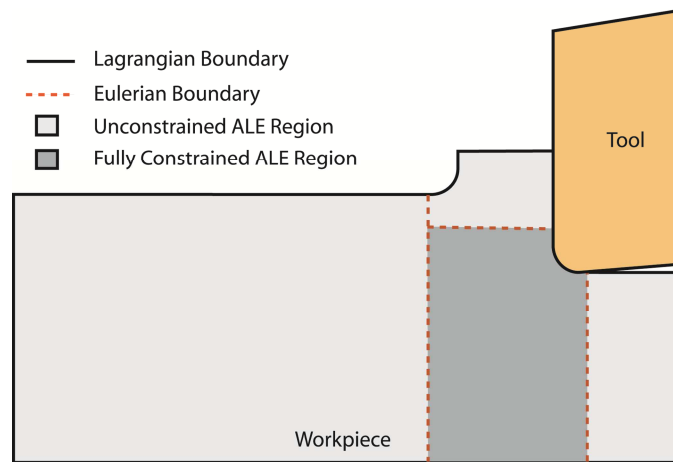


Figure 3-5: Partitioning Scheme for ALE

This configuration not only minimizes mesh distortion near the cutting edge but also forces chip separation, thus negating the need for a fracture criterion.

Not allowing for fracture no doubt ignores some of the specific cutting energy. However, from classical metal cutting principles this specific energy of surface formation

is known to be three or four orders of magnitude less than the total specific cutting energy [100].

From the partitioning scheme shown in Figure 3-5 it is evident that an initial chip is necessary for this formulation. However, it has been shown that this initial size has no effect on the steady state chip formed after the model has reached steady state cutting [74].

3.6 Material Models

Finding a suitable material model for simulating the cutting process is not a trivial matter, and a large body of work exist about this topic. The two material models which have found the most wide application when simulating metal cutting are an empirical material model proposed by Johnson and Cook [101] and a dislocation mechanics based model developed by Zerilli and Armstrong [102].

The *Johnson-Cook* material model is perhaps the most successfully applied model for the metal cutting process [103]. This model considers the material to be homogeneous, free of defects ,and defines its von Mises flow stress as a function of strain, strain rate and temperature. Each of the above independent and process variables are within the *Johnson-Cook* model expressed by their own term in this constitutive equation .

$$\sigma = (A + B\varepsilon^n) \left(1 + C \ln \left(\frac{\dot{\varepsilon}}{\dot{\varepsilon}_0}\right)\right) \left(1 - \left(\frac{T - T_r}{T_m - T_r}\right)^m\right) \quad (3-2)$$

Where the descriptions of the variables and parameters are given in Table 3-II below.

Table 3-II: Variables and Parameters of the *Johnson-Cook* Model

σ - Flow Stress	ϵ - Equivalent Plastic Strain	$\dot{\epsilon}$ - Equivalent Plastic Strain Rate
A - Initial Yield Strength	B - Strain Hardening Coefficient	n - Strain Hardening Exponent
C - Strain Rate Coefficient	$\dot{\epsilon}_0$ - Reference Plastic Strain Rate	T_r - Reference Temperature
T - Current Temperature	T_m - Melting Temperature	m - Thermal Softening Exponent

In this equation the first term corresponds to strain hardening, the second to strain rate sensitivity and the third term expresses the effect of thermal softening due to temperature rise of the workpiece.

Since the strain rates in metal cutting are large, conventional tensile testing is not a suitable approach for measuring the parameters required in the *Johnson-Cook* material model. Typically, to determine these parameters at high strain rates, a Split Hopkins Bar (SPHB) compression test is performed. In this methodology, the test sample is placed between the flat faces of two bars, one of which is explosively actuated to apply a pressure wave to the test sample. The sample is then compressed between the two bars as the pressure wave is transmitted. The displacement at the free end of the other bar is then measured and related to the stress time curve of the tested sample. This in turn can be expressed as a stress-strain curve for the material [104].

In order to evaluate all five of the *Johnson-Cook* parameters the stress strain curve needs to be completed over a range of temperatures and strain rates. At a minimum one additional temperature and one additional strain rate are required to determine the five parameters.

There are two ways in which the parameters are commonly extrapolated from the experimental data. The more rigorous method is to perform a weighted sum of squared differences between calculated and measured values, but this method is very lengthy since an absolute minimum has to be found by varying five constants. In lieu of this, stress-strain data is obtained by curve fitting data in which some parameters are held fixed. The A parameter in the *Johnson-Cook* model is simply the yield stress at the reference temperature and strain rate. Further, at the reference temperature and strain rate, the thermal softening and strain rate sensitivity terms disappear, reducing the model to simple power law hardening. As such, the B and n terms can easily be regressed. Then, by examining the measured stress data for cases where only one variable is left unconstrained, the material constant related to this unconstrained variable can be fitted [87].

In most materials, there is some interaction between the effects of thermal softening and the strain rate sensitivity, yet the *Johnson-Cook* material model separates the influence of these. This can lead to poor fit between the material model and measurements, particularly at conditions which significantly differ from the reference strain rate and temperature. For this reason it is important to perform material tests at strain rates similar to those of the process being investigated [87].

Given the variability in the microstructure of a given steel, based on previous processing or heat treatment, it is not surprising that significant inconsistencies can be found in the material parameters available in the literature for said steel. This is further complicated by the significant effect that the choice of reference strain rate and

temperature has on the regressed material parameters, particularly if the parameters are individually determined rather than through a least squares regression for all parameters. In fact the lack of reliable and consistent material data presents one of the most significant challenges in the simulation of metal cutting [44]. Since the *Johnson-Cook* material parameters have a significant effect on the predicted residual stresses, the choice of these parameters is crucial. For this reason a detailed study on the effect of varying the parameters of the Johnson-Cook material model on the predicted residual stresses was carried out by Nasr [126]. For the carbide tool, only the elastic properties were considered due to the brittle nature of the tool. The tool coating was also considered purely elastic.

3.7 Interfacial Friction

The typical shear stress distribution, first described by Zorev [100], are shown in Figure 3-6. This model of the interface remains the most accepted as it has been validated experimentally by both Shaw [100] and Oezel [70]. The shear limit imposed by this model represents the point at which the effective contact area approaches the apparent contact area, at which point the resistance to sliding exceeds the shear strength of the workpiece material and the material continuously shears at the interface instead of sliding.

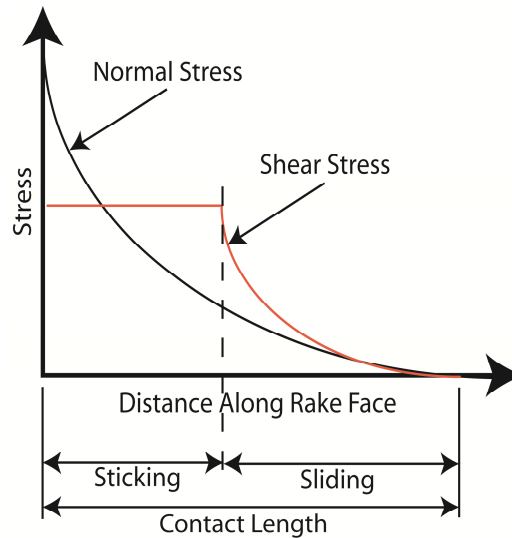


Figure 3-6: Normal Pressure and Shear Stress along Rake Face (Adapted from [100])

In attempts to capture this behaviour Yen et al. [105] applied a fixed room temperature shear limit value at the high pressure end of a simple coulumbic friction law. This was clearly unrealistic since the shear limit should be a function of temperature, strain and strain rate. An alternative to incorporating this shear limit is to assign a constant friction value to the workpiece elements at the tool-workpiece interface. At high contact pressures as the resistance to sliding approaches the shear strength of the material the element will shear. This shearing behaviour is controlled by the material model described above. So if the element is sufficiently small the interfacial shearing can be captured in the element. Thus the shear limit becomes a function of strain, strain rate and temperature, without the need for a complicated contact subroutine.

For this reason the tool-workpiece interaction for this work was modeled in ABAQUS as a contact pair, following a simple coulumbic friction law with a master-slave configuration. An isotropic coefficient of friction was assumed at 0.2, this was in order to

match average tribometer results for the same workpiece and tool material pairings. This means that for all the work presented in this thesis, the same friction model was used to characterize both the rake-chip interface, as well as the wearland-machined surface interface. In other words the secondary and tertiary deformation zones were characterized with the same parameters in each model.

In ABAQUS there are two contact algorithms which can be used to correct the slave penetration into the master surface, kinematic and penalty contact algorithms. These two methods differ in how they apply the correction to the slave nodes after penetration has occurred. The kinematic algorithm calculates a correcting acceleration which would have prevented the penetration and applies this in the next time step to the penetrating slave node. The penalty algorithm, however, calculates a fictional spring stiffness which when applied between the master and slave nodes would result in sufficient force to resolve the penetration. Thus, the penalty algorithm adds some stiffness into the model which in turn affects the maximum stable time increment, but the added benefit is that this formulation tends to be more numerically stable [106]. For the simulations considered in this work no instabilities were induced using the kinematic contact algorithm. However, for cases where contact instabilities develop, the penalty algorithm could be used at a numerical cost.

3.8 Heat Generation

There are two main types of heating which need to be considered in the cutting simulations; heat generation due to plastic work and that generated through friction.

The rate of heat generation (\dot{Q}_p) is determined as a fraction of plastic deformation energy, defined as [90]:

$$\dot{Q}_p = \eta \times \sigma \times \dot{\epsilon} \quad (3-3)$$

where σ is the flow stress, $\dot{\epsilon}$ the plastic strain rate and η the fraction of the plastic deformation energy converted to heat. Typically the fraction (η) is taken to be in the range of 0.85 and 0.95 [16, 24] .

Similarly, the heat generated through friction (\dot{Q}_f) is determined as a fraction of the frictional work that is converted to heat.

$$\dot{Q}_f = \psi \times F_f \times V_c \quad (3-4)$$

where F_f , V_c and ψ are the friction force, chip velocity and the fraction of the frictional energy that is converted to heat respectively [63].

In this work η and ψ were assumed to be 0.9. Ambient temperature was assumed to be 25°C and applied as initial conditions to all simulations. In terms of the cutting model, the predominant heat source is in the primary shear deformation zone where most of the plastic work occurs. However in the secondary and tertiary zones the heating is predominantly frictional.

3.9 Constraints

The constraints needed to affect the cut can be separated into boundary conditions, Figure 3-7a, and the ALE constraints, Figure 3-7b. The cutting tool is held fixed in two

directions along the back and top surface. This approach ignores the machine dynamics; these could be included by attaching tuned spring and damper elements on the tool. However, since the simulated time scale is very short, the dynamic response of the machine tool is ignored in the simulations. Therefore, phenomenon such as regenerative chatter and force response cannot be accurately captured as a result.

The cutting speed is applied at the workpiece for this cutting model. To this effect, the bottom of the workpiece is held fixed in the vertical direction and moved at the cutting speed in the horizontal direction, these boundary conditions are labelled in Figure 3-7a.

The specifics of the ALE constraints are also important in achieving a stable cutting mode. A re-meshing frequency of 10 re-meshing sweeps is used every 150 increments, with 300 initial sweeps. In terms of the spatial constraints, the workpiece was separated into four separate ALE regions with different constraints. The regions are: one fully constrained region near the cutting edge, two partially constrained regions each side of the fixed region and then the remaining unconstrained elements. These regions are labelled in Figure 3-7b.

The fully constrained region near the cutting edge prevents the mesh deformation associated with the stagnation region. The partially constrained regions are fixed only in the vertical direction in order to allow for a more dense mesh near the surface of the workpiece. Without these regions the ALE algorithm would redistribute the initial mesh grading to be uniform through the whole workpiece. The unconstrained regions are left

free to re-mesh in order to achieve a smooth mesh despite the large volumetric changes experienced as the chip is formed.

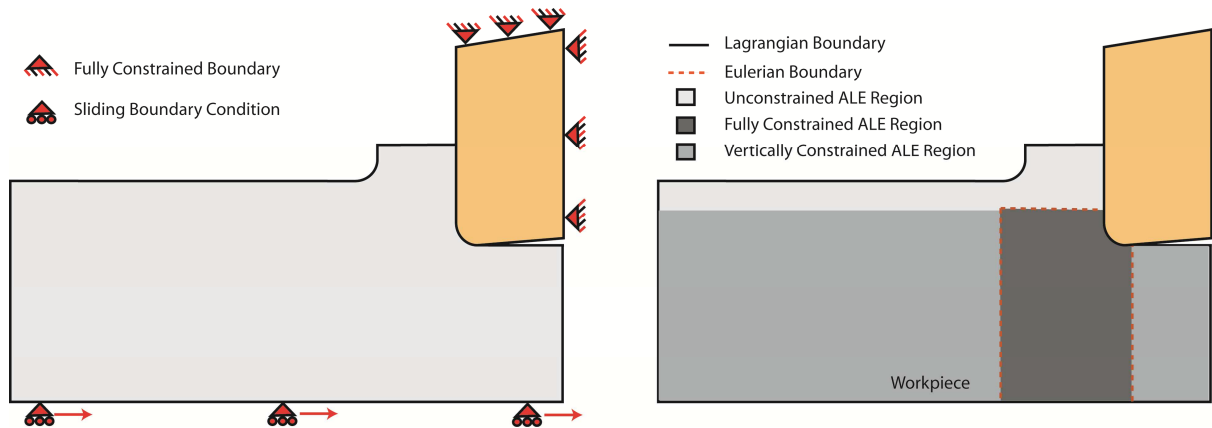


Figure 3-7: Boundary Conditions and ALE Constraints

3.10 Thermal Relaxation Module

When simulating residual stresses the tangential stress profile is of main interest, since this is the stress that most affects crack propagation [74]. Before this solution variable can be taken from the ALE model a relaxation step is introduced within ABAQUS to relax the mechanical boundary conditions. After the mechanical relaxation step, there is still a temperature gradient in the part. Therefore, a thermal relaxation step is required. The time scales associated with the thermal relaxation are several orders of magnitude larger than the cutting time, thus a fully explicit relaxation of the entire cutting model would take a substantial amount of computational time. Instead, a small slice of elements is extracted from the newly formed workpiece. The temperatures and stresses for these elements are output and the relaxation is then handled in MATLAB. The problem reduces to one dimensional heat diffusion. Since the time scales are still quite small the effects of convection were considered negligible, and the problem was treated

as pure self-quenching. Also the temperatures after the initial mechanical relaxation are small (<300 °C) allowing the thermal changes to be coupled with the stress field through simple elastic behaviour. That is to say the relaxation does not enter the plastic regime. Thus the stress increment at any time $\dot{\sigma}$, can simply be calculated with Equation (3-5) where E is the Young's modulus, T is the local temperature and \dot{T} is the rate of temperature change and α is the thermal expansion coefficient.

$$\dot{\sigma} = E(T)\alpha(T)\dot{T} \quad (3-5)$$

Where thermal history is of no concern there is no need to solve the one dimensional problem, the starting and ending temperatures are all that is needed and a constant increment can be used in Figure (3-5). Further if $E(T)$ and $\alpha(T)$ are integrated to yield an average value over temperature range during cooling, the total stress increment due to thermal relaxation can be determined without the need for incrementing, The total stress increment due to thermal relaxation is given by Equation (3-6 where, T_E is the temperature of the element extracted from the ALE cutting model and T_R is the final relaxation temperature, which is usually room temperature.

$$\sigma_{TR} = E_{avg}\alpha_{avg}(T_E - T_R) \quad (3-6)$$

Chapter 4: Experimental Procedure

In this chapter the laboratory work for obtaining the cutting forces and residual stress profiles for this work is discussed. The main purpose of these measurements was for the validation of two dimensional cutting models, thus orthogonal cutting test were performed, and analysed. The cutting tests themselves are described first, followed by the measurement techniques.

4.1 Cutting Tests

In order for the experimental cutting tests to match the two dimensional simulations, so called orthogonal cutting tests are required. In this work, this was achieved by turning thin disks of the workpiece, shown schematically in Figure 4-1. As long as the feed per revolution is kept below one-tenth the width of a rib, the material side flow is minimal and the process can be treated as a plane strain deformation process [100].

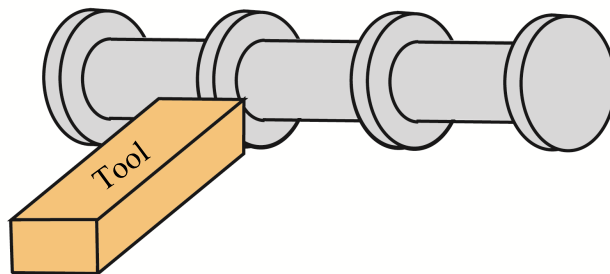


Figure 4-1: Schematic of Rib Turning

Grooves were machined into a cylindrical workpiece bar, as shown in Figure 4-2 below. The grooves were then machined as part of the experimental validation study of the orthogonal cutting process. A six inch bar of AISI 4140 was chosen for the experimental study.

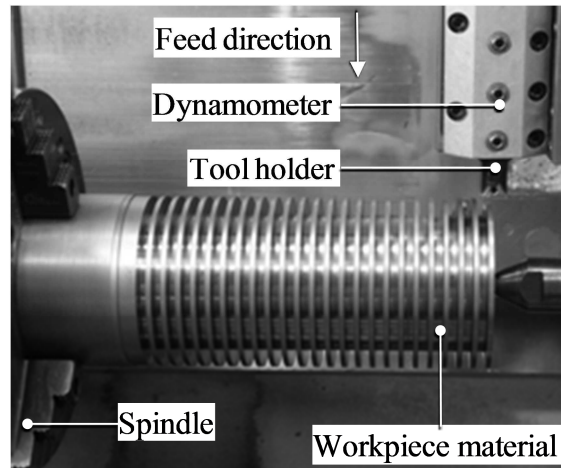


Figure 4-2: Orthogonal Cutting Setup

Orthogonal dry cutting tests were carried out on the Boehringer VDF-180cm CNC Lathe with a continuous variable speed control from 0 to 4,500 rpm and a maximum spindle power of 37.3 kW. Cutting forces were measured using a Kistler three component stationary piezoelectric dynamometer (type 9121, calibrated range: $F_x = 0 - 3,000$ N, $F_y = 0 - 3,000$ N, and $F_z = 0 - 6,000$ N), connected to a series of charge amplifiers (type 5011A, with a frequency limit of 200 kHz). Data acquisition was accomplished using an analogue to digital converter card connected to a high performance computer, which was capable of sampling at 200 KS/sec per channel.

4.2 Workpiece and Tool Materials

The results obtained in this thesis are organized into the next 3 chapters (5-7). These chapters are concerned with small uncut chip thicknesses (Chapter 5), effects of choice of friction model (Chapter 6) and the influence of phase transformations (Chapter 7)

Each of these chapters warranted different workpiece and tool materials. For chapters 5 and 6, the workpiece material used was hot rolled AISI 1045 with a chemical composition of 0.43-0.46% C, 0.40% Si, 0.65% Mn, 0.10% Mo, 0.40% Ni and Fe balance. However, when cutting this material, the temperature reached was insufficient to induce surface phase transformations. Therefore a different material, AISI 4140 with a chemical composition of 0.38-0.43% C, 0.75% Mn, 0.80% Cr, 0.15% Mo, 0.15% Si and Fe balance, was selected for the phase transformation study presented in chapter 7. AISI 4140 was chosen because it cut with continuous chips under conditions that induced phase transformations.

The cutting tools used for all sets of experiments were made of cemented tungsten carbide, but the tool for the first phase was PVD coated with TiAlN-TiN to prevent any tool wear during testing, inserts were inspected after cutting to ensure no appreciable wear had occurred. Further, to ensure minimal variation between cutting edge radii inserts were taken from the same batch. Since tool wear was desirable for the second and third phases, uncoated tools were used. In all cases the inserts used were triangular flat faced inserts (TNG type)

A brief summary of the workpiece and tool material as well as tool coating can be found in Table 4-I.

Table 4-I: Workpiece and Tool Materials

	Chapter 5	Chapter 6	Chapter 7
Workpiece	AISI 1045	AISI 1045	AISI 4140
Tool	WC	WC	WC
Tool Coating	TiAlN-TiN	None	None

4.3 Tool Wear Measurement

In order to quantify the tool wear and accurately measure the actual profile of the cutting edge, inserts were assessed both before and after cutting.

A Nikon AZ100M optical microscope with an automatic Prior ProScan II stage was used to capture images uniformly spaced in the vertical direction (1 μ m spacing). This image stack was then processed into a 3D surface of the cutting edge using Nikon NIS Elements. The average geometry across the width of cut was curve fit using a b-spline. A tool developed by Youssefian and Koshy [107], was used to represent the cutting edge as contour based parameters. Flank and crater wear were determined by straight line regressions to the average shape. Where tool wear is measured and integrated in the cutting model, the simplified worn geometries are shown in the relevant chapters (6 and 7).

4.4 Residual Stress Measurement

Despite a number of existing techniques that are able to measure residual stress depth profiles in a non-destructive manner, X-ray diffraction coupled with etching remains the industrial standard. This combined with the difficulty of access to many of the newer techniques resolved the choice of X-ray diffraction as the measurement technique used in this work.

In order to obtain depth profiles of the residual stresses remaining within the machined discs, residual stress measurements in the hoop direction were taken using a X-ray diffractometer (XSTRESS 3000). The radiation source used was Cr K α with a 2 mm diameter spot size. Electrochemical etching (20% perchloric acid + 80% ethanol) was employed to remove surface and sub-surface layers for the depth profile measurements. These measurements were taken out of house by an ISO 9001:2008 certified company. As a matter of procedure the measured residual stress profiles were only revealed upon completion of the residual stress prediction and the comparison was then made under supervision. Further, residual stress measurements of the annealed AISI 1045 sample were to establish the initial state of the workpiece. These measurements are given in Appendix I. The residual stresses recovered to neutral at a depth of 70 μm , however since the material was cut to a depth of approximately 10 mm these measurements are not critical to the work performed.

4.5 Experimental Test Matrix

As mentioned earlier, this work is separated into three separate sections each discussed in its own chapter (Chapters 5, 6 and 7). Each one of these required slightly different cutting parameters, the test matrix for each of these sections is given in tables within the relevant chapter. All the testing parameters were selected to ensure that chips were continuous, that cutting was stable and chatter did not occur. In the first two cases, as detailed Table 5-III and Table 6-II, it was also imperative that no phase transformations occurred, whilst the opposite was true of the last case, as shown in Table 7-III. For the second and third sections cutting had to be sufficiently aggressive to incur significant tool wear within the cutting time.

Chapter 5:

Residual Stress Prediction when using Small Uncut Chip Thicknesses

In this chapter a sequential cut module is introduced in order to predict residual stresses when using small uncut chip thicknesses. The residual stress profiles predicted using this module are compared to experimentally obtained values.

Since the experimental work and test matrix is already discussed in Chapter 4, this chapter begins by discussing the particulars of the cutting model used in this work, focusing on the specific parameters used within the framework of the basic cutting module described in Chapter 3 as well as on the sequential cut module, the results of which are then discussed.

5.1 Model Details

5.1.1 Metal Cutting Simulation Module

The general finite element model used for this work was discussed earlier in detail in Chapter 3. However this section will discuss the unique additions to the model for residual stress prediction when using small uncut chip thickness as well as the specific parameters needed for the accurate simulation.

The *Johnson-Cook* material model was used to mathematically describe the workpiece material homogeneous plasticity behavior as a function of strain, strain rate and temperature as shown again in (5-1, where the individual terms in square brackets

were described earlier in Chapter 3. The constants used in this work are listed in Table 5-I where the first term corresponds to strain hardening, the second to strain rate sensitivity and the third term expresses the effect of thermal softening.

$$\sigma = [A + B\epsilon^n] \left[1 + C \ln \left(\frac{\dot{\epsilon}}{\dot{\epsilon}_0} \right) \right] \left[1 - \left(\frac{\theta - \theta_r}{\theta_m - \theta_r} \right)^m \right] \quad (5-1)$$

Table 5-I: AISI 1045 Johnson Cook Material Constants [105].

A (MPa)	B (MPa)	n	C	$\dot{\epsilon}_0$ (s ⁻¹)	θ_m (°C)	m
553.1	600.8	0.243	0.0134	1	1400	1

Due to the brittle nature of the carbide material, only elastic properties of the PVD coated tool were considered. Table 5-II lists the mechanical and physical properties of the tool and coating materials.

Table 5-II: Tool Substrate and Coating Materials Mechanical and Physical Properties.

	Substrate Material (94% WC – 6% Co) [105]	Tool Coating TiAlN [108]
Modulus of elasticity (GPa)	612	370 (20 °C) 350 (250 °C)
Poisson's ratio	0.22	0.1709
Specific heat capacity (J/kg K)	334.01 + 0.12 θ	518
Thermal conductivity (W/m K)	86	50 (20 – 800 °C)

5.1.2 Sequential Cut Module

Using the methodology outlined in section 3.10 the residual stresses for a cut can be predicted. In addition to the stresses calculated in this manner the plastic strain must be saved to be later used as the initial conditions for the second pass.

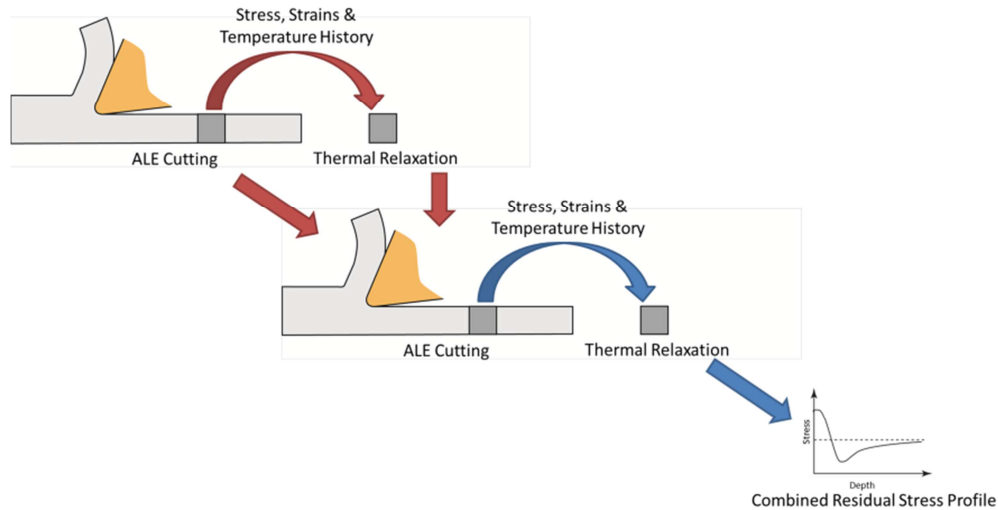


Figure 5-1: Schematic of the Sequential Cut Module

In order to implement a sequential cut module the most complicated part is how to impart the workpiece history from the first pass to the second pass, while solving for the thermal relaxation in a different solver. This requires using the predicted residual stress depth profile, as well as the equivalent plastic strain (PEEQ) as the initial condition for the second pass. After the relaxed stress distribution is calculated in the thermal relaxation module, the solution variables are applied to the ALE cutting model as an initial field. This is achieved by outputting the ABAQUS mesh file to MATLAB, where the coordinate of the centroid of each element is determined in order to interpolate the various element fields (stresses and equivalent plastic strain) for the entire workpiece. Once these initial fields have been defined, a new solution step is required before the cutting simulation can be started. The interpolation of solution variables can lead the

solution to be non-equilibrium. Therefore a step is required in which all nodes are held fixed, and the stress solution is allowed to equilibrate. After this step the previous boundary conditions are applied again in order to affect the second cut. This step is then relaxed in the exact same manner as the first cut to obtain the final residual stress profile. This is schematically illustrated in Figure 5-2.

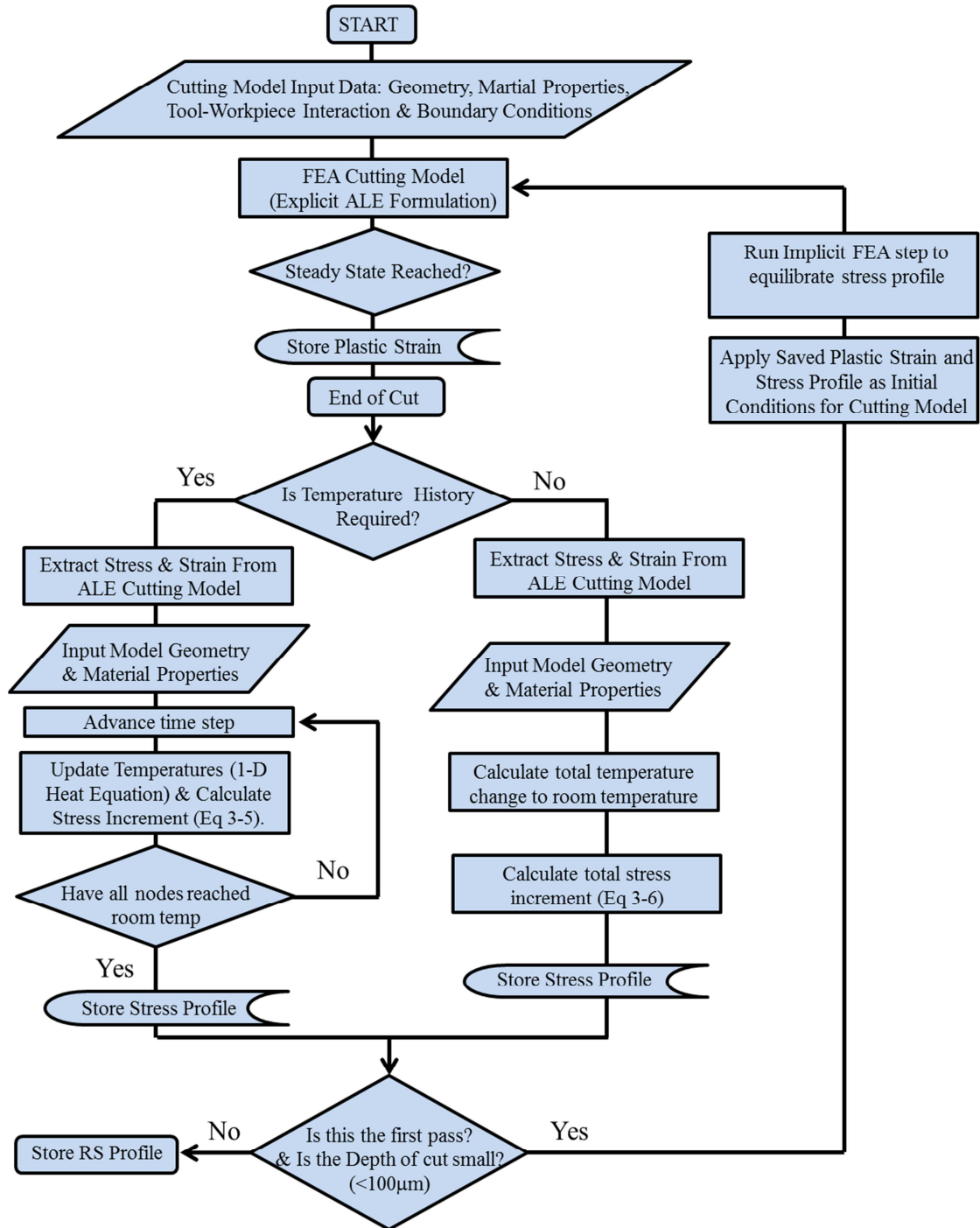


Figure 5-2: Flowchart of Sequential Cut Procedure

Table 5-III list the simulation test matrix and eight models will be presented. The simulation parameters are exactly the same as the experimental parameters listed in Chapter 4. Four simulations were performed without the sequential cut module and four with the sequential cut module.

Table 5-III: Simulation Test Matrix.

Cutting speed (m/min)	100		200	
Undeformed chip thickness (mm)	0.07	0.14	0.07	0.14
Without sequential cut module	Model 1	Model 2	Model 3	Model 4
With sequential cut module	Model 5	Model 6	Model 7	Model 8

5.2 Results and Discussion

Figure 5-3 shows the residual stress profiles, in the hoop direction, at 0.07 mm undeformed chip thickness at cutting speeds of 100 m/min and 200 m/min. The error bars indicate the deviation in the measurement at each depth. Since the x-ray spot size encompasses a number of different workpiece grains, some scatter in the measured residual stresses values is expected. Also since the x-ray measurement is taken over a penetration depth of around 5 μ m some further scatter is inherent. The combination of these two reasons lead to the significant scatter observed in Figure 5-3.

At the machined surface, both residual stress profiles were tensile. The profiles changed to a compressive state at a depth of about 10 μ m. At the lower speed, the tensile residual stresses penetrate deeper into the machined surface in comparison to the higher

cutting speed. Similar trends of cutting speed versus residual stress profile were reported in AISI 316L steel [79]. This was likely due to higher heat flux flowing into the workpiece material at the lower cutting speed. Figure 5-4 shows the temperature distribution beneath the newly machined surface obtained from the FE model at the same process simulation time. The difference in surface temperature for the two cutting speeds was less than 15 C. However at a depth of 25 μ m the temperature difference increased to about 60°C when the average temperature dropped by around 200°C. This indicates that the heat flux flowing into the workpiece material was higher at the lower cutting speed. This is perhaps due to increased time taken for the cutting edge to move across the machined surface compared to the higher cutting speed. Because the workpiece material is strain rate insensitive, a significant increase in work is not expected, as such increased temperatures are not expected. Also the increased speed leads to decreased interaction time between the chip, tool and workpiece, this would cause lower temperatures beneath the machined surface for the higher cutting speed.

The reduction in thermal softening experienced at higher cutting speeds, explains the increased compression observed in the residual stress profile.

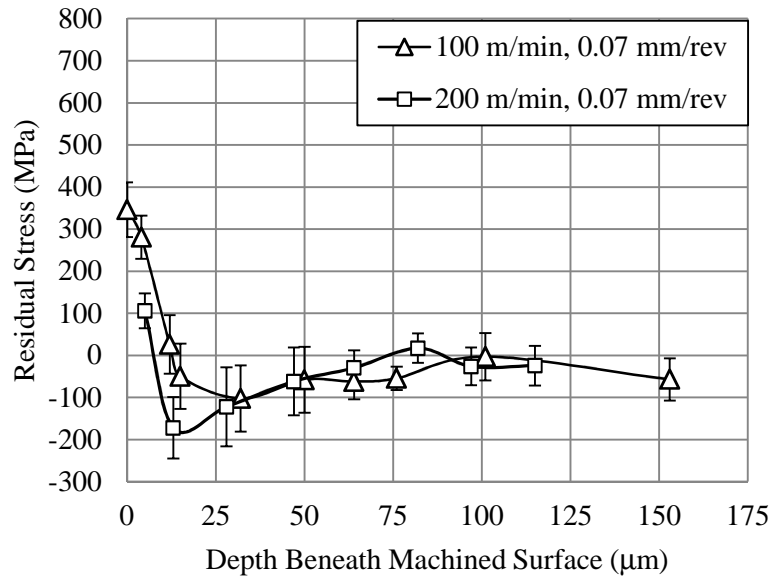


Figure 5-3: Experimentally Measured Residual Stress Depth Profile at Fixed Undeformed Chip Thickness of 0.07 mm at 100 m/min and 200 m/min Cutting Speed

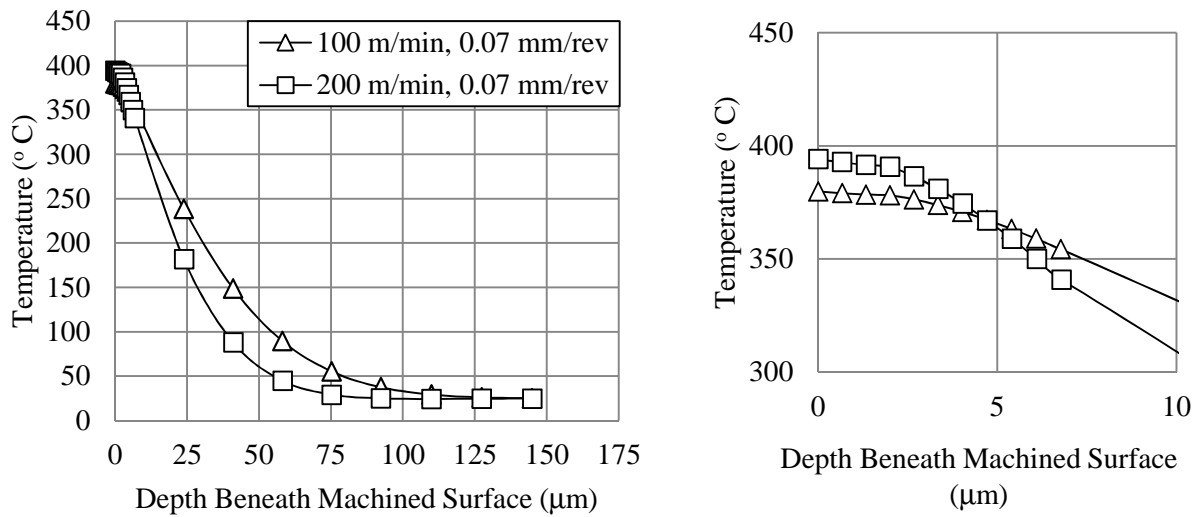


Figure 5-4: Effect of Cutting Speed on Temperature Distribution Beneath the Newly Machined Surface

Figure 5-5 shows a comparison between measured and predicted residual stresses profiles with and without the sequential cut module at a cutting speed of 100 m/min and

0.07 mm undeformed chip thickness. The residual stress profile with the sequential model is clearly much closer to the experimental data compared to the one without. This is attributed to the increased sensitivity of the residual stress profile to the pre-existing conditions of the workpiece, arising from the preceding cut. Therefore, in order to improve the accuracy of the predicted residual stresses, inclusion of the sequential cut module in the analysis is critical. Also the sequential cut module, resulted in decreased penetration depth of the tensile layer compared to the prediction without the sequential cut module. Ee et.al. [13] found that the residual stresses were tensile but decayed more quickly with distance from the surface to zero in the second cut compared to that without the sequential cut, which was similar to the trend observed in Figure 5-5. Similar trends were also reported by [47].

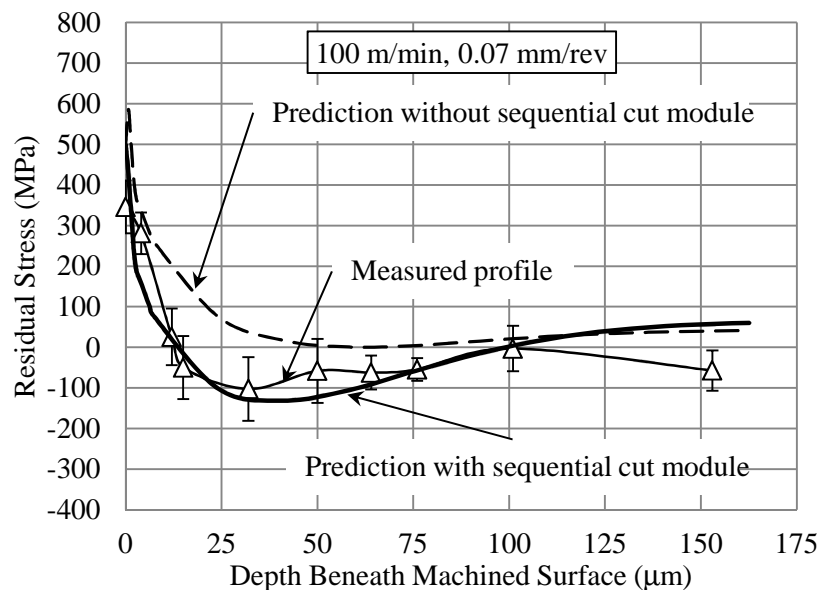


Figure 5-5: Comparison Between Measured and Predicted Residual Stress Profile at 100 m/min Cutting Speed and 0.07 mm Undeformed Chip Thickness

Figure 5-6 shows the temperature profile beneath the newly machined surface after passing through the cutting edge. It was observed that the temperature and penetration depth after the sequential cut module were higher than those in the case with no sequential cut. However, the maximum temperature difference was less than 50 C, which is at a depth of 50 μ m. Therefore it can be concluded that the stress induced by the thermal loading cannot have such a significant effect on the residual stress profile. Furthermore, for the higher temperature profile with the sequential cuts, the residual stresses should be more tensile compared to the case with no sequential cuts. This is contrary to the simulated residual stresses results in Figure 5-5.

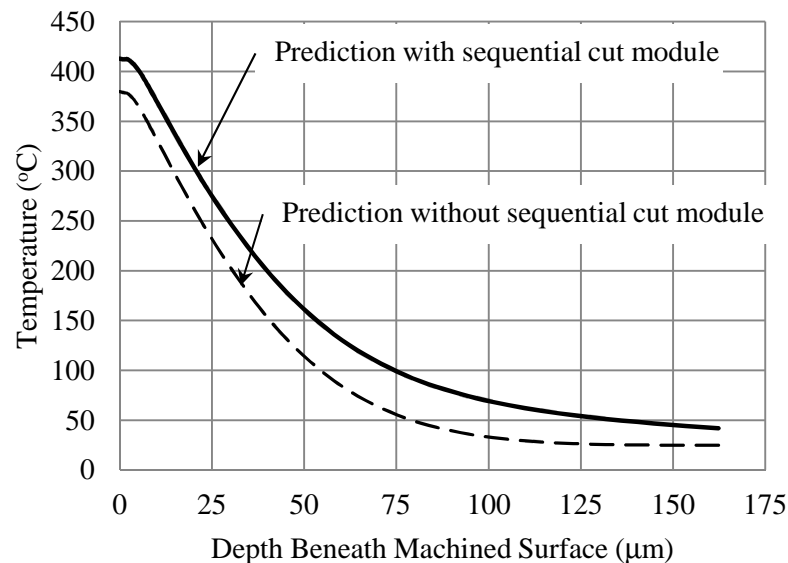


Figure 5-6: Temperature Profile Beneath the Newly Machined Surface after Passing through the Cutting Edge at 100 m/min Cutting Speed and 0.07 mm Undeformed Chip Thickness.

Since the temperature history is known, the residual stress induced purely by thermal means can be estimated using a decoupled thermal relaxation module. By subtracting this estimate from the total predicted residual stress the mechanically induced

contribution towards the total residual stress profile was obtained. This yielded a simple way of analysing the relative magnitude of the mechanical and thermal contributions to the total residual stress profile.

Figure 5-7 shows the thermal and mechanical induced stress distributions beneath the newly machined surface. As expected, the thermal induced stresses with and without the sequential cut module were similar. However, the mechanical induced stresses were more compressive and the penetration depth deeper with the sequential cut module. Therefore, with the sequential cut module, the predicted residual stresses were more compressive when compared to without the sequential cut module.

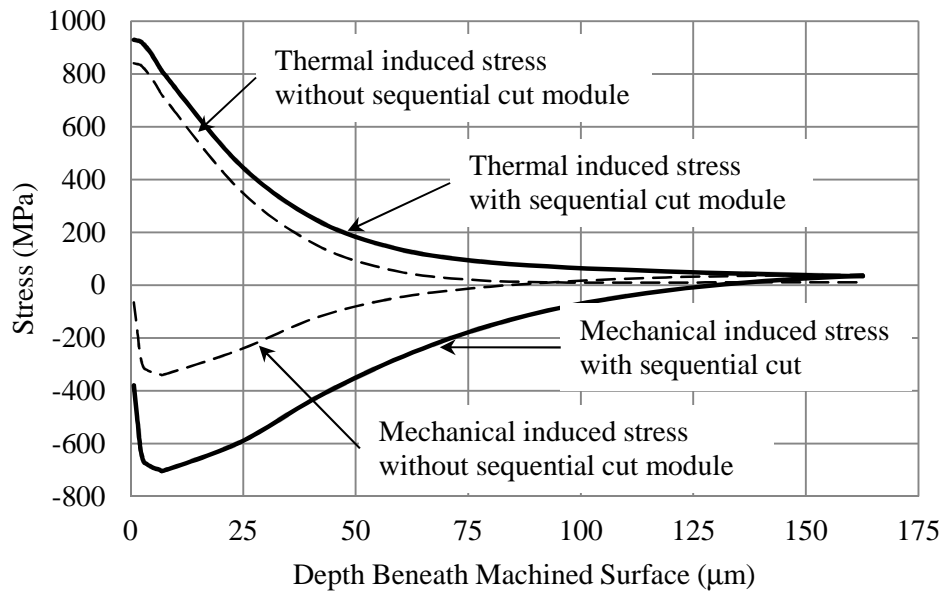


Figure 5-7: Thermal and Mechanical Induced Stress Distributions Beneath the Newly Machined Surface for 100 m/min Cutting Speed and 0.07 mm Undeformed Chip Thickness.

Higher mechanically induced stresses from the sequential cut module are due to the pre-existence of residual stress field generated from the previous cut. With the

sequential cut module, the residual stress field generated from the previous cut was incorporated into the cutting model. The detail residual stress field is shown in Figure 5-5 (dashed line). The predicted tensile residual stress profile without the sequential cut module was $\sim 50 \mu\text{m}$ deep. This implies that the sub surface hardness must be higher than the bulk material. This was also observed by [109] when turning AISI 1045 in the annealed state at 100 m/min cutting speed and 0.1 mm undeformed chip thickness. Han measured the micro-hardness with the machining parameter mentioned earlier and found that the sub surface hardness was 15 % higher than the bulk hardness. The higher hardness is usually associated with the A value from Johnson Cook material constitutive equation, which was the initial plastic flow stress at zero plastic strain, see (5-1). With higher hardness magnitude, the stress and energy required to strain the material increases. This is schematically illustrated in Figure 5-8 where the stress and energy generated with and without the pre hardened layer are compared.

Figure 5-9 shows the effect of including the sequential cut module on temperature distribution through the chip. By including the sequential cut module higher temperature were generated at the free surface of the chip. This was due to the material hardening that was generated from the previous cut. When including the residual stresses from the previous cut, the energy generated from plastic deformation was higher as shown in Figure 5-8 (c). Towards the cutting edge, the temperature generated with the sequential cut module did not show any substantial difference. This was because the penetration depth of the residual stresses was only $\sim 50 \mu\text{m}$ from the free surface. Figure 5-10 compares the cutting force from experimental results and prediction with and without

sequential cut module for various cutting speeds and depth of cut. At 0.07 mm/rev, the prediction with sequential cut module was higher when compared to the case of no sequential cuts. This was likely due to the pre hardened sub surface of the workpiece material.

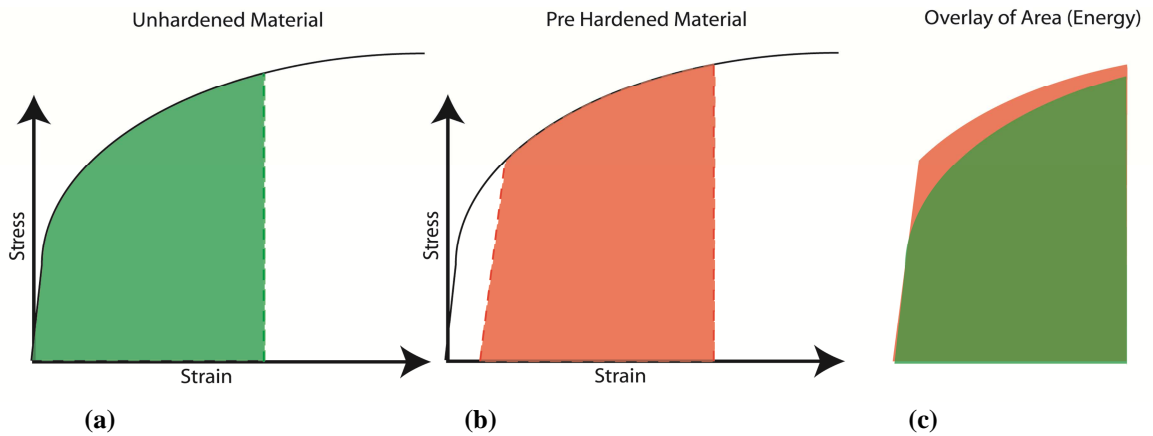


Figure 5-8: Schematic of Stress and Energy Released in Pre-Hardened Layer.

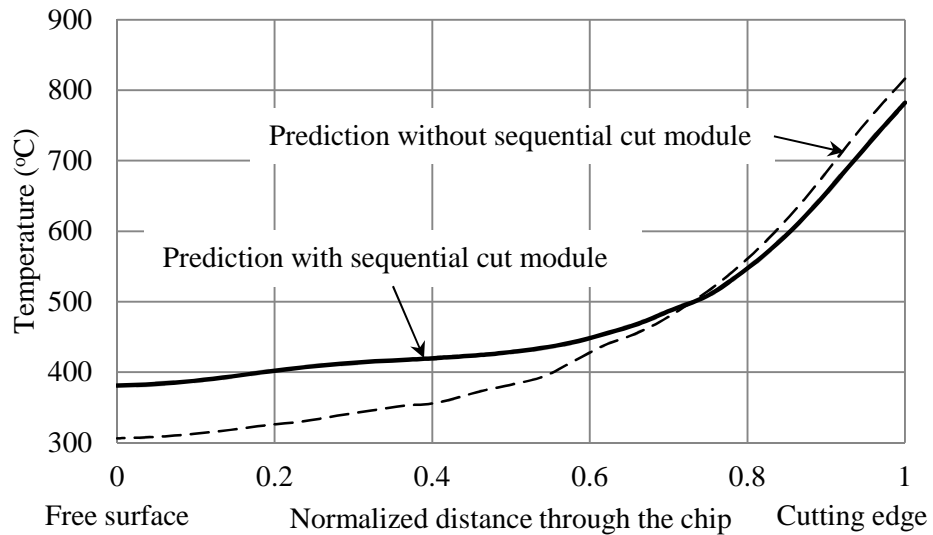


Figure 5-9: Temperature Distribution through the Chip at 100 m/min Cutting Speed and 0.70 mm Undeformed Chip Thickness

Figure 5-11 compares the residual stress profiles both with and without the sequential cut modules with experimental results at 200 m/min cutting speed and 0.07 mm undeformed chip thickness. The prediction with the sequential cut module agreed substantially better with experiments than those without the sequential cut module. This trend was similar to that found in Figure 5-5. However, when the undeformed chip thickness was increased to 0.14 mm, as shown in Figure 5-12 and Figure 5-13, both at 100 m/min and 200 m/min cutting speed, the sequential cut module did not have a significant effect on the residual stress profiles. At the high undeformed chip thickness of 0.14 mm, the cutting edge is engaging the workpiece material that was not affected by the previous cut residual stresses. From Figure 5-12 and Figure 5-13, the penetration depth of the residual stresses is $< 80 \mu\text{m}$, and the undeformed chip thickness used was 0.14 mm.

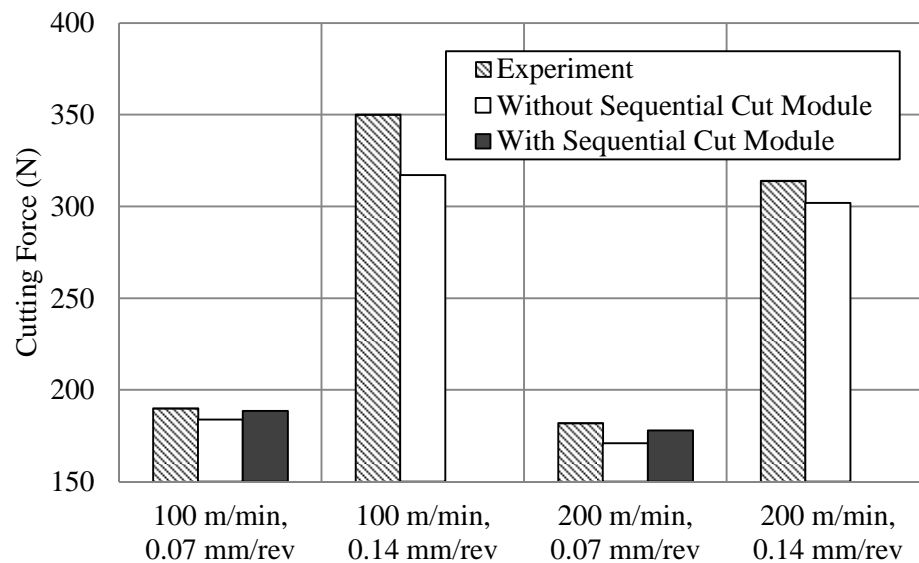


Figure 5-10: Effect of Process Parameters on Experimental and Predicted Cutting Forces.

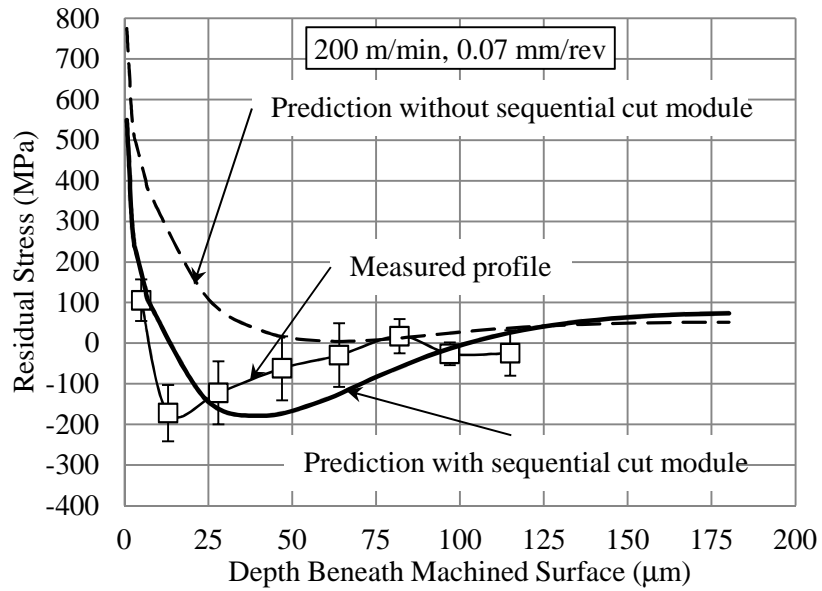


Figure 5-11: Comparison Between Measured and Predicted Residual Stress Profile at 200 m/min Cutting Speed and 0.07 mm Undeformed Chip Thickness

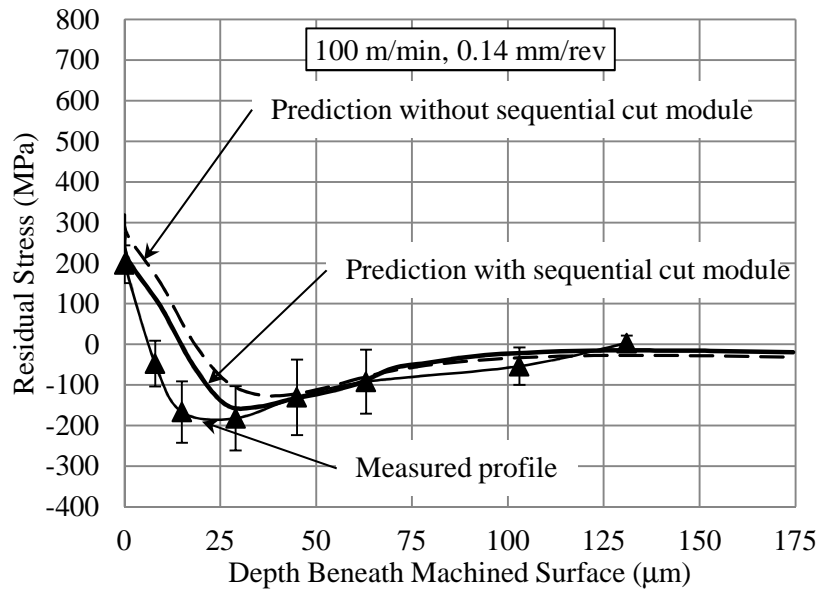


Figure 5-12: Comparison Between Measured and Predicted Residual Stress Profile at 100 m/min Cutting Speed and 0.14 mm Undeformed Chip Thickness

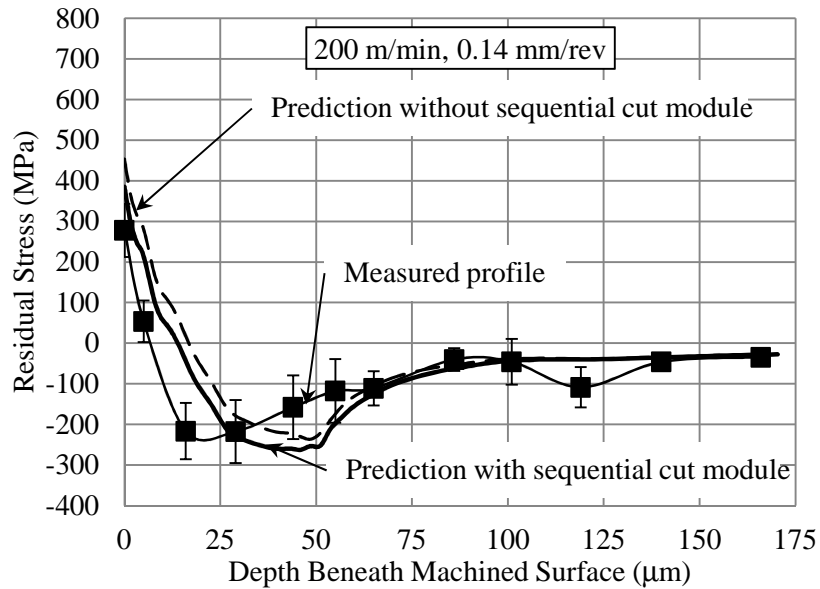


Figure 5-13: Comparison Between Measured and Predicted Residual Stress Profile at 200 m/min Cutting Speed and 0.14 mm Undeformed Chip Thickness

Due to the larger undeformed chip thickness, the residual stresses generated from the previous cut have little influence on the cutting mechanics and thus the residual stress profile with and without the sequential cut module were very similar. At 0.07 mm undeformed chip thickness, the residual stress penetration depth can be as deep as 60 μm . Therefore, a large fraction of the undeformed chip thickness is affected by the residual stresses generated from the previous cut, which is included in the sequential cut model. Hence the residual stresses showed a significant difference between with and without the sequential cut module. At 0.14 mm undeformed chip thickness, only a smaller fraction of the uncut chip thickness has a residual stress profile, which was transferred from the previous cut. Therefore, the sequential cut module has little influence on the residual stress profile. In general, at the higher undeformed chip thickness, the magnitude of measured compressive residual stresses was higher when compared to the lower

undeformed chip thickness. This was likely due to higher cutting forces (see Figure 5-10), i.e., mechanical loading induced on the workpiece at higher undeformed chip thickness. Increasing the cutting speed did not change the surface residual stress magnitude significantly. This was likely due to AISI 1045 insensitivity to strain rate.

Chapter 6: Effect of Friction Models on Residual Stress Prediction

A suitable choice of friction model is critical to any cutting simulation. However the literature contains often inadequate and contradictory results [80] [81]. This chapter will focus on the effect of choice of friction model on the simulation output, particularly in terms of cutting forces and residual stresses. Incorporation of several different friction models in the cutting model is discussed as well as a brief summary of the modelling parameters used. This is followed by a more detailed discussion of the friction at the tool-chip interface, and then a discussion of the results.

6.1 Model Details

6.1.1 Friction at the Tool-Chip Interface

As discussed in Chapter 3, the frictional characteristics within the tool-chip interface have been studied empirically, in some detail, for more than a half century, most famously by *Zorev* in 1963 [100]. In his seminal work typical normal and shear stress distributions for this interface were measured using split tool techniques. The cutting tool was separated into two separate parts, the resulting forces were measured at each tool. By varying the location of the split in the tools the stresses at the interface can be mapped. These distributions have since been validated by numerous researchers [70] [100]. From this work it is known that despite a monotonically increasing normal stress distribution, the shear stress (τ_f) reaches a limit beyond which it no longer increases, a

shear limit (τ_p). The typical distribution is depicted in Figure 3-6. According to this model sticking occurs near the tool tip, and the workpiece slides freely over the remaining region. Using standard Coulomb friction for the sliding region the interface can be characterized by two distinct regions:

$$\begin{aligned}\tau_f(x) &= \tau_p \text{ when } 0 < x < l_p \\ \tau_f(x) &= \mu\sigma_n(x) \text{ when } l_p < x < l_c\end{aligned}\tag{6-1}$$

where x is the distance from the cutting edge, l_p is the length of the sticking zone and l_c is the length of the contact between the tool and chip.

Although the conditions in the tool-workpiece interface are well known through experimental work, how to implement it in a model remains contentious. Since friction is the focus of this chapter, the essential features of friction models commonly used in FEA of metal cutting are discussed below. In industrial environments, most cutting is performed in the presence of some lubrication. In the past this was of the flood type, whereby the entire work zone is flooded with liquid coolant. At present, efforts are made, for primarily environmental reasons, to eliminate flood cooling in favour of minimum quality lubrication (MQL). Current knowledge on the effect of these cutting fluids is limited, more complex friction models are no doubt required to simulate these effects. New models must be developed to characterize these effects [44]. The work presented in this thesis however concerns only dry cutting, and lubrication is ignored.

In the context of FEA models of metal cutting many early models ignored friction altogether [70, 110] . In more recent years, four distinct friction models have been utilized for cutting simulations: coulomb friction, constant shear, constant shear in sticking and coulomb friction in sliding, and lastly a continuously varying coefficient of friction throughout the interface [70].

Type I: Coulombs Friction Model

Based simply on coulombs friction law, a linear relationship is defined between the normal pressure (σ) and the frictional shear (τ), here the proportionality constant is taken as the coefficient of friction (μ) as follows: .

$$\tau = \mu\sigma \quad (6-2)$$

This model has been described as over simplified [111, 112] and unable to accurately capture the sticking and sliding region at the tool tip. Most commonly the coefficient of friction for this model is estimated using Merchants cutting circle [70], from which a relationship for the coefficient of friction can be determined as a function of cutting force (F_c), thrust forces(F_t) and rake angle (α):

$$\mu = \frac{F_c \sin \alpha + F_t \cos \alpha}{F_c \cos \alpha - F_t \sin \alpha} \quad (6-3)$$

Alternatively, the coefficient of friction can be determined from pin on disc tribometric experiments [113]. In the absence of a pin on disc setup by running a lathe in

reverse and using the flank face of the tool in a plowing action a friction coefficient can be estimated [114].

Type II: Constant Shear Friction

A constant shear friction model assumes a constant shear stress (k) throughout the entire tool-chip interface. This shear stress is usually calculated as a fraction of the material flow stress [70]. Further this material flow stress can be estimated as:

$$k = \frac{F_c \cos \phi - F_t \sin^2 \phi}{2t_u w} \quad (6-4)$$
$$\phi = \tan^{-1} \frac{(t_u/t_c) \cos \alpha}{1 - (t_u/t_c) \sin \alpha}$$

where t_u , t_c and w are the uncut chip thickness, the chip thickness and the width of cut respectively.

A further shear friction factor still has to be estimated in order to scale this flow stress to a suitable level. Estimating this shear friction factor is not simple and usually one has to resort to shear limits established through split tool experiments from cutting tests.

Alternatively shear limits can be estimated from tribological experiments [113].

Type III: Constant Shear in Sticking Region and Coulomb Friction in Sliding Region

This mixed friction model aims to separate the friction models used in the sticking and sliding region in order to mimic Zorevs friction model. The difficulty here lies in

determining the point at which the transition occurs between the two models. In general, two separate approaches are taken where the length of the sticking region can be measured through experimental means [70, 71, 115]. This length is then used as a fixed input to the model. However during cutting simulation this distance is not constant and the experiments to measure this length are arduous, thus alternate approaches are often implemented. This usually entails changing between regimes at a fixed shear value, most often the same limit calculated in the constant shear model. No measurements of the sticking region length is needed. A common shear limit, a measure of the materials shear strength, based on Von Mises theory is calculated as:

$$\tau_m = \frac{\sigma_y}{\sqrt{3}} \quad (6-5)$$

where σ_y is the uniaxial tensile yield strength of the workpiece material [116]. One researcher used the shear flow stress as the limiting value [71].

$$\tau_m = \sigma_y \quad (6-6)$$

Type IV: Variable Coefficient of Friction through entire Tool-Chip Interface

There are a number of different approaches that can be taken under this particular heading, Usui et al [117] and Dirikolu et al. [118] worked out relations that describe the frictional behaviour as a function of various parameters that affect the tool-chip interface: most notably shear limit, normal pressure and some empirical coefficients. A more direct

method is to measure the relationship experimentally between normal pressure and shear stress from the results of cutting tests or pin on disc tests [113].

Orthogonal cutting experiments are compared to the predicted forces and residual stress profiles obtained using different friction models, in order to investigate the influence of these friction models on the predictions. The cutting parameters and material coefficients were held fixed while varying only the friction model. Using common techniques from literature, a total of 10 common friction conditions were identified, and a test matrix developed (see Table 6-I). The test matrix was run for each tool wear geometry. The effective model type, noted in Table 6-I, will be discussed later in the chapter.

Table 6-I: Test Matrix for Various Friction Conditions

#	Label	COF (μ)	Shear Limit (τ_m)	Effective Model Type	Tool Wear (μm)
1	$\mu=0.1$	0.1	None	Type I	71.5 and 175.5
2	$\mu=0.1 \tau_m=257$	0.1	257 MPa	Type I	71.5 and 175.5
3	$\mu=0.1 \tau_m=490$	0.1	490 MPa	Type I	71.5 and 175.5
4	$\mu=0.22$	0.22	None	Type I	71.5 and 175.5
5	$\mu=0.22 \tau_m=257$	0.22	257 MPa	Type II	71.5 and 175.5
6	$\mu=0.22 \tau_m=490$	0.22	490 MPa	Type I	71.5 and 175.5
7	$\mu=0.5$	0.5	None	Type I	71.5 and 175.5
8	$\mu=0.5 \tau_m=257$	0.5	257 MPa	Type III	71.5 and 175.5
9	$\mu=0.5 \tau_m=490$	0.5	490 MPa	Type I	71.5 and 175.5
10	$\mu=f(\sigma_n)$	$f(\sigma_n)$	None	Type 4	71.5 and 175.5

The experimental test matrix for the same work is shown below:

Table 6-II: Effect of Friction Model Test Matrix (AISI 1045 Cut Using an Uncoated WC Tool)

Test #	Feed	Speed	Rib Width	Rib Depth	Cutting Time	Tool Wear
1	200 $\mu\text{m}/\text{rev}$	200 m/min	3 mm	25 mm	3 Sec	71.5 μm
2	200 $\mu\text{m}/\text{rev}$	200 m/min	3 mm	25 mm	9 Sec	157.5 μm
3	200 $\mu\text{m}/\text{rev}$	200 m/min	3 mm	25 mm	12 Sec	175.5 μm

6.1.2 Modelling Parameters

The material in this work, AISI 1045, was cut using an uncoated cemented carbide tool. The workpiece was treated as an elastic-plastic body, whilst the tool was treated as

purely elastic. The thermo-mechanical properties used for this work are given in Table 5-I and Table 6-III. The thermal relaxation of the workpiece was treated exactly as outlined in Chapter 3 and 5, and since the feed per revolution, or uncut chip thickness, was kept quite large the sequential cut module was not necessary, this is schematically shown in Figure 5-2, where the uncut chip thickness is larger than the threshold to initiate the sequential cut module.

Table 6-III: Remaining Thermo-Mechanical Properties [105]

	Workpiece Material	Tool Material
Modulus of elasticity (GPa)	205	612
Poisson's ratio	0.3	0.22
Specific heat capacity (J/kg K)	470 @ 20 ⁰ C 535 @ 200 ⁰ C 635 @ 400 ⁰ C 800 @ 600 ⁰ C	334.01 + 0.12 θ
Thermal conductivity (W/m K)	46 @ 20 ⁰ C 40 @ 250 ⁰ C 34 @ 500 ⁰ C 27 @ 750 ⁰ C 25 @ 825 ⁰ C	86

6.1.3 Worn Tool Geometry

In order to accurately reflect the cutting conditions during the cutting experiment it was important to include not only the accurate cutting edge radius but also the actual tool wear. Only a short instant in time is simulated in the cutting model, while tool wear evolves in a timescale several orders of magnitude larger, a representative tool wear pattern was measured at two separate times for use in the model. The average geometry across the width of cut was approximated by a simple cutting geometry for quantification and use in cutting models. The angle of the flank wear land was best approximated by a

straight line at -10° from the horizontal, with the length of this segment increasing as tool wear progressed (V_b). Crater wear was treated as a shortening of the vertical section of the rake face (V_c). The work presented in this chapter is separated into two tool geometries: one for low flank wear ($V_b=71.5 \mu\text{m}$) and another one for comparatively high flank wear ($V_b=175.5 \mu\text{m}$) and limited crater wear. Measurements of the cutting edge geometry indicate that for the lower wear case ($71.5\mu\text{m}$) the cutting edge radius remains the same, with the flank wear restricting the arc length. For the case of the highly worn tool, the cutting edge radius evolves into a very small radius between the rake face and the wearland, as well as some bowing of the wear land. This was simplified by assuming a flat wear land for the tool. These geometries are shown in Figure 6-1 along with the original unworn cutting geometry. These values of tool wear were chosen to coincide with the measured values from experiments.

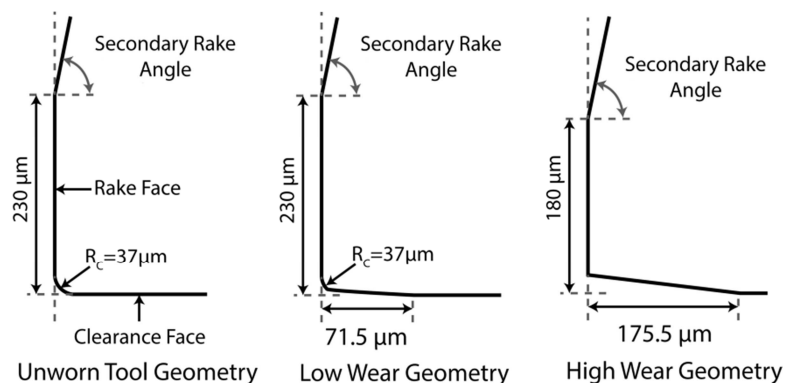


Figure 6-1: Worn Cutting Edge Geometry

6.2 Predicted Forces and Residual Stresses

Most cutting models are validated through comparison between experimental and predicted cutting force [45, 93, 119]. This is particularly the case for updated *Lagrangian*

simulations, which are not able to accurately predict thrust forces [103]. Figure 6-2 shows the predicted cutting forces for the the various friction conditions..

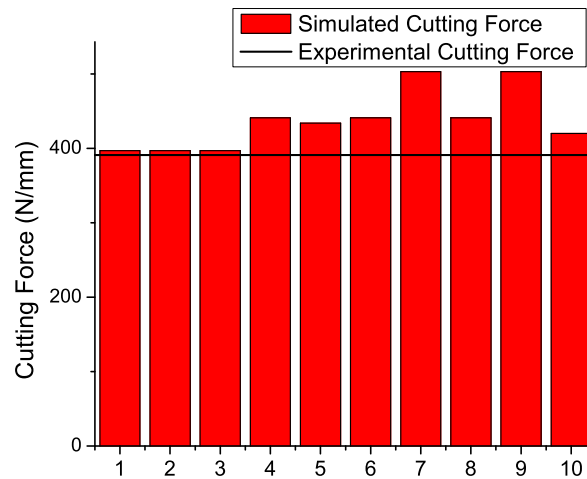


Figure 6-2: Comparison of Cutting Forces

Even though the case of $\mu=0.5$ somewhat over predicts the cutting force, when one considers the complexities of the cutting process it would appear that all of these friction models acceptably approximate the conditions within the tool-workpiece interface. As analysis of the influence of friction model on thrust forces is shown in Figure 6-3. There is clearly a large variation in thrust force from different friction models. The main observation here, if we consider only the cutting force, $\mu=0.1$ appears to be the best match to experimental results. However the thrust force for this case is substantially under estimated, but the cases with $\mu=0.22$ and $\mu=0.5$ with $\tau_m=257$ MPa do a good job of approximating both the cutting and thrust force.

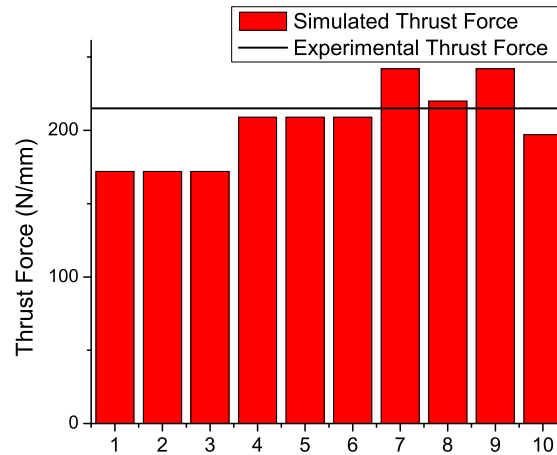


Figure 6-3: Comparison of Thrust Force

Considering the complexities of modelling the friction behaviours in orthogonal cutting, all of the predicted forces are not far from experimental cutting force. Minor changes in the material model could make any one of these match the force data quite precisely. If considering only force data for the validation of the cutting model any one of these friction models would apply, as noted in reference [71]. This changes significantly when we consider the more subtle measurement of residual stress profile beneath the machined surface. The predicted residual stress profiles for these friction models are shown in Figure 6-4 and Figure 6-6.

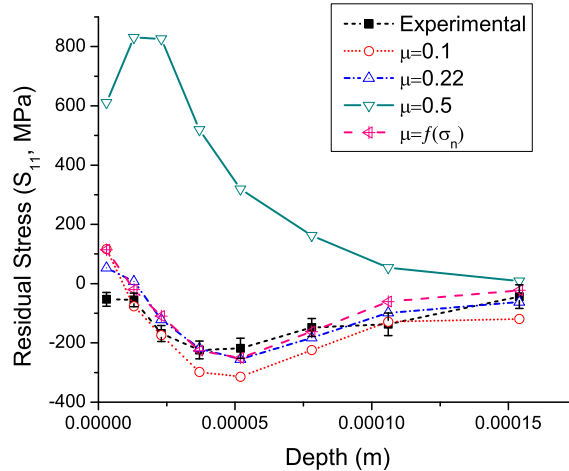


Figure 6-4: Effect of Coefficient of Friction on Residual Stress Profiles

From Figure 6-4, it appears that a coefficient of friction of $\mu=0.5$ results in an unreasonable residual stress profile in contrast to all other cases which provide acceptable results. At $\mu=0.5$ there is excessive heat generated and consequently temperatures increase drastically. This leads to a thermally dominated residual stress profile. This can be seen by comparing the decomposed residual stress profile for the $\mu=0.5$ and the $\mu=0.22$ case (see Figure 6-5), where the residual stress profile is decomposed into a mechanically induced component and a thermally induced component. By dividing the sum of the magnitude of both the mechanical and thermal contribution by the magnitude of the thermal contribution, the percentage contribution of thermal effects to the residual stress profile is estimated.

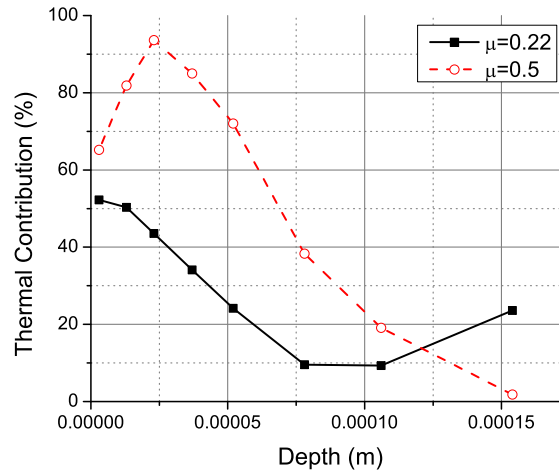


Figure 6-5: Thermal Contributions towards Total Residual Stress Profile

The change from a balanced RS profile at $\mu=0.22$ to a thermally dominated one at $\mu=0.5$ is apparent in their work. Anurag and Guo [72] found the thermal contribution towards the total residual stress profile to be around 20% which is in much better agreement with the lower friction cases. The effects of this overestimated friction condition can be mitigated through the use of a shear limit in the friction model as shown in Figure 6-6.

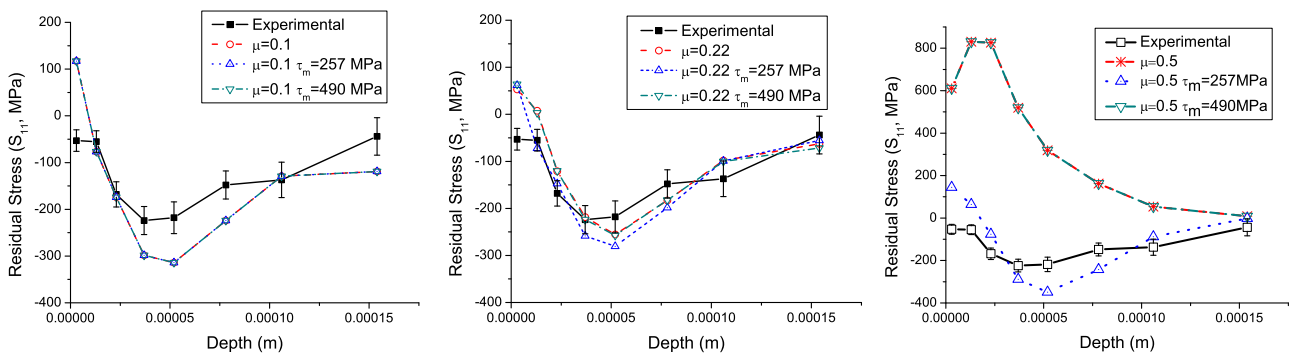


Figure 6-6: Effect of Shear Limit on Residual Stress Profiles

With more reasonable estimates of the coefficient of friction and shear limit, the changes in residual stress profile become more subtle. Most notable is that at lower

friction or shear limits the compressive residual stress component in the profile is increased without significant changes in the penetration depth. This result is not in agreement with the results reported by Anurag and Guo [72]. The difference can be explained by looking at the thermal contribution towards the residual stress profile, Anurag and Guo [72] reported about 20% thermal contribution to the final residual stress profile whilst the configuration in the present work results in a higher thermal contribution as seen in Figure 6-5. This probably correlates to much smaller uncut chip thicknesses in Anurag and Guo [72], than those used in this work, which would lead to a plowing dominated cutting process.

Further influence of shear limit was investigated by looking at the tool-chip interface. In Figure 6-7, the shear stress along the tool-chip interface is plotted. Starting at the end of the cutting edge radius along the flank of the tool the interface is traversed until past where the tool and chip separate on the rake face of the tool.

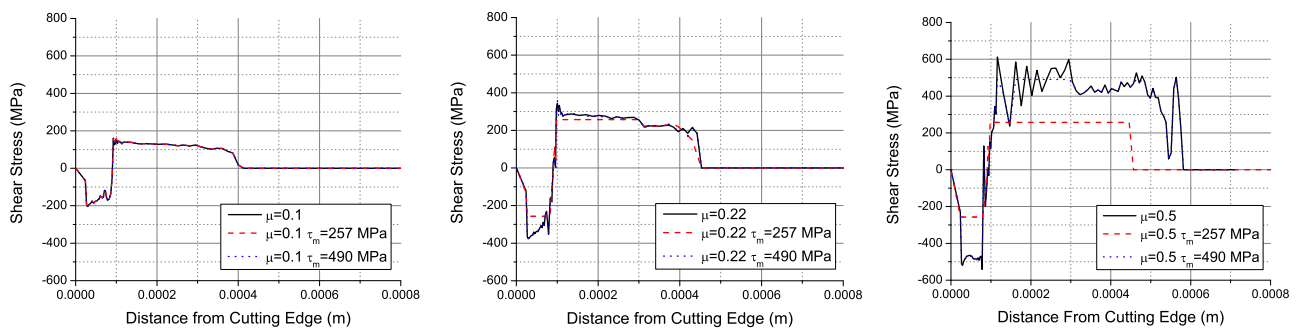


Figure 6-7: Shear Stress along the Tool-Chip Interface

The stagnation region can easily be identified by the change in the direction of shear stress; this is where the material flow changes from being pushed under the tool to flowing along the rake face of the tool. The point where the shear stress then falls and

remains at zero is where the tool-chip contact ends and is a measure of chip curl. In fact the influence of the COF on this curl is easily observed, with larger coefficients causing more gradual curl and smaller coefficients cause a sharp curl.

It is also interesting to observe that even without of any frictional shear, stress rarely exceeds 490 MPa. The most common methods for estimating the shear limit results in values of frictional shear equal to this, or even larger, depending on the exact approach. This is because the shear limit is estimated based on the material strength under pure shear. This level of stress is never exceeded in FEA because elements yield before this stress can be reached. In fact, the case of $\mu=0.5$ involves near perfect shear along the surface, as demonstrated by the mismatch in strain in different directions for a single element on the newly generated surface ($\epsilon_{11}=-1.33$ $\epsilon_{22}=1.27$ $\epsilon_{12}=-27.11$). Since there is always a normal stress as well as a shearing stress in cutting, the effective stress will always be greater than just the shear stress and the element will yield before the shear limit is reached.

When estimating friction coefficients from the friction angle in *Merchants* cutting diagram, values greater than 0.5 are obtained. It is likely that description of a single coefficient of friction is over simplified and inaccuracy arises from poor estimation of the friction condition. When an intentionally large COF is used, a shear limit is required in order to reduce the frictional shear and more accurately represent the chip shape. Even then, traditional estimates of shear strength are not sufficient. With the low shear limits required for large coefficients of friction, the entire tool-chip interface is controlled by the shear limit with coulombic friction affecting, at most, a couple of elements far away from

the primary, secondary or tertiary deformation zones. It is to be noted that when more accurate estimates of the COF are used these limits are not required. The use of a single well-tuned COF substantially reduces the tuning of the FEA model. For example, instead of tuning the friction to unreasonably large values in order to match cutting forces, the cutting geometry can be adjusted to more accurately resemble the cutting process. This brings the forces in better agreement without using unrealistic friction parameters.

Most existing literature on metal cutting simulation employs larger friction values and thus assumes low or negligible tool wear, or in other words, considers cases of perfectly sharp tools, or tool with a cutting edge radius free of any wear. However during the early stages of cutting, tool wear is very rapid until it stabilizes to a steady tool wear region and then accelerates when excessively worn. These changes in tool wear have a significant effect on cutting forces and temperature distributions, thus significant changes within the residual stress profile occur. In fact, as the tool wears, a larger tertiary shear deformation develops, allowing for significantly more interaction between the tool and workpiece. This increased interaction leads to a more appreciable influence of friction coefficient upon the predicted results. The cutting and thrust forces for various friction conditions are shown in Figure 6-8, for the same cutting conditions as in Table 6-I earlier, except that the tool wear is more significant ($V_b=175.5 \mu\text{m}$, $V_c=180 \mu\text{m}$).

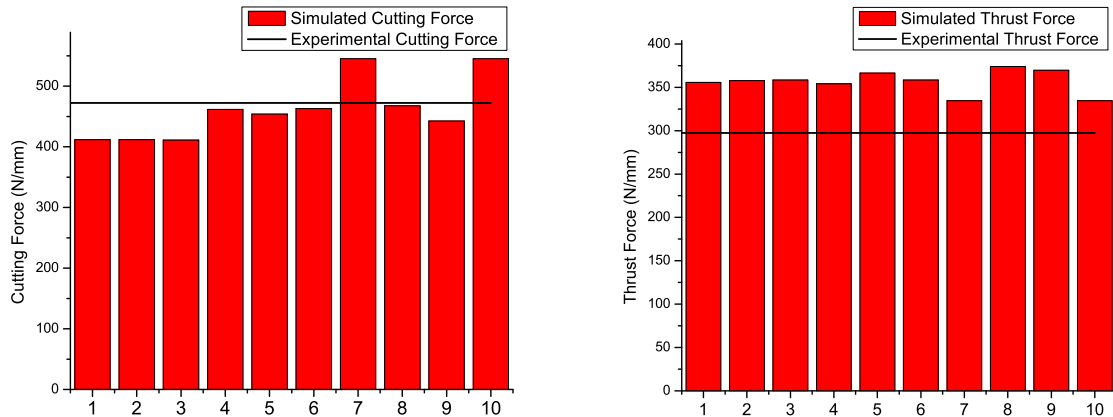


Figure 6-8: Cutting Forces and Thrust Forces for High Tool Wear ($V_b=175.5 \mu\text{m}$, $V_c=180 \mu\text{m}$)

With significant tool wear the sensitivity of the cutting model to friction condition changes substantially. The thrust force in all cases is significantly over predicted; this is a common problem when simulating thrust forces and is attributed to over simplification of the cutting region immediately ahead of the cutting edge. In the case of ALE the stagnation region can be captured, but fracture is not correctly modeled and consequently some inaccuracies result.

With low wear, the cutting force was well predicted for all cases except for $\mu=0.5$. However with larger tool wear this no longer holds, with substantial under prediction occurring at $\mu=0.1$. The opposite trend is observed for thrust force as a function of tool wear where the effect of friction becomes much less noticeable at higher tool wear. In fact as friction is increased the thrust force decreases, which differs with reported literature [71, 93]. This is, however, simply explained, as it is an effect of the direction in which the friction force acts along the flank wear. That is to say the flank wear, which was measured as described in the experimental section, is at an angle of -10° with the horizontal shown in Figure 6-1. Since the friction force acts tangential to this surface, the

friction force adds to the cutting force whilst also pulling the tool into the workpiece and reducing the thrust force. Thus increasing the coefficient of friction between a highly worn tool and the workpiece increases the cutting force and decreases the thrust force.

A second factor which acts to reduce the sensitivity of the more heavily worn model to friction in terms of thrust force is that the crater wear reduces the tool-chip contact length from 403 μm to 351 μm . Since the distance along which the friction force is acting almost parallel to the thrust force is smaller for the more highly worn case, the effect on the thrust force becomes less significant.

Despite the somewhat counterintuitive decrease in thrust force sensitivity with higher tool wear, friction is expected to have a significant effect on predicted residual stress profiles. This is largely due to the significantly increased temperatures experienced with high flank wear, causing thermal stresses to dominate the residual stress profile. Figure 6-9 shows the predicted residual stress profiles as compared to the experimental one for a significantly worn tool ($V_b=175.5 \mu\text{m}$, $V_c=180 \mu\text{m}$).

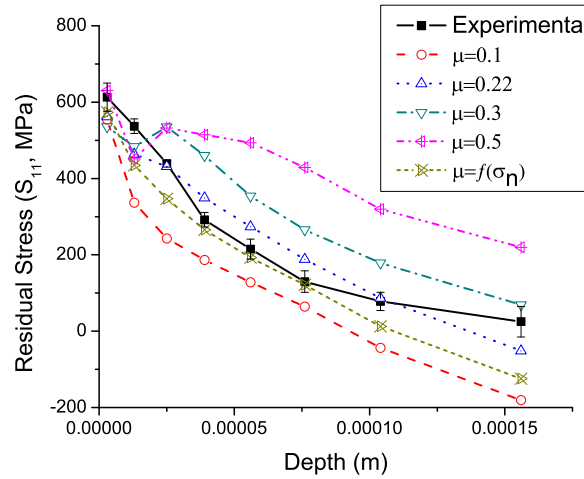


Figure 6-9: Residual Stress Profiles for Increasing Friction without a Shear Limit.

For the low tool wear case, the measured and predicted residual stress profile was of the typical sickle shape associated with cutting. However, for the high wear case the entire measured profile was tensile. This indicates, as expected, thermally induced residual stresses dominate the profile, and consequently these profiles are more sensitive to the effects of the coefficient of friction. This can be observed by looking at the difference in the contributions of mechanical as opposed to thermal effects on the total residual stress profile. This is shown in Figure 6-10 where the contribution for the case of $\mu=0.22$ is given for both the high and low tool wear.

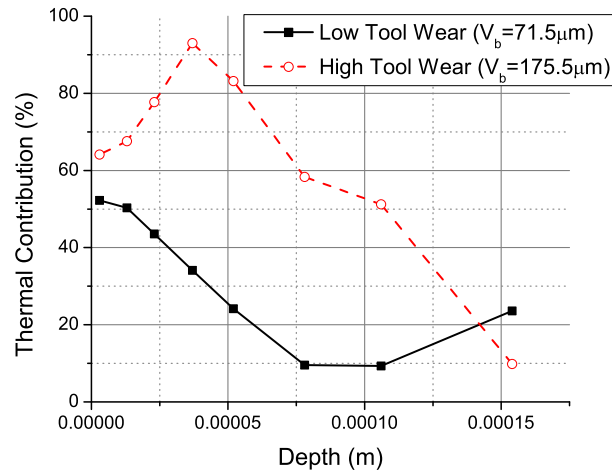


Figure 6-10: Mechanical and Thermal Contributions towards Total Residual Stress Profile ($\mu=0.22$)

As the coefficient of friction is increased from 0.1 all the way to 0.5, the temperatures increase drastically. The surface temperature of the workpiece as it leaves the tertiary deformation zone rises from 433°C with a coefficient of friction of 0.1 to 1006°C with a coefficient of friction of 0.5. These increased temperature gradients are evident in the increasingly tensile residual stress profiles achieved as a result of increasing the coefficient of friction.

As friction is increased a fluctuation in the residual stress profile is induced near the surface, this is where the dominating thermally induced stress are affected by the unreasonably large strains induced by sticking along the tool flank. The entire surface element shears instead of simply slipping along the surface, so high strains are experienced. The equivalent strain along the surface goes from 3.2 for $\mu=0.1$ to 4.0 for $\mu=0.22$ and up to almost 35 for $\mu=0.5$. This clearly unrealistic increase in strain leads to such strong gradients, that the existing mesh cannot resolve the problem, this results in a discontinuity in the predicted residual stress profile.

This unreasonable strain near the surface can be addressed by introducing a shear limit, and as in the low wear case, two separate shear limits are utilized: one at 490 MPa which is the initial yield point for this material under pure shear, and one at 257 MPa which is a more reasonable empirically derived shear limit. The residual stress profiles in response to these shear limits is shown below in Figure 6-11.

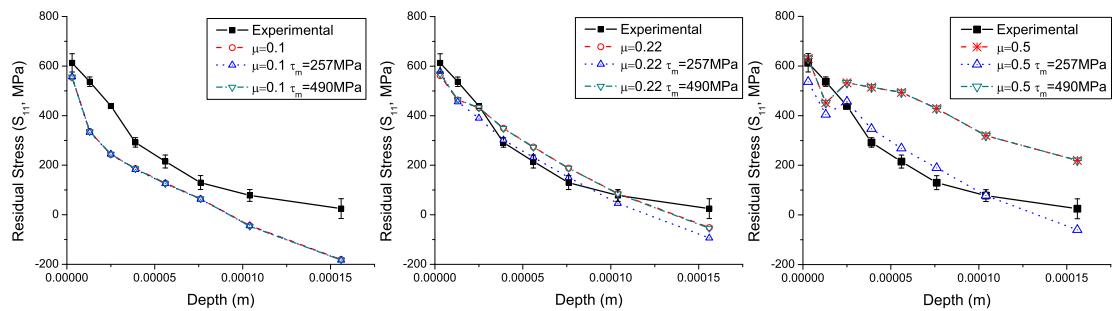


Figure 6-11: Effect of Shear Limit with Significant Tool Wear

As with the low tool wear case, the higher shear limit taken from the literature based on the shear strength of the material has no effect whatsoever, as the maximum shear at the tool-workpiece interface never goes above 490MPa.

The shear limit has any influence in the case of $\mu=0.1$ as this under predicted coefficient of friction fails to raise the shear stress near the limit. Even the case of $\mu=0.22$, which represents the measured coefficient of friction for this material pair, shows only limited effect of the shear limit. This suggests that if reliable experimental data is available for the coefficient of friction then a shear limit will only have limited effect and need not be used. This is for the already discussed reason that the material model within the FEA code is already equipped to handle the material yielding as a result of combined loading when sticking occurs.

However, as is evident from the case of $\mu=0.5$, if the coefficient of friction is significantly increased, the shear limit has a strong correcting influence. In this case the estimate of shear relative to normal stress is exaggerated, and the combined loading predicted by FEA is no longer accurate, thus the onset of yielding is not accurately captured. This becomes the same as a constant shear case at the magnitude of the shear limit. Thus, if there is some uncertainty with regard to the choice of coefficient of friction, a reasonable approach would be to choose a slightly higher coefficient of friction with a good empirically determined shear limit.

6.3 Summary

In general it seems that the choice of friction model matters less than the importance of choosing the correct values for the parameters of the friction model. In Table 6-I each of the tested models is characterized based on the observation of the interfacial shear into the different types of models. In the present work, a coulomb friction model ($\mu=0.22$), constant shear ($\tau_m=257\text{MPa}$), columbic in sliding and constant in sticking ($\mu=0.22$ and $\tau_m=257\text{MPa}$) as well as a pressure dependant function ($\mu=f(\sigma_n)$) (Types I through Type IV) were used to accurately predict both cutting forces as well as residual stress profiles. All these models can work, if accurate friction measurements are performed for the parameters required by these models.

It is worth noting that neither cutting nor thrust force are good at predicting which friction coefficient will most accurately predict residual stresses. Just because a cutting model can accurately predict the cutting and thrust force, does not mean that it is able to

predict residual stresses with any accuracy. Tuning the friction model in order to match force predictions to experimental measurements is a poor practice. Rather, the evolving cutting edge geometry needs to be accurately represented in order to improve force predictions. Friction should be based on realistic measured results from tribometric experiments.

Using simple cutting mechanics to estimate friction angles and thus finding a coefficient of friction for an FEA model results in very high estimates of the coefficient of friction ($\mu > 0.5$), which necessitates an accurate shear limit. Unfortunately simple mechanics estimate of the shear limit based on the yield strength of the material in pure shear yields large values ($\tau_m > 490\text{MPa}$). Thus using simple mechanics to avoid experimentally obtaining the friction behaviour for a tool-workpiece pairing is not reasonable.

The exact tool geometry including any tool wear is of the utmost importance in accurately predicting the cutting forces as well as residual stress profile. Unfortunately at present, the only accurate way of obtaining the cutting edge radius as well as the shape and size of any wear is purely experimental with work being pursued towards predicting the tool wear. A limitation of the present model is that the tool geometry must be known a priori. As long as it is necessary to perform a cut for some measurements, the model is not fully predictive. Unlike earlier models it is possible to use friction data from tribometric experiments rather than having to perform laborious split tool experiments to measure normal and frictional stresses along the cutting edge as in the case of [70]. Once reliable tool wear predictions can be made, it will be possible to determine all the process

and material parameters for a given material pairing without any cutting experiments, at which point models will be wholly predictive.

Finally, for the cases presented in this work, despite being able to make all the available types of friction models accurately predict the cutting forces and residual stress profiles, the recommendation is to use a simple coulumbic coefficient of friction as it is the most simple of the models available and thus requires minimum experimental work to obtain its parameters.

Chapter 7: Phase Transformations in Residual Stress Prediction

There is no doubt that a significant source of residual stresses in many machined parts arise from phase transformation induced effects. As such this chapter concerns itself with extending the framework of the basic ALE cutting model to be able to predict the phase changes that occur near the surface of many machined parts. This chapter presents the details of a phase transformation module, and the results obtained from this module are compared with the experimentally obtained results. As with the previous two chapters the parameters of the base ALE cutting model used are discussed first then the new phase transformation module is discussed. This is followed by the obtained results.

7.1 Model Details

7.1.1 Modelling Parameters

The material in this work, AISI 4140, was cut using an uncoated cemented carbide tool. As earlier, the workpiece was treated as an elastic-plastic body, whilst the tool was treated as purely elastic. The thermo-mechanical properties used for this work are given in Table 7-I and Table 7-II. The thermal relaxation of the workpiece was treated exactly as outlined in Chapter 3, and since the feed per revolution, or uncut chip thickness, was quite large the sequential cut module was not necessary.

Table 7-I: Plastic Properties and the Workpiece [120]

A (MPa)	B (MPa)	n	C	$\dot{\epsilon}_0$ (s^{-1})	θ_m ($^{\circ}C$)	m
598	768	0.2092	0.0137	1	1520	0.807

Table 7-II: Remaining Thermo-Mechanical Properties

	Workpiece Material [120]	Tool Material [105]
Modulus of elasticity (GPa)	210 GPa	612
Poisson's ratio	0.3	0.22
Specific heat capacity (J/kg K)	473 @ 200 $^{\circ}C$ 519 @ 400 $^{\circ}C$ 561 @ 600 $^{\circ}C$	334.01 + 0.12 θ
Thermal conductivity (W/m K)	42.6 @ 100 $^{\circ}C$ 42.3 @ 200 $^{\circ}C$ 37.7 @ 400 $^{\circ}C$ 33.0 @ 600 $^{\circ}C$	86

7.1.2 Worn Tool Geometry

In order to accurately reflect the cutting conditions during the cutting experiments, it was important to include not only the precise cutting edge radius but also the actual tool wear. The average geometry across the width of cut was approximated by a simple cutting geometry for quantification and use in cutting models. The angle of the flank wearland was best approximated by a straight line at -1° from the horizontal, with the length of this segment increasing as tool wear progressed (V_b). Crater wear was not an issue with this material pairing.

The work presented in this chapter is separated into three tool geometries corresponding to low flank wear ($V_b=88 \mu m$), medium flank wear ($V_b=267 \mu m$), and

comparatively high flank wear ($V_b=332 \mu\text{m}$). These geometries are shown in Figure 7-1 along with the unworn cutting geometry.

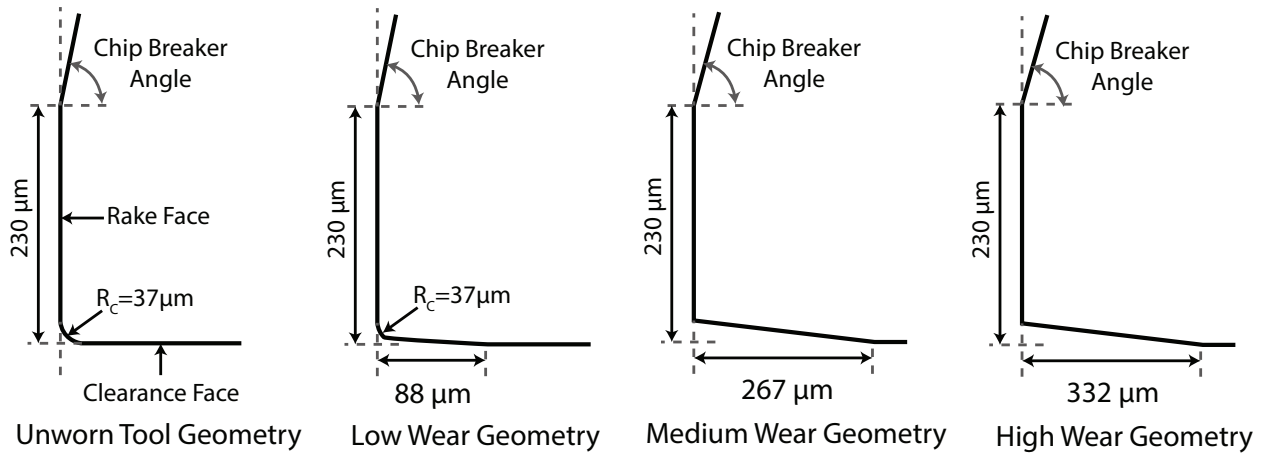


Figure 7-1: Cutting Edge Geometry

7.2 Friction at the Tool-Chip Interface

Previous work on the effect of friction on the formation of residual stresses steered the choice of friction models for this material pairing to a simple coulumbic coefficient of friction with a shear limit to help limit the excessive strain induced by sticking of the nodes along the tool-chip interface. The friction parameters used in this work were $\mu=0.22$ and $\tau_{\max}=205 \text{ MPa}$.

7.3 Phase Transformation Module

Due to the short time scales involved with the heating and cooling during the cutting process, austenitic and diffusion reactions are limited [121, 122]. The base material transforms into austenite without reaching the equilibrium weight fraction of austenite. The volume fraction of austenite formed during the cutting process for a given

element thus needs to be determined. Miokovic [121] presents a comprehensive methodology for predicting austenite and martensite formation within AISI 4140.

The methodology entails applying *Sheil's* additivity rule to empirically determined constant heating curves in the form of *Avrami* functions. In this context the *Avrami* function for continuous heating or cooling is expressed by Equation (7-1):

$$f_A = 1 - \exp[-(bt)^n] \quad (7-1)$$

where t is time and n is an experimentally determined parameter. The parameter b is defined by Equation (7-2):

$$b(T) = C \exp\left[-\frac{\Delta H}{kT}\right] \quad (7-2)$$

Where ΔH is the activation enthalpy for the ferrite to austenite transformation, C is a velocity constant, k the Boltzmann constant and T the temperature in K. If the parameters b and n are known for a material then the *Avrami* function can fully describe the isothermal formation of austenite. *Sheil's* additivity principle enables an arbitrary temperature history to be discretized into a series of short isothermal time steps, during which the formation of austenite is governed by the empirically determined *Avrami* function. Thus the volume fraction of austenite after time t_{i+1} can be calculated by applying Equation (7-3):

$$f_{A,i+1} = f_{A,i} + \Delta f_A = f_{A,i} + \left. \frac{\partial f_{A,i}}{\partial t} \right|_{t_i^*} \Delta t \quad (7-3)$$

where $\left. \frac{\partial f_{A,i}}{\partial t} \right|_{t_i^*}$ is defined by Equation (7-4)

$$\left. \frac{\partial f_{A,i}}{\partial t} \right|_{t_i^*} = n * b(T_i) \ln \left(\frac{1}{1 - f_{A,i}} \right)^{\frac{n-1}{n}} (1 - f_{A,i}) \quad (7-4)$$

As the workpiece begins to cool the austenite will begin to transform to either bainite or martensite. In order to determine which of the two will form, the integral in Equation (7-5) needs to be evaluated [123]:

$$\int_0^t \frac{dt}{t_\alpha(T)} \geq 1 \quad (7-5)$$

where dt is the timestep and $t_\alpha(T)$ is the incubation time required, at temperature T , for bainite to form, and t is the cooling time. If this integral exceeds 1 before the temperature drops below the martensite formation temperature, bainite will form. However in this work, the timescales are much smaller than those required to satisfy this integral and as such only martensite is formed.

Transformation of austenite to martensite was addressed by the Koistinen-Marburger relation [55] as shown in Equation (7-6):

$$f_m = f_m^{max} (1 - \exp(-\gamma(M_s - T))) \quad (7-6)$$

where γ is a constant usually found to be close to 0.011 for most steels, including AISI 4140, M_s is the temperature when the martensite transformation begins. T is the temperature of the region of the workpiece where the phase transformation occurs, and f_m^{max} the maximum amount of martensite that can be formed, in this case the total amount of austenite.

These phase transformations are coupled with the stress field by introducing an additional strain component to the total strain. Thus the volumetric change associated with the various phase changes can be incorporated into the relaxation model, where the strain increment due to this volume dilation is shown by Equation (7-7) [124, 125] :

$$\Delta\varepsilon^{\Delta V} = \frac{1}{3} \frac{\Delta V}{V} \Delta f \quad (7-7)$$

The percentage change in volume due to phase transformation ($\Delta V/V$) for each of the transformations is given with the material properties in [15], and Δf is the change in volume fraction of the phase during the time increment. The volumetric dilation used in this simulation was a combination of that yielded from the annealed AISI 4140 to austenite as well as that from austenite to martensite. As long as this strain combined with the thermal relaxation is elastic, the transformations can be coupled to the stress field using the isotropic *Hook's* law with temperature dependant *Young's* modulus.

This model calibrated with the parameters determined by Miokovic et al. [121] has been implemented in MATLAB which draws upon the temperature history developed within the thermal relaxation module. Schematically this process is illustrated in Figure 7-2.

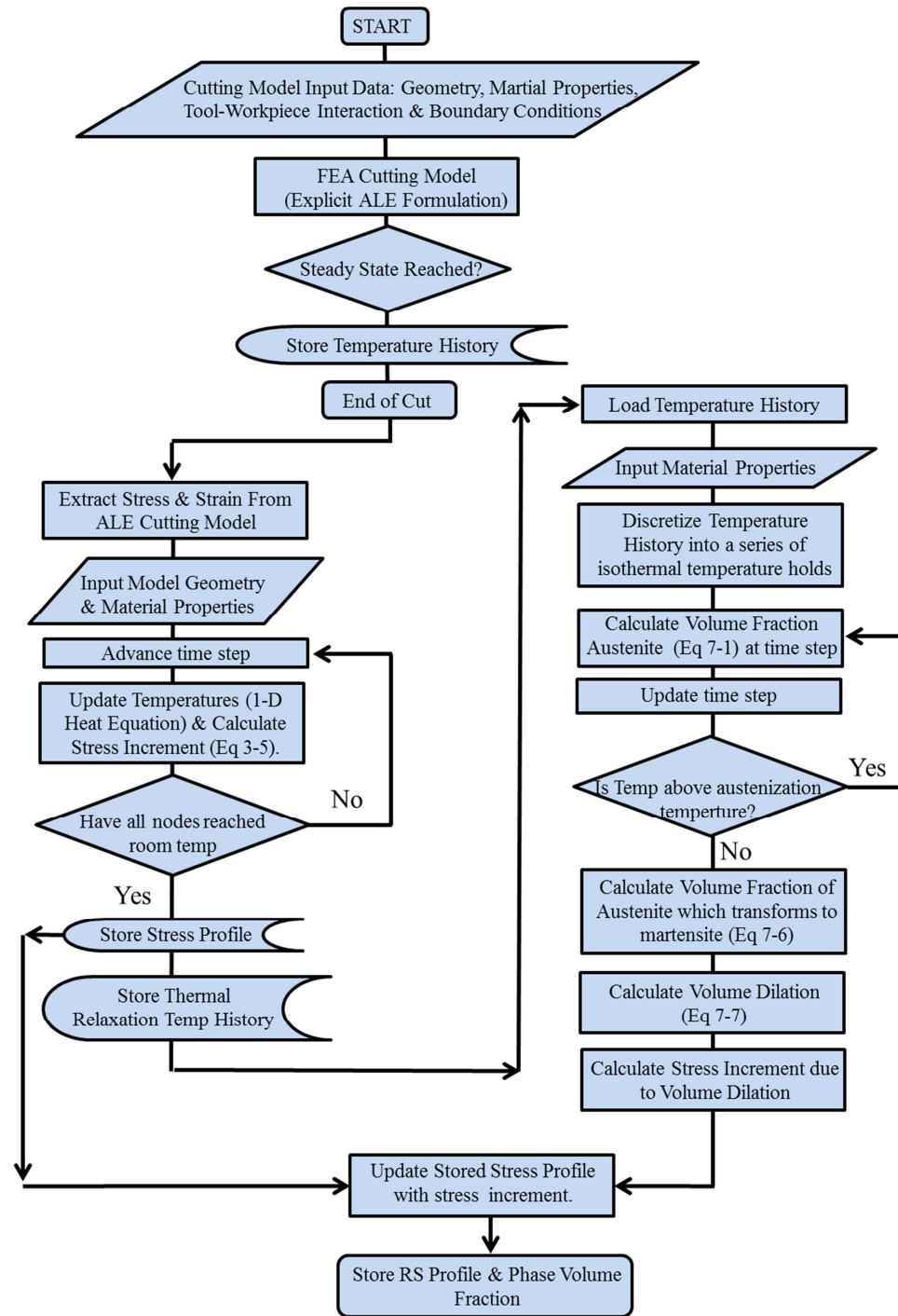


Figure 7-2: Flow Chart of Phase Transformation Prediction Module

The experimental test matrix used for this work is given below:

Table 7-III: Effect of Phase Transformations Test Matrix (AISI 4140 Cut Using an Uncoated WC Tool)

Test #	Feed	Speed	Rib Width	Rib Depth	Cutting Time	Tool Wear
1	200 $\mu\text{m}/\text{rev}$	300 m/min	3 mm	25 mm	3 Sec	88 μm
2	200 $\mu\text{m}/\text{rev}$	300 m/min	3 mm	25 mm	9 Sec	267 μm
3	200 $\mu\text{m}/\text{rev}$	300 m/min	3 mm	25 mm	12 Sec	332 μm
4	200 $\mu\text{m}/\text{rev}$	150 m/min	3 mm	25 mm	3 Sec	76 μm

7.4 Predicting White Layer Depth

In order to perform a basic assessment of the cutting model, cutting and thrust forces were measured during cutting experiments. The cutting process was stopped after varying distances cut and the tool wear was measured, and cutting models were run for these tool wear profiles. From this model cutting and thrust forces were extracted, and then compared to the measured ones with a single standard deviation given as the error bars (see Figure 7-3).

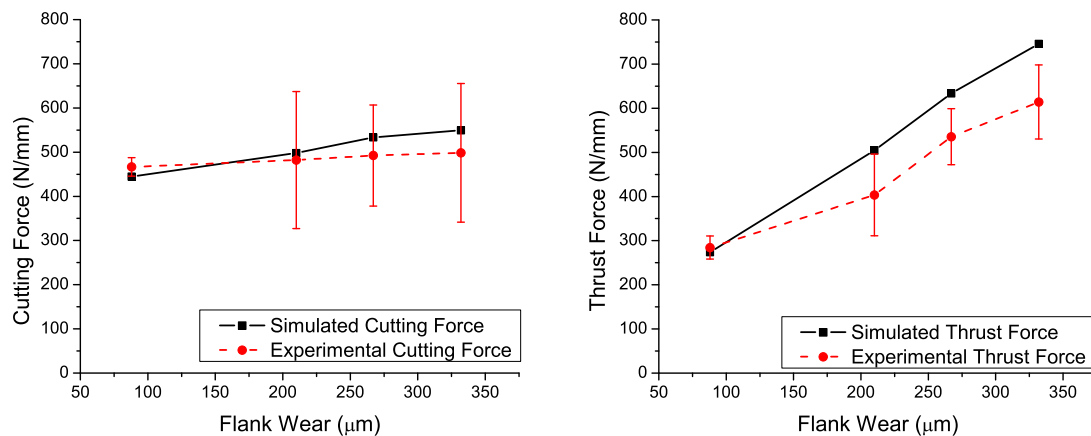


Figure 7-3: Cutting and Thrust Forces

As would be expected both the cutting and thrust forces increase with tool wear, however the thrust force is much more significantly affected, as this triples over the measured region. The importance of accurately representing the worn cutting geometry is apparent in the sensitivity of the thrust force to tool wear. Further the cutting force is quite accurately captured, with some over prediction apparent in the thrust force. In terms of a quick analysis of the cutting model it can be concluded that the forces are well predicted and the cutting model can be used for the prediction of white layer.

The stress and temperature history from the model was output for a narrow segment of the newly formed surface, and introduced into the thermal relaxation and phase transformation modules to obtain the volume fraction of martensite. For the three worn tool geometries shown in Figure 7-1, the volume fraction of martensite is shown in Figure 7-4.

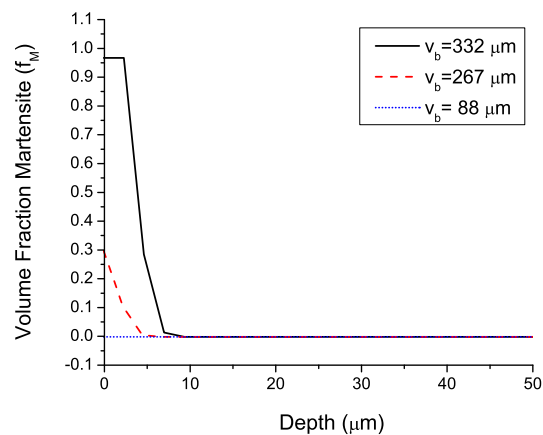


Figure 7-4: Volume Fraction Martensite Predicted as a Function of Tool Wear.

The three different wear sizes correspond to the three possibilities in terms of white layer, the lowest wear case of 88 μm results in insufficient temperatures for any austenization to occur thus no martensite is predicted and no white layer is formed. The

increased temperatures associated with 267 μm of wear allow for partial austenization of the workpiece near the surface. Since the temperatures and time scales are small enough, the predicted volume fraction of martensite is quite small, so still no white layer is formed. Finally temperatures increase again as the wear increases to 332 μm allowing for substantially more austenization. In fact a thin layer of 3 μm at the surface fully austenizes resulting in almost pure martensite near the workpiece surface with volume fraction of martensite dropping very rapidly at increased depths. By 7 μm beneath the surface the fraction of martensite drops down to zero.

The experimentally obtained workpiece was sectioned as described in Chapter 4, mounted, polished and etched. Under an optical microscope the white layer thickness, if any, was measured. Two sample micrographs are shown below in Figure 7-5 with the sample cut at moderate tool wear (267 μm flank wear) shown on the left and the one cut with high wear (332 μm flank wear) on the right.

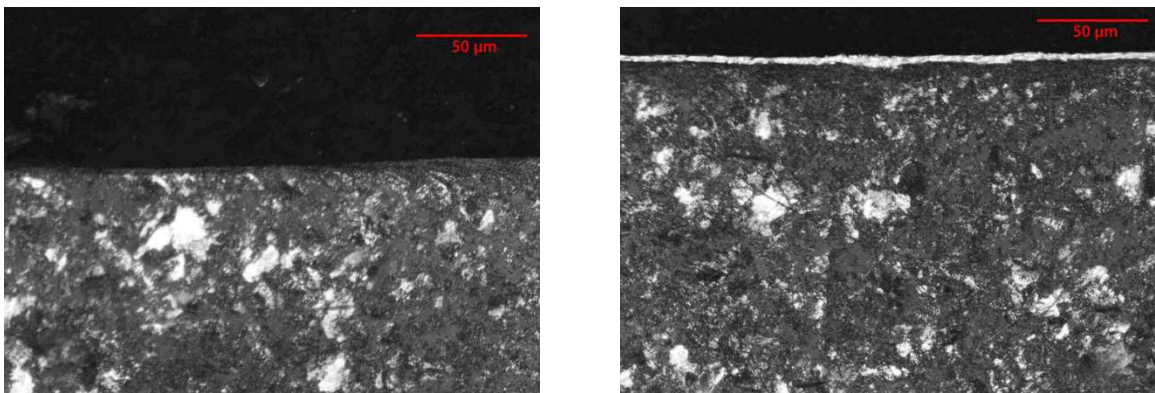


Figure 7-5: Micrographs Cut with 267 μm Flank Wear on Left and at 332 μm Flank Wear on the Right.

As expected the samples cut with 88 μm and 267 μm of wear showed no evidence of a white layer, which is in agreement with the simulation. At 332 μm of flank wear

there was an average white layer thickness of $4.6 \mu\text{m}$ with a standard deviation of $0.78 \mu\text{m}$. The maximum measured thickness was $6.8 \mu\text{m}$ and the minimum was $3.3 \mu\text{m}$. The average white layer thickness is shown in Figure 7-6 as the gray shaded region with the predicted martensite content superimposed.

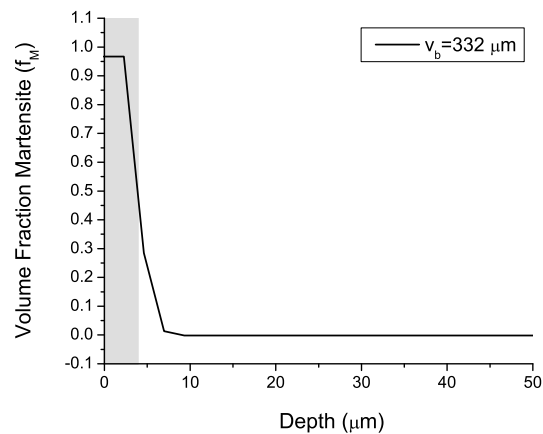


Figure 7-6: Volume Fraction Martensite Predicted as a Function of Tool Wear, Average Whitelayer Thickness for $v_b = 332$ is Indicated as the Shaded Region.

It is clear that the predicted white layer thickness is in good agreement with the measured thickness, which falls between the fully austenized layer and the untransformed layer. Since the model is capable of accurately predicting the white layer thickness, the next challenge is to see the influence of coupling the volumetric changes during phase transformations to the residual stress profile.

7.5 Modelling of Residual Stresses

In order to assess the efficacy of the residual stress module, experimental measurements of the residual stress depth profile were carried out. The measured residual stress profiles for each of these geometries is given in Figure 7-7 with one standard deviation shown as error bars.

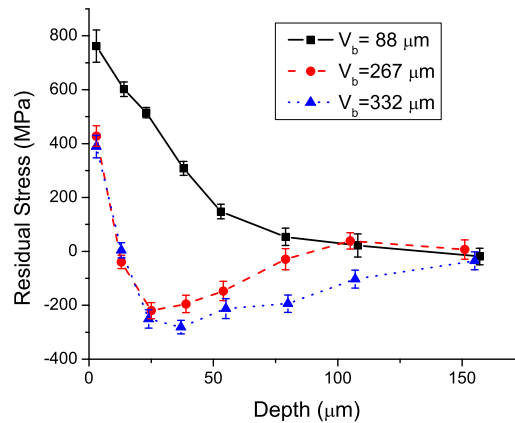


Figure 7-7: Experimentally Measured Residual Stress Profiles

The trend given by this experimentally measured profile is somewhat unexpected, given that increasing tool wear leads to increasingly tensile residual stresses [15]. The general shape of the residual stress profiles is more in agreement with those measured by Salvatore et al. [54]. However penetration depths measured in this work were significantly smaller. Given that the heat treatment of the workpiece was not mentioned, it is possible that it was hardened, which would account for the difference in measured profiles.

Since the martensitic phase transformation tends to induce compressive residual stresses, it is tempting to assign this increasingly compressive residual stress profile to increasing volume fractions of martensite. However from the previous section it is known that the phase transformations do not penetrate below 10 μm. Thus, this trend must be attributed to other processes. This increasingly tensile trend is most likely due to strain hardening increasing the mechanical work, as seen in Figure 7-3 and leading to increased mechanical contributions to the final residual stress profile, despite increasing temperatures. This exact same trend can be observed in the simulated results in Figure 7-8

where flank wear increases from left to right from 88 μm to 267 μm and 332 μm respectively.

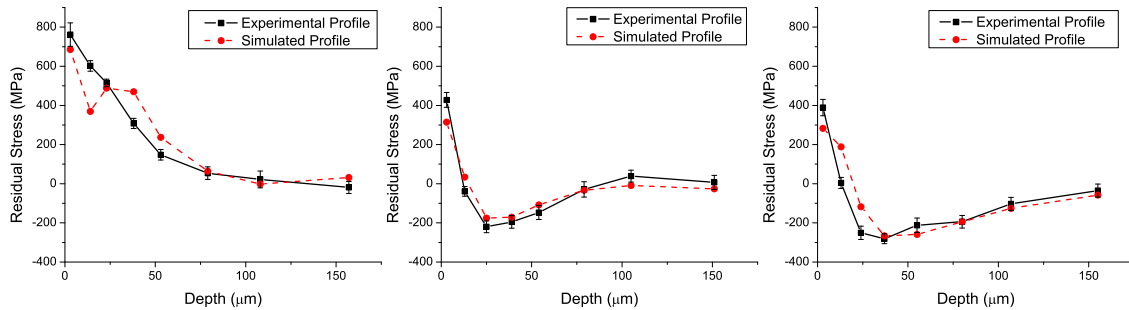


Figure 7-8: Experimental and Simulated Residual Stress Profiles for $v_b = 88 \mu\text{m}$, 267 μm and 332 μm Respectively from Left to Right.

From this we see that the model is indeed able to capture the residual stress profile to a high degree of accuracy. This is true in cases where there is a very limited amount of phase transformation, as well as when there is a noticeable white layer on the finished workpiece. Further by looking at the residual stress profile predicted without the phase transformation module as well as that using phase transformations, one can get an idea of the influence of the phase transformations on the profile. In Figure 7-9, the two profiles are shown along with the inferred effect of the transformation.

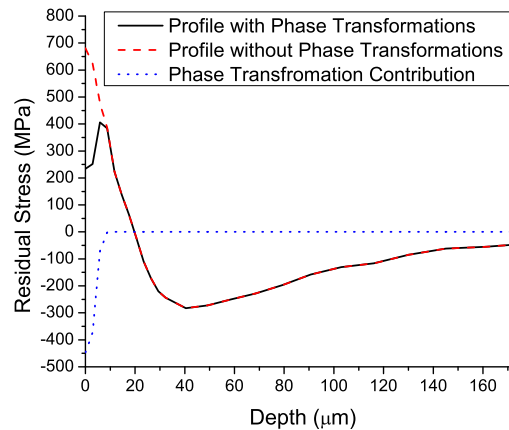


Figure 7-9: Effect of Phase Transformation Module

These results indicate that there is only a small change in profile gained by incorporating the phase transformations. However, it is worth noting that the surface tensile stress is reduced almost by a third and the maximum tensile residual stress is reduced by almost half from phase transformations. Since there is a direct link between the maximum tensile stress and surface residual stress and final part fatigue life [81] this represents a significant change in predicted part quality. However, this might be moot since the integrity of the white layer is typically poor and the pre-existing micro cracks reduce part life [80].

It is to be noted that despite the significant shift of the surface residual stress profile, phase transformations are not sufficient to explain the increasingly compressive stress profiles achieved with increasingly worn tools. So as suggested above it is necessary to look at the mechanical and thermal contributions towards the final residual stress profiles. In Figure 7-10 these contributions are shown for each of the geometries, where the thermal contribution is the effect of thermal relaxation on the residual stress

profile, the phase transformation contribution is that due to volume dilation during phase change, the balance is due to mechanical processes.

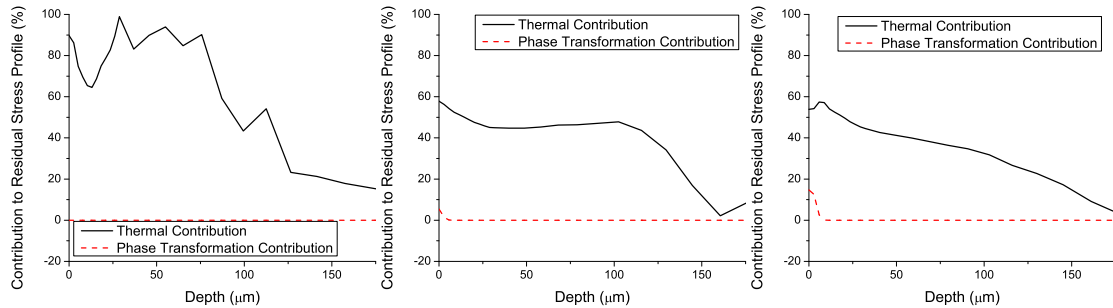


Figure 7-10: Component Contribution towards Total Residual Stress Profile, for $v_b = 88 \mu\text{m}$, $267 \mu\text{m}$ and $332 \mu\text{m}$ respectively from left to right.

These plots show clearly that in the area where the increasingly compressive trend is strongest ($<75 \mu\text{m}$ depth), despite increasing temperatures with wear, the thermal contribution reduces dramatically with increased tool wear. For $88 \mu\text{m}$ flank wear the majority of the residual stress profile is contributed by thermal processes. However, as tool wear rises, increasing loads offset the mounting temperature resulting in much lower thermal contributions. These results differ from the work of Xie et al. [15] who found purely tensile residual stresses despite cutting AISI4140 at significantly slower speeds. The difference is most likely due to their use of very small uncut chip thicknesses ($<1/10$ of the values in this work). It is likely that cutting was performed at very near the minimum uncut chip thickness, in which case rubbing becomes severe and excessive cutting temperatures are to be expected, especially with worn tools.

Despite the strong agreement between the experimentally measured residual stress profiles and those predicted using this approach, it is important to note that there are some

limitations of this model in regards to predicting white layer formation. This model is only able to predict thermally induced phase transformations, but white layer can be formed through severe plastic deformations (SPD) as well [52]. In general this occurs for high part hardness and fast cutting speed, as illustrated for AISI 52100 bearing steel in Figure 7-11. This is for a different workpiece material, yet the trend should be similar for AISI4140.

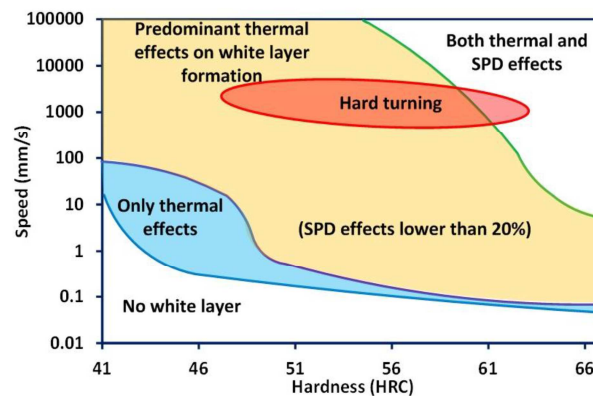


Figure 7-11: Nature of White Layer Formed at Various Speeds and Workpiece Metallurgical States. (Adapted from [52]).

This all means that the current model will only work for relatively soft materials (HRC<50) or low cutting speeds. There is however a further limitation of ALE cutting model as it is not able to predict the adiabatic shearing which occurs when segmented and saw-tooth chips are formed. These types of chips are characteristic of the high speed high hardness cutting conditions where SPD become significant, so before the model can really be expanded to consider these changes, it is necessary to expand the model to include discontinuous or at least saw-tooth chips.

Chapter 8:

Conclusions

This chapter begins with a summary of the main conclusions drawn through the work presented within this thesis. Subsequently the next steps of this research are discussed with recommendations for future work.

8.1 Summary of Results

As with the rest of this thesis, the results can be separated into three distinct sections, small uncut chip thickness, frictional effects and phase transformations. The main conclusions for each section are summarized below.

8.1.1 Small Uncut Chip Thickness (Sequential Cut)

Since the time scale of the thermal relaxation after metal cutting is significantly longer than the time scale of the actual cutting time, significant time savings were achieved by developing a relaxation module to relax the stress field outside of the main ALE model. To this effect a simple elastic relaxation subroutine with a sequential cut module was written in MATLAB.

When simulating small feed rates without the sequential cut module, substantial differences were observed between the experimentally obtained residual stress profiles and those predicted by FEA. In many instances the model completely missed the compressive portion of the residual stress profile. However using sequential cuts, a drastic

improvement in the prediction of residual stress profiles was achieved; in fact the experimental and profiles simulated using the sequential cut module were nearly identical.

As feed rates were increased, the benefits of sequential cuts became less noticeable, as a single pass simulation actually manages to predict the residual stress profile with good accuracy. In fact for feed rates in excess of $100\mu\text{m}/\text{rev}$ the limited improvement does not merit the increased simulation time required for the sequential cut module.

Further it was determined that if the remaining stress state in the finished surface is not the main goal of the simulation, then even with small uncut chip thicknesses the benefits of the sequential cut module are limited. That is because the chip morphology and tool-workpiece interface are not significantly different between passes.

8.1.2 Frictional Effects

A significant study on the effect of friction on the residual stress profile formed during dry orthogonal cutting was presented for both lightly worn as well as highly worn tools. It was shown that lightly worn tools are only minimally affected by the choice of friction model, whilst more significantly worn tools are affected to a larger degree by the friction model. Tool wear is normally neglected when simulating residual stress profiles, which might account for the disagreement within the literature on the significance of the friction model.

It was further shown that good results can be obtained using a number of different friction models, independent of the amount of tool wear. In general a realistic

determination of the parameters for a friction model far outweighs the choice of model, thus the most simple one should be used where possible. In general this means that shear limit (τ_m) is not needed for a well characterized coefficient of friction (μ). However if a shear limit is used, it is important to note that the limit is not the same as the shear limit of the workpiece material under pure shear, or the flow stress of the workpiece material. The shear limit should be carefully determined through tribometric experiments.

Analytical solutions typically used to estimate the coefficient of friction for metal cutting yield unrealistically large coefficients of friction. Accurate prediction of cutting forces with such large values of coefficient of friction does not mean that the residual stress profile, temperatures or even chip thickness are accurately predicted. In fact, the common practice of calibrating a friction model using cutting forces seems to have little merit, as there is little correlation between the accuracy of the force prediction and the accuracy of the predicted residual stress profiles. A better approach is to use a simple friction model, and to modify the cutting geometry to more accurately represent the actual cutting conditions to calibrate the cutting forces.

8.1.3 Phase Change

In this work an FE model was developed for studying both the onset of white layer as well as residual stresses during cutting. This model was calibrated and validated for AISI 4140 using a number of differently worn tool geometries. The strong agreement between the predicted residual stress profiles and experimental ones, in addition to accurate white layer depth predictions, indicate that the model can indeed be used to study the relationship between various cutting parameters and the finished sub surface quality.

Further the developed models were used to show that the increasingly compressive residual stress profiles measured during this work were due to increased mechanical loading, despite increasing temperatures with tool wear. It was shown that by including phase transformations into the residual stress prediction, the surface residual stress is strongly affected and agrees better with measured profiles. Some limitations to this model were also discussed which point to future work, developing a reliable ALE cutting model that can handle segmented and saw tooth chips to simulate harder materials where phase transformations become even more significant.

8.2 Future Work

Throughout this work a consistent limitation faced was the present inability of the ALE cutting model to predict segmented chips. Much of the field where residual stresses are of particular interest is in hard aerospace materials which typically cut in a segmented manner. A modification to the ALE model to include a damage criterion near the chips free surface, which would allow segmented chips to be modeled, would be of great interest to the field, and would, in principle, lead to the development of a new meshing scheme.

A further development which would significantly add to the versatility of the ALE cutting model would be the incorporation of microstructure into the model. This could be achieved through a user material model which would allow the entire workpiece to be modeled as one material having spatially distributed properties. This would overcome the

inherent difficulties of the ALE model in regards to different materials and would add significantly to the state of the art.

Currently the ALE cutting model is not fully predictive since tool wear measurements are needed to accurately represent the conditions at the tool-workpiece interface. A continuously evolving tool profile based on wear rate predictions would obviate the necessity for tool wear measurements and would significantly advance the predictive abilities of the cutting models.

Lastly, at present the ALE model struggles to take advantage of multiple processors because ABAQUS has problems dividing an ALE region between multiple processors. Using clever partitioning it might be possible to allow for a better segmentation scheme. Significant computational advantage would be realized as computers continue to have more parallel processors.

References

- [1] E. Brinksmeier, J. Cammett, W. Koenig, P. Leskovar, P. Peters and H. Toenshoff, "Residual Stresses - Measurement and Causes in Machining Processes," *Ann. CIRP*, vol. 31, no. 2, pp. 491-510, 1982.
- [2] H. Kishawy and M. Elbestawi, "Tool Wear and Surface Integrity During High-Speed Turning of Hardened Steel with Polycrystalline Boron Nitride (PCBN) Tools," *Proceedings of the IMechE part B, J. of Engineering Manufacture*, vol. 125, no. 6, pp. 755-767, 2001.
- [3] T. Kawakamia and T. Kuniedaa, "Study on Factors Determining Limits of Minimum Machinable Size in Micro EDM," *Ann. CIRP*, vol. 54, no. 1, pp. 167-170, 2005.
- [4] E. Capello, P. Vavoli, G. Bassanini and A. Bisi, "Residual Stress and Surface Roughness in Turning," *Trans. of the ASME, J. of Engineering Materials and Technology*, vol. 121, no. 3, pp. 346-351, 1999.
- [5] R. Stephens, A. Fatemi, R. Stephens and H. Fuchs, *Metal Fatigue in Engineering*, 2 ed., New York: John Wiley and Sons Inc., 2001.
- [6] G. Webster and A. Ezeilo, "Residual Stress Distributions and Their Influence on Fatigue Life," *Int. J. of Fatigue*, vol. 23, no. 1, pp. 375-383, 2001.
- [7] M. Field and W. Koster, "Optimizing Grinding Parameters to Combine High Productivity with High Surface Integrity," *Ann. CIRP*, vol. 27, no. 1, pp. 523-526, 1978.
- [8] C. Liu and X. Yang, "The Scatter of Surface Residual Stresses Produced by Face-Turning and Grinding," *Machining Science and Technology*, vol. 5, no. 1, pp. 1-21, 2001.
- [9] D. Jang, T. Watkins, K. Kozaczek, C. Hubbard and O. Calvin, "Surface Residual Stresses in Machined Austenitic Stainless Steel," *Wear*, vol. 194, no. 1, pp. 168-173, 1996.
- [10] J. Outeiro, A. Dias and I. Jawahir, "On the Effects of Residual Stresses Induced by Coated and Uncoated Cutting Tools with Finite Edge Radii in Turning Operations," *Ann. CIRP*, vol. 55, no. 1, pp. 111-116, 2006.
- [11] J. Thiele, S. Melkote, R.A. Peascoe and T. Watkins, "Effect of Cutting Edge Geometry and Workpiece Hardness on Surface Residual Stresses in Finish Hard Turning of AISI 52100 Steel," *Trans. of the ASME, J. of Manufacturing Science*

- and Engineering*, vol. 122, no. 4, pp. 642-649, 2000.
- [12] J. Hua, D. Umbrello and R. Shivpuri, "Investigation of Cutting Conditions and Cutting Edge Preparations for Enhanced Compressive Subsurface Residual Stress in the Hard Turning of Bearing Steel," *J. of Material Processing Technology*, vol. 171, no. 1, pp. 180-187, 2006.
- [13] K. Ee, O. Dillon and I. Jawahir, "Finite Element Modeling of Residual Stresses in Machining Induced by Cutting using a Finite Edge Radius," *Int. J. of Mechanical Sciences*, vol. 47, no. 1, pp. 1611-1628, 2005.
- [14] C. Liu and M. Barash, "The Mechanical State of the Sublayer of a Surface Generated by Chip-Removal Process, Part 1: Cutting with a Sharp Edge," *Trans. of the ASME, J. of Engineering for Industry*, vol. 98, no. 4, pp. 1192-1202, 1976.
- [15] Q. Xie, A. Bayoumi and L. Kendall, "On Tool Wear and its Effect on Machined Surface Integrity," *J. Mater. Shaping Technol.*, vol. 8, no. 1, pp. 255-265, 1990.
- [16] T. El-Wardany, H. Kishawy and M. Elbestawi, "Surface Integrity of Die Materials in High Speed Hard Machining. Part 2: Micro-Hardness Variations and Residual Stresses," *Trans. of the ASME, J. of Manufacturing Science and Engineering*, vol. 122, no. 4, pp. 632-641, 2000.
- [17] S. Jeelani and J. Bailey, "Residual Stress Distribution in Machining Annealed 18 Percent Nickel Maraging Steel," *Trans. of the ASME, J. of Engineering Materials and Technology*, vol. 108, no. 2, pp. 93-98, 1986.
- [18] L. Chen, T. El-Wardany and W. Harris, "Modelling the Effects of Flank Wear and Land and Chip Formation on Residual Stresses," *Ann. CIRP*, vol. 53, no. 1, pp. 95-98, 2004.
- [19] C. Liu, Z. Lin and M. Barash, "Thermal and Mechanical Stresses in the Workpiece during Machining," *ASME, Production Engineering Division*, vol. 12, no. 1, pp. 181-191, 1984.
- [20] P. Vomacka and H. Walburger, "Residual Stresses due to Hard Machining – Industrial Experiences," *Material Science Forum*, vol. 347, no. 1, pp. 592-597, 2000.
- [21] P. Dahlman, F. Gunnberg and M. Jacobson, "The Influence of Rake Angle, Cutting Feed and Cutting Depth on Residual Stresses in Hard Turning," *J. of Material Processing Technology*, vol. 147, no. 1, pp. 181-184, 2004.
- [22] R. M'Saoubi, J. Outeiro, B. Changeux, J. Lebrun and A. Dias, "Residual Stress

- Analysis in Orthogonal Machining of Standard and Resulfurized AISI 316L Steels," *J. of Materials Processing Technology*, vol. 96, no. 1, pp. 225-233, 1999.
- [23] M. Jacobson, P. Dahlman and F. Gunnberg, "Cutting Speed Influence on Surface Integrity of Hard Turned Bainite Steel," *J. of Materials Processing Technology*, vol. 128, no. 1, pp. 318-323, 2002.
- [24] C. Shet and X. Deng, "Residual Stresses and Strains in Orthogonal Metal Cutting," *Int. J. of Machine Tools and Manufacture*, vol. 43, no. 1, pp. 573-587, 2003.
- [25] A. Sharman, J. Hughes and K. Ridgway, "An Analysis of the Residual Stresses Generated in Inconel 718 When Turning," *J. of Materials Processing Technology*, vol. 173, no. 1, pp. 359-367, 2006.
- [26] J. Outeiro, J. Pina, R. M'Saoubi, F. Pusavec and I. Jawahir, "Analysis of Residual Stresses Induced by Dry Turning of Difficult-to-Machine Materials," *Ann. CIRP*, vol. 57, no. 1, pp. 77-80, 2008.
- [27] I.S. Jawahir, E. Brinksmeier, R. M'Saoubi, D. Aspinwall, J. Outeiro, D. Meyer, D. Umbrello and A. Jayal, "Surface Integrity in Material Removal Processes: Recent Advances," *Ann. CIRP*, vol. 60, no. 2, pp. 603-626, 2011.
- [28] P. Withers, M. Turski, L. Edwards, P. Bouchard and D. Buttle, "Recent Advances in Residual Stress Measurement," *Int. J. of Pressure Vessels and Piping*, vol. 85, no. 3, pp. 118-127, 2008.
- [29] M. Hutchings, P. Withers, T. Holden and T. Lorentzen, Introduction to the Characterisation of Residual Stresses by Neutron Diffraction, London: CRC Press, Taylor & Francis, 2005.
- [30] T. Pirling, G. Bruno and P. Withers, "SALSA—A New Instrument for Strain Imaging in Engineering Materials and Components," *Mat Sci Eng*, vol. 437, no. 1, pp. 139-144, 2006.
- [31] M. Daymond and L. Edwards, "ENGIN-X: A Fully Refined Diffractometer," *Neutron News*, vol. 15, no. 1, pp. 24-29, 2004.
- [32] P. Withers, "Depth Capabilities of Neutron and Synchrotron Diffraction Strain Measurement Instruments: Part I—the Maximum Feasible Path Length," *J Appl Crystallogr*, vol. 37, no. 1, pp. 596-606, 2004.
- [33] H. Tönshoff, W. Schmieden, I. Inasaki, W. König and G. Spur, "Abrasive Machining of Silicon," *Ann. CIRP*, vol. 39, no. 2, pp. 621-635, 1990.

- [34] D. Lucca, E. Brinksmeier and G. Goch, "Progress in Assessing Surface and Subsurface Integrity," *Ann. CIRP*, vol. 47, no. 2, pp. 669-693, 1998.
- [35] T. Semba, K. Sakuma, Y. Tani and H. Sato, "Thickness Measurement of a Metallurgically Damaged Layer on a Ground Surface Using an Acoustic Microscope," *Ann. CIRP*, vol. 38, no. 1, pp. 549-552, 1989.
- [36] M. Duquennoy, M. Ouaftouh, M. Qian, F. Jenot and M. Ourak, "Ultrasonic Characterization of Residual Stresses in Steel Rods Using a Laser Line Source and Piezoelectric Transducers," *NDT Int.*, vol. 34, no. 5, pp. 355-362, 2001.
- [37] J. Herrmann, J. Kim, L. Jacobs, J. Qu, J. Littles and M. Savage, "Assessment of Material Damage in a Nickel-base Superalloy Using Nonlinear Rayleigh Surface Waves," *J. of Applied Physics*, vol. 99, no. 12, pp. 124913-124913, 2006.
- [38] N. Rossini, M. Dassisti, K. Benyounis and A. Olabi, "Methods of Measuring Residual Stresses in Components," *Materials & Design*, vol. 35, no. 1, pp. 572-588, 2012.
- [39] A. Olabi and M. Hashmi, "Stress Relief Procedures for Low Carbon Steel (1020) Welded Components," *J Mater Process Technology*, vol. 56, no. 1, pp. 552-562, 1996.
- [40] M. Fitzpatrick, A. Fry, P. Holdway, F. Kandil, J. Shackleton and L. Suominen, "*Determination of Residual Stresses by X-ray Diffraction*" National Physical Laboratory, Teddington, UK.
- [41] B. Cullity and S. Stock, *Elements of X-ray Diffraction*, 3 ed., Upper Saddle River, NJ: Prentice Hall, 2001.
- [42] I. Noyan and J. Cohen, *Residual Stress – Measurement by Diffraction and Interpretation*, New York: Springer-Verlag, 1987.
- [43] S. Liang and J. Su, "Residual Stress Modeling in Orthogonal Machining," *Ann. CIRP*, vol. 56, no. 1, pp. 65-68, 2007.
- [44] P. Arrazola, T. Özel, D. Umbrello, M. Davies and I. Jawahir, "Recent Advances in Modelling of Metal Machining Processes," *Ann CIRP*, vol. 62, pp. 695-718, 2013.
- [45] K. Komvopoulos and S. Erpenbeck, "Finite Element Modelling of Orthogonal Metal Cutting," *Trans. of the ASME, J. of Engineering for Industry*, vol. 113, no. 3, pp. 253-267, 1991.
- [46] M. Baker, J. Rosler and C. Siemers, "A Finite Element Model of High Speed Metal

- Cutting with Adiabatic Shearing," *Computers and Structures*, vol. 80, no. 1, pp. 495-513, 2002.
- [47] C. Liu and Y. Guo, "Finite Element Analysis of the Effect of Sequential Cuts and Tool–Chip Friction on Residual Stresses in a Machined Layer," *Int. J. of Mechanical Sciences*, vol. 42, no. 6, pp. 1069-1086, 2000.
- [48] E. Ceretti, P. Fallbohmer, W. Wu and T. Altan, "Application of 2D FEM to Chip Formation in Orthogonal Cutting," *J. of Materials Processing Technology*, vol. 59, no. 1, pp. 169-181, 1996.
- [49] E. Ceretti, M. Lucchi and T. Altan, "FEM Simulation Orthogonal Cutting: Serrated Chip Formation," *J. of Materials Processing Technology*, vol. 95, no. 1, pp. 17-26, 1999.
- [50] T. Özel and T. Altan, "Process Simulation using Finite Element Method Prediction of Cutting Forces, Tool Stresses and Temperatures in Highspeed Flat End Milling Process," *Int. J. of Machine Tools and Manufacture*, vol. 40, no. 5, pp. 713-738, 2000.
- [51] F. Klocke, H. Raedt and S. Hoppe, "2D-FEM Simulation of the Orthogonal High Speed Cutting Process," *Machining Science and Technology*, vol. 5, no. 3, pp. 323-340, 2001.
- [52] D. Umbrello, A. Jayal, S. Caruso, O. Dillon and I. Jawahir, "Modeling of White and Dark Layer Formation in Hard Machining of AISI 52100 Bearing Steel," *Machining Science and Technology*, vol. 14, no. 1, pp. 128-147, 2010.
- [53] X. Yang and C. Liu, "A new Stress-Based Model of Friction Behaviour in Machining and its Significant Impact on Residual Stresses Computed by Finite Element Method," *Int. J. of Mechanical Sciences*, vol. 44, no. 1, pp. 703-723, 2002.
- [54] F. Salvatore, F. Halila, T. Mabrouki and H. Hamdi, "Numerical and Experimental Study of Residual Stress Induced by Machining Process," *Int. J. of Surface Science and Engineering*, vol. 6, no. 1, pp. 136-147, 2012.
- [55] A. Ramesh and S. Melkote, "Modeling of White Layer Formation Under Thermally Dominant Conditions in Orthogonal Machining of Hardened AISI 52100 Steel," *Int. J. of Machine Tools and Manufacture*, vol. 48, no. 3-4, pp. 402-414, 2008.
- [56] S. Ranganath, C. Guo and P. Hegde, "A Finite Element Modeling Approach to Predicting White Layer Formation in Nickel Superalloys," *Ann. CIRP*, vol. 58, no. 1, pp. 77-80, 2009.

- [57] A. Simoneau, E. Ng and M. Elbestawi, "Grain Size and Orientation Effects When Microcutting AISI 1045 Steel," *Ann. CIRP*, vol. 56, no. 1, pp. 57-60, 2007.
- [58] A. Simoneau, E. Ng and M. Elbestawi, "Surface Defects During Microcutting," *Int. J. of Machine Tools & Manufacture*, vol. 46, no. 1, pp. 1378-1387, 2006.
- [59] M. Miguélez, A. Munoz-Sanchez, J. Cantero and J. Loya, "An Efficient Implementation of Boundary Conditions in an ALE Model for Orthogonal Cutting," *J. of Theoretical and Applied Mechanics*, vol. 47, no. 3, pp. 599-616, 2009.
- [60] M. Miguélez, R. Zaera, A. Molinari, R. Cheriguene and A. Rusinek, "Residual Stresses in Orthogonal Cutting of Metals: the Effect of Thermomechanical Coupling Parameters and of Friction," *J. of Thermal Stresses*, vol. 32, no. 1, pp. 269-289, 2009.
- [61] M. Nasr, E. Ng and M. Elbestawi, "Modelling the Effects of Tool-Edge Radius on Residual Stresses when Orthogonal Cutting AISI 316L," *Int. J. of Machine Tools and Manufacture*, vol. 47, no. 2, pp. 401-411, 2007.
- [62] M. Nasr, E. Ng and M. Elbestawi, "A Modified Time-Efficient FE Approach for Predicting Machining-Induced Residual Stresses," *Finite Elements in Analysis and Design*, vol. 44, no. 4, pp. 149-161, 2008.
- [63] E. Ng, T. El-Wardany, M. Dumitrscu and M. Elbestawi, "Physics-Based Simulation of High Speed Machining," *Machining Science and Technology*, vol. 6, no. 3, pp. 301-329, 2002.
- [64] A. Simoneau, E. Ng and M. Elbestawi, "Modeling the Effects of Microstructure in Metal Cutting," *Int. J. of Machine Tools and Manufacture*, vol. 47, no. 1, pp. 368-375, 2006.
- [65] C. Dandekar, Y. Shin and J. Barnes, "Machinability Improvement of Titanium Alloy (Ti-6Al-4V) via LAM and Hybrid Machining," *Int. J. of Machine Tools and Manufacture*, vol. 50, no. 2, pp. 174-182, 2010.
- [66] B. Rao, C. Dandekar and Y. Shin, "An Experimental and Numerical Study on the Face Milling of Ti-6Al-4V Alloy: Tool Performance and Surface Integrity," *J. of Materials Processing Technology*, vol. 211, no. 2, pp. 294-304, 2011.
- [67] J. Hua and R. Shivpuri, "A Cobalt Diffusion Based Model for Predicting Crater Wear of Carbide Tools in Machining Titanium Alloys," *J. of Engineering Materials and Technology*, vol. 127, no. 1, pp. 136-144, 2005.
- [68] J. Lorentzon and N. Järvstråt, "Modelling tool wear in cemented-carbide machining

- alloy 718," *Int. J. of Machine Tools and Manufacture*, vol. 48, no. 10, pp. 1072-1080, 2008.
- [69] E. Usui, T. Shirakashi and T. Kitagawa, "Analytical Prediction of Cutting Tool Wear," *Wear*, vol. 100, no. 1, pp. 129-151, 1984.
- [70] T. Özel, "The Influence of Friction Models on Finite Element Simulations of Machining," *Int. J. of Machine Tools and Manufacture*, vol. 46, no. 1, pp. 518-530, 2006.
- [71] I. Filice, F. Micari, S. Rizzuti and D. Umbrello, "A Critical Analysis on the Friction Modelling in Orthogonal Machining," *Int. J. of Machine Tools and Manufacture*, vol. 47, no. 3-4, pp. 709-714, 2007.
- [72] S. Anurag and Y. Guo, "Predictive Model to Decouple the Contributions of Friction and Plastic Deformation to Machined Surface Temperatures and Residual Stress Patterns in Finish Dry Cutting," *Frontiers of Mechanical Engineering in China*, vol. 5, no. 3, pp. 247-255, 2010.
- [73] M. Miguelez, R. Zaera, A. Rusinek, A. Moufki and A. Molinari, "Numerical Modelling of Orthogonal Cutting: Influence of Cutting Conditions and Separation criterion," *J. of Physics IV France*, vol. 134, no. 1, pp. 417-422, 2006.
- [74] M. Nasr, E. Ng and M. Elbestawi, "Modelling the Effects of Tool-Edge Radius on Residual Stresses when Orthogonal Cutting AISI 316L," *Int. J. of Machine Tools and Manufacture*, vol. 47, no. 1, pp. 401-411, 2007.
- [75] V. Schulze and F. Zanger, "Numerical Analysis of the Influence of Johnson-Cook-Material Parameters on the Surface Integrity of Ti-6Al-4V," *Procedia Engineering*, vol. 19, no. 1, pp. 306-311, 2011.
- [76] A. Kortabarri, A. Madariag, E. Fernandez, J. Esnaol and P. Arrazola, "A Comparative Study of Residual Stress Profiles on Inconel 718 Induced by Dry Face Turning," *Procedia Engineering*, vol. 19, no. 1, pp. 228-234, 2011.
- [77] I. Lazoglu, D. Ulutan, B. Alaca, S. Engin and B. Kaftanoglu, "An Enhanced Analytical Model for Residual Stress Prediction in Machining," *Ann. CIRP*, vol. 57, no. 1, pp. 81-84, 2008.
- [78] Y. Guo and C. Liu, "FEM Analysis of Mechanical State on Sequentially Machined Surfaces," *Machining Science and Technology*, vol. 6, no. 1, pp. 21-41, 2002.
- [79] J. Outeiro, D. Umbrello and R. M'Saoubi, "Experimental and Numerical Modelling of the Residual Stresses Induced in Orthogonal Cutting of AISI 316L Steel," *Int. J.*

- of Machine Tools and Manufacture*, vol. 46, no. 14, pp. 1786-1794, 2006.
- [80] D. Schwach and Y. Guo, "A Fundamental Study on the Impact of Surface Integrity by Hard Turning on Rolling Contact Fatigue," *Int. J. of Fatigue*, vol. 28, no. 1, pp. 1838-1844, 2006.
- [81] A. Ramesh, J. Thiele and S. Melkote, "Residual Stress and Sub-surface Flow in Finish Hard Turned AISI 4340 and 52100 Steels: A Comparative Study," *Proceedings of the ASME IMECE*, pp. 831-837, 1998.
- [82] Y. Chou and C. Evans, "White Layer and Thermal Modelling of Hard Turned Surfaces," *Int. J. of Machine Tools and Manufacture*, vol. 39, no. 1, pp. 1863-1881, 1999.
- [83] J. Barry and G. Byrne, "TEM Study on the Surface White Layer in Two Turned Hardened Steels," *Mater. Sci. Eng.*, vol. 325, no. 1-2, pp. 356-364, 2002.
- [84] Y. Guo and J. Sahni, "A Comparative Study of Hard Turned and Cylindrically Ground White Layers," *Int. J. of Machine Tools and Manufacture*, vol. 44, no. 2, pp. 135-145, 2004.
- [85] A. Warren, Y. Guo and M. Weaver, "The Influence of Machining Induced Residual Stress and Phase Transformation on the Measurement of Subsurface Mechanical Behaviour using Nano Indentation," *Surf. & Coating Technol.*, vol. 200, no. 11, pp. 3459-3467, 2006.
- [86] V. Schulze, J. Michna, J. Schneider and P. Gumbsch, "Modelling of Cutting Induced Surface Phase Transformations Considering Friction Effects," *Procedia Engineering*, vol. 19, no. 1, pp. 331-336, 2011.
- [87] S. Jaspers and J. Dautzenberg, "Material Behaviour in Metal Cutting: Strains, Strain rates and Temperatures in Chip Formation," *J. of Materials Processing Technology*, vol. 121, no. 1, pp. 123-135, 2002.
- [88] T. Belytchko, W. Liu and B. Moran, *Nonlinear Finite Elements for Continua and Structures*, Toronto: John Wiley and Sons Ltd., 2000.
- [89] J. Sun, K. Lee and H. Lee, "Comparison of Implicit and Explicit F.E. Methods for Dynamic Problems," *J. of Materials Processing Technology*, vol. 105, no. 1, pp. 110-118, 2000.
- [90] A. Shih, "Finite Element Analysis of the Rake Angle Effects in Orthogonal Metal Cutting," *Int. J. of Mechanical Sciences*, vol. 38, no. 1, pp. 1-17, 1996.

- [91] A. Mamalis, M. Horváth, A. Branis and D. Manolacos., "Finite Element Simulation of Chip Formation in Orthogonal Metal Cutting," *J. of Materials Processing Technology*, vol. 110, no. 1, pp. 9-27, 2001.
- [92] Y. Guo. and C. Liu., "3D FEA Modeling of Hard Turning," *J. of Manufacturing Science and Engineering*, vol. 124, no. 1, pp. 189-199, 2002.
- [93] G. Shi, X. Deng and C. Shet, "A Finite Element Study of the Effect of Friction in Orthogonal Metal Cutting," *Finite Elements in Analysis and Design*, vol. 38, no. 1, pp. 863-883, 2002.
- [94] C. Shet and X. Deng, "Finite Element Analysis of the Orthogonal Metal Cutting Process," *J. of Materials Processing Technology*, vol. 105, no. 1, pp. 95-109, 2000.
- [95] K. Li, X.L. Gao and J. Sutherland, "Finite Element Simulation of the Orthogonal Metal Cutting Process for Qualitative Understanding of the Effects of Crater Wear on the Chip Formation Process," *J. of Materials Processing Technology*, vol. 127, no. 1, pp. 309-324, 2002.
- [96] T. Childs and K. Maekawa, "Computer Aided Simulation and Experimental Studies of Chip Flow and Tool Wear in the Turning of Low Alloy Steels by Cemented Carbide Tools," *Wear*, vol. 139, no. 1, pp. 235-250, 1990.
- [97] K. Kim, W. Lee and H. Sin, "A Finite Element Analysis of Machining With the Tool Edge Considered," *J. of Materials Processing Technology*, vol. 86, no. 1, pp. 45-55, 1999.
- [98] M. Movahhedy, M. Gadala and Y. Altintas, "Simulation of Chip Formation in Orthogonal Metal Cutting Process: an ALE Finite Element Approach," *Machining Science and Technology*, vol. 4, no. 1, pp. 15-42, 2000.
- [99] M. Gadala, "Recent Trends in ALE Formulation and its Application in Solid Mechanics," *Computer Methods in Applied Mechanics and Engineering*, vol. 193, no. 1, pp. 4247-4275, 2004.
- [100] M. Shaw, *Metal Cutting Principles*, 2 ed., New York: Oxford University Press, 2005.
- [101] G. Johnson and W. Cook, "A Constitutive Model and Data for Metals Subject to Large Strains, High Strain Rates and High Temperatures," *7th Int. Symposium on Ballistics*, pp. 541-547, 1983.
- [102] F. Zerilli and R. Armstrong, "Dislocation Mechanics Based Constitutive Relations for Material Dynamics Calculations," *J. of Applied Physics*, vol. 61, no. 5, pp.

1816-1825, 1987.

- [103] N. Fang, "A New Quantitative Sensitivity Analysis of the Flow Stress of 18 Engineering Materials in Machining," *Trans. ASME, J. of Engineering Materials and Technology*, vol. 127, no. 2, pp. 192-196, 2005.
- [104] B. Gama, S. Lopatnikov and J. Gillespie, "Hopkinson Bar Experimental Technique: A Critical Review," *Appl Mech Rev*, vol. 57, no. 4, pp. 223-250, 2004.
- [105] Y. Yen, A. Jain, P. Chigurupati, W. Wu and T. Altan, "Computer Simulation of Orthogonal Cutting using a Tool with Multiple Coatings," *Machining Science and Technology*, vol. 8, no. 2, pp. 305-326, 2004.
- [106] Abaqus User's Manual, 6.8 ed., SIMULA, 2008.
- [107] N. Youssefian and P. Koshy, "Parametric Characterization of the Geometry of Honed Cutting Edges," *Precision Engineering*, vol. 37, no. 3, pp. 746-752, 2013.
- [108] R. Coelho, E. Ng and M. Elbestawi, "Tool Wear when Turning Hardened AISI 4340 with Coated PCBN Tools using Finishing Cutting Conditions," *Int. J. of Machine Tools and Manufacture*, vol. 47, no. 1, pp. 263-272, 2007.
- [109] S. Han, "Mechanisms and Modelling of White Layer Formation in Orthogonal Machining of Steel," 2006.
- [110] J. Strenkowski and K. Moon, "Finite Element Prediction of Chip Geometry and Tool/Workpiece Temperature Distributions in Orthogonal Metal Cutting," *ASME J. of Engineering for Industry*, vol. 112, no. 1, pp. 313-318, 1990.
- [111] P. Wright, J. Horne and D. Tabor, "Boundary Conditions at the Chip-Tool Interface in Machining: Comparisons Between Seizure and Sliding Friction," *Wear*, vol. 54, no. 2, pp. 371-390, 1979.
- [112] S. Raman, A. Longstreet and D. Guha, "A Fractal View of Tool-Chip Interfacial Friction in Machining," *Wear*, vol. 253, no. 11-12, pp. 1111-1120, 2002.
- [113] J. Boyd, Tribometer-Based Quantification of Friction in Metal Cutting, M.A.Sc. Dissertation, Hamilton: McMaster University, 2012.
- [114] P. Hendrik, F. Klocke and D. Lung, "A New Experimental Methodology to Analyse the Friction Behaviour at the Tool-Chip Interface in Metal Cutting," *Production Engineering*, vol. 6, no. 4-5, pp. 349-354, 2012.
- [115] T. Childs, "Material Property Needs in Modeling Metal Machining," *Proceedings*

- of the CIRP Int. Workshop on Modeling of Machining Operations*, vol. 1, no. 1, pp. 193-202, 1998.
- [116] L. Li and H. Kishawy, "A model for Cutting Forces Generated During Machining with Self-Propelled Rotary Tools," *Int. J. of Machine Tools and Manufacture*, vol. 46, no. 12-13, pp. 1388-1394, 2006.
- [117] E. Usui and T. Shirakashi, "Mechanics of Machining-from Descriptive to Predictive Theory," *On the Art of Cutting Metals-75 Years Later*, vol. 7, no. 1, pp. 13-55, 1982.
- [118] M. Dirikolu, T. Childs and K. Maekawa, "Finite Element Simulation of Chip Flow in Metal Machining," *Int. J. of Mechanical Sciences*, vol. 43, no. 1, pp. 2699-2713, 2001.
- [119] A. Shih, "Finite Element Analysis of the Rake Angle Effects in Orthogonal Metal Cutting," *Int. J. of Mechanical Science*, vol. 38, no. 1, pp. 1-17, 1996.
- [120] H. Kishawy, I. Deiab and A. Haglund, "Arbitrary Lagrangian Eulerian Analysis on Cutting with Honed Tools," *Proc. IMechE, J. Engineering Manufacture*, vol. 222, no. B, pp. 155-162, 2008.
- [121] T. Miokovic, J. Schwarzer, V. Schulze, O. Vöhringer and D. Löhe, "Description of Short Time Phase Transformations During the Heating of Steels Based on High-Rate Experimental Data," *J. Phys. IV France*, vol. 120, no. 1, pp. 591-598, 2004.
- [122] T. Mioković, V. Schulze, O. Vöhringer and D. Löhe, "Predictions of Phase Transformations During Laser Surface Hardening of AISI 4140 Including the Effects of Inhomogeneous Austenite Formation," *J. of Material Science and Engineering*, vol. 435, no. 1, pp. 547-555, 2006.
- [123] R. Lakhkar, Y. Shin and M. Krane, "Predictive Modeling of Multi-Track Laser Hardening of AISI 4140 steel," *J. of Materials Science and Engineering*, vol. 480, no. 1, pp. 209-217, 2008.
- [124] N. Bailey, W. Tan and Y. C. Shin, "Predictive Modeling and Experimental Results for Residual Stresses in Laser Hardening of AISI 4140 Steel by a High Power Diode Laser," *Surface and Coatings Technology*, vol. 203, no. 1, pp. 2003-2012, 2009.
- [125] C. Simsir and C. Gür, "A FEM Based Framework for Simulation of Thermal Treatments: Application to Steel Quenching," *Computational Materials Science*, vol. 44, no. 2, pp. 588-600, 2008.

- [126] M. Nasr, On Modelling of Machining-Induced Residual Stresses, Ph.D. Dissertation, Hamilton: McMaster University, 2007.

Appendix 1: Annealed Residual Stress Depth Profile

The measured residual stress depth profile for the AISI 1045 samples is give below:

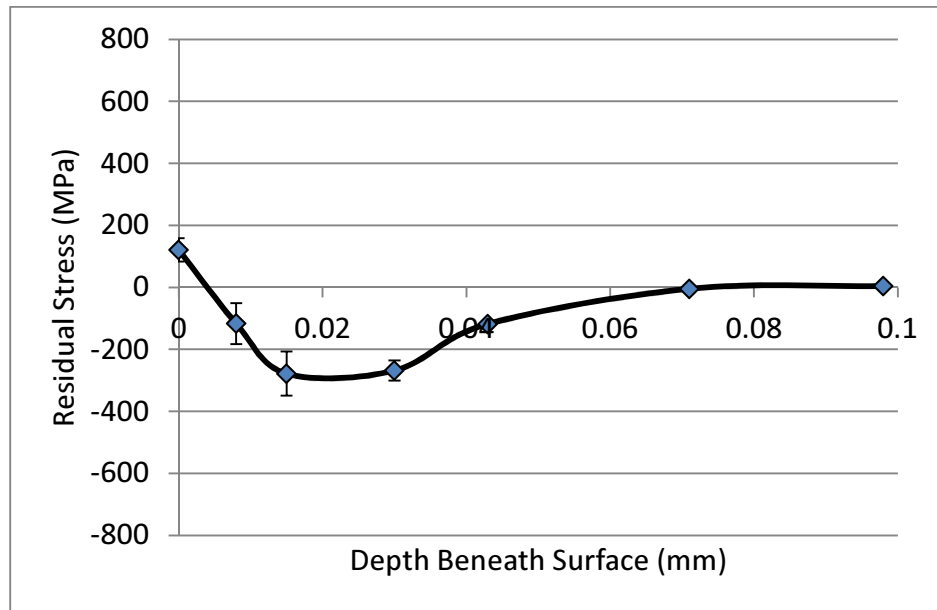


Figure A-1: Annealed AISI 1045 Sample Residual Stress Depth Profile